UNIVERSITAT DE BARCELONA

New therapeutic approaches to target myofibroblast activation in liver pathologies: fibrosis and cholangiocarcinoma

Josep Amengual Segura

New therapeutic approaches to target myofibroblast activation in liver pathologies: fibrosis and cholangiocarcinoma

This thesis is submitted to the University of Barcelona and presented by Josep Amengual Segura to obtain the degree of Doctor by the University of Barcelona

This work has been developed at Bellvitge Biomedical Research Institute (IDIBELL), under the supervision of Dr. Isabel Fabregat Romero and Dr. Javier Vaquero Rodríguez.

Dr. Isabel Fabregat Romero

Josep Amengual Segura

Dr. Javier Vaquero Rodríguez

TGF-β and Cancer group

Oncobell Program, IDIBELL

Doctoral Program in Biomedicine

University of Barcelona

This work has been developed at the Rosalind Franklin Area at Bellvitge Biomedical Research Institute (IDIBELL), L'Hospitalet de Llobregat, Barcelona.

The author enjoyed the following financial support for salary:

- Contract linked to the project *Desarrollo preclínico de un nuevo activo modulador de la fibrosis y la senescencia para el tratamiento de la enfermedad de hígado graso no-alcohólico*; RTC2019-007125-1. Funded by Ministerio de Ciencia e Innovación. Coordinated between Senolytic Therapeutics, Isabel Fabregat, María Luz Martinez Chantar and Manuel Serrano. From 01/03/2021 – 31/12/2022.
- Contract linked to the project *Descifrando el papel de la NADPH oxidasa NOX4 en el carcinoma hepatocelular: relevancia en células tumorales y estroma y relación con la vía del TGF-beta*; PID2021-122551-OB-I00. Funded by Ministerio de Ciencia e Innovación to Isabel Fabregat Romero. From 01/01/2023 – expected until 18/05/2025.

This research has been possible thanks to the financial support of the following institutions:

- Agencia Estatal de Investigación, Ministerio de Ciencia, Innovación y Universidades (MICIN), Spain, cofounded by FEDER funds/European Regional Development Fund– a way to build Europe:
    - *Project: Nuevas aproximaciones experimentales para analizar el papel de la NADPH oxidasa NOX4 en regeneración y cáncer hepáticos. Relación con la vía del TGF-beta*; RTI2018-094079-B-100.
    - *Project: Desarrollo preclínico de un nuevo activo modulador de la fibrosis y la senescencia para el tratamiento de la enfermedad de hígado graso no-alcohólico*; RTC2019-007125-1.
    - *Project*: *Dissecting the therapeutic potential of the NADPH oxidase NOX4 in cholangiocarcinoma through single-cell RNA sequencing*; PID2019-108651RJ-I00.
    - Project: *Descifrando el papel de la NADPH oxidasa NOX4 en el carcinoma hepatocelular: relevancia en células tumorales y estroma y relación con la vía del TGF-beta*; PID2021-122551OB-I00.
- Fundación Ramón Areces, Spain. Project: *Diseccionando el papel de la vía del receptor del factor de crecimiento epidérmico (EGFR) de hepatocitos en el interactoma celular dentro del nicho fibrótico hepático*; CIVP20A6593.
- Fundación Asociación Española Contra el Cáncer (AECC), Spain. Project: Towards a precision medicine using TGF-β inhibitors in hepatocellular carcinoma and cholangiocarcinoma; PRYGN211279FABR.
- Agència de Gestió d'Ajuts Universitaris i de Recerca (AGAUR), Generalitat de Catalunya, Spain. Project: Role of TGF-beta and the oxidative stress in human pathologies. Reference: 2021SGR00029.
- The CIBERehd, National Biomedical Research Institute on Liver and Gastrointestinal Diseases, funded by the Instituto de Salud Carlos III, Spain.

We are very grateful to Nuria Segovia and family for kindly funding research in cholangiocarcinoma.

We thank the Generalitat de Catalunya's support through the CERCA Programme.

ABBREVIATIONS

3D	Three-dimensional
α-SMA	α-smooth muscle actin
ADAM17	A disintegrin and metalloproteinase 17
ADP	Adenine diphosphate
ALD	Alcoholic liver disease
ANOVA	Analysis of variance
apCAF	Antigen-presenting cancer associated fibroblast
ASH	Alcoholic steatohepatitis
CAF	Cancer-associated fibroblast
Cas9	CRISPR-associated protein 9
CCA	Cholangiocarcinoma
cCasp3	Cleaved caspase 3
CCl_3	Trichloromethyl
CCl_4	Carbon tetrachloride
CD4	Cluster of differentiation 4
cDNA	Complementary DNA
CK19	Cytokeratin 19
COL1A1	α-1 type I collagen
CRISPR	Clustered regularly interspaced short palindromic repeats
CTLA4	Cytotoxic T-lymphocyte antigen 4
DAB	Diaminobenzidine
DAPI	4′,6-diamidino-2-phenylindole
DCA	Deoxycholic acid
dCCA	Distal cholangiocarcinoma
DMEM	Dulbecco’s modified eagle medium
DMSO	Dimethyl sulfoxide
DMT-1	Divalent metal transporter 1
DPI	Diphenyleneiodonium
DUOX	Dual oxidase
eCAF	Epithelial-to-mesenchymal cancer-associated fibroblast
eCCA	Extrahepatic cholangiocarcinoma

ECM	Extracellular matrix
EMT	Epithelial-to-mesenchymal transition
ERK	Extracellular signal-regulated kinase
FAD	Flavine adenine dinucleotide
FAP	Fibroblast activation protein
FBS	Foetal bovine serum
FDR	False discovery rate
GEO	Gene expression omnibus
gRNA	Guide RNA
GSVA	Gene set variation analysis
HAS2	Hyaluronan synthase 2
HBV	Hepatitis B virus
HCC	Hepatocellular carcinoma
HCV	Hepatitis C virus
HEPES	N-2-hydroxyethylpiperazine-N-2-ethane sulfonic acid
HFE	Homeostatic iron regulator
HGF	Hepatocyte growth factor
HSC	Hepatic stellate cell
iCAF	Inflammatory cancer-associated fibroblast
iCCA	Intrahepatic cholangiocarcinoma
IHC	Immunohistochemistry
MASLD	Metabolic dysfunction-associated steatotic liver disease
MEK	Mitogen-activated protein kinase kinase
MEM	Minimum essential medium
MMP	Matrix metalloproteinase
myCAF	Myofibroblastic cancer-associated fibroblast
NASH	Non-alcoholic steatohepatitis
NK	Natural killer cell
NOX	NADPH oxidase
NOXA1	NADPH oxidase activator 1
NOXO1	NADPH oxidase organizer 1

PCA	Principal component analysis
pCCA	Perihilar cholangiocarcinoma
PD-1	Programmed cell death protein 1
PD-L1	Programmed cell death ligand 1
RNA-seq	RNA sequencing
ROS	Reactive oxygen species
RSL3	Ras-selective lethal 3
RT-qPCR	Real-time quantitative PCR
SASP	Senescence-associated secretory phenotype
scRNA-seq	Single-cell RNA sequencing
SD	Standard deviation
SEM	Standard error of the mean
siRNA	Small interfering RNA
TACE	Tumour necrosis factor α converting enzyme
TAM	Tumour-associated macrophage
TAN	Tumour-associated neutrophil
TCGA	The cancer genome atlas
TE buffer	Tris-ethylenediaminetetraacetic buffer
TF	Transferrin
TFR	Transferrin receptor
TGF-β	Transforming growth factor β
TME	Tumour microenvironment
TNF-α	Tumour necrosis factor α
vCAF	Vascular cancer-associated fibroblast
VISTA	V-domain Ig suppressor of T cell activation
WT	Wild type

TABLE OF CONTENTS

I. INTRODUCTION

1. Liver pathologies where fibroblast activation plays a crucial role

1.1. Liver fibrosis

Liver fibrosis can be defined as a scar formation process characterized by excessive accumulation of extracellular matrix (ECM), particularly collagen, arising in response to chronic liver injury from various aetiologies such as viral hepatitis, alcohol abuse or steatosis. Physiologically, this process is meant to allow tissue repair upon acute damage that leads to a posterior scar resolution. However, when the etiological agent persists, liver fibrosis may progress towards cirrhosis, stage at which the liver architecture is completely disorganized, increasing the risk of potential deadly complications such as portal hypertension, development of hepatocellular carcinoma (HCC) and liver failure (**Figure 1**) [1, 2]. Despite the increase in the prevalence of advanced liver fibrosis and cirrhosis in the last years [3], effective anti-fibrotic therapies are lacking. In fact, it was not until this year that the Food and Drug Administration of the United States approved Rezdiffra (resmetirom) as the first treatment for patients with non-alcoholic steatohepatitis (NASH) with moderate to advanced fibrosis [4]. This is why, so far, medical interventions for liver fibrosis focus mainly on removing the causative agent of the disease. For instance, liver fibrosis or even cirrhosis caused by chronic HBV or HCV infection can regress following viral suppression [5, 6]. Similarly, reduction of body weight either through lifestyle modification [7] or bariatric surgery [8] also improves NASH features and fibrosis.

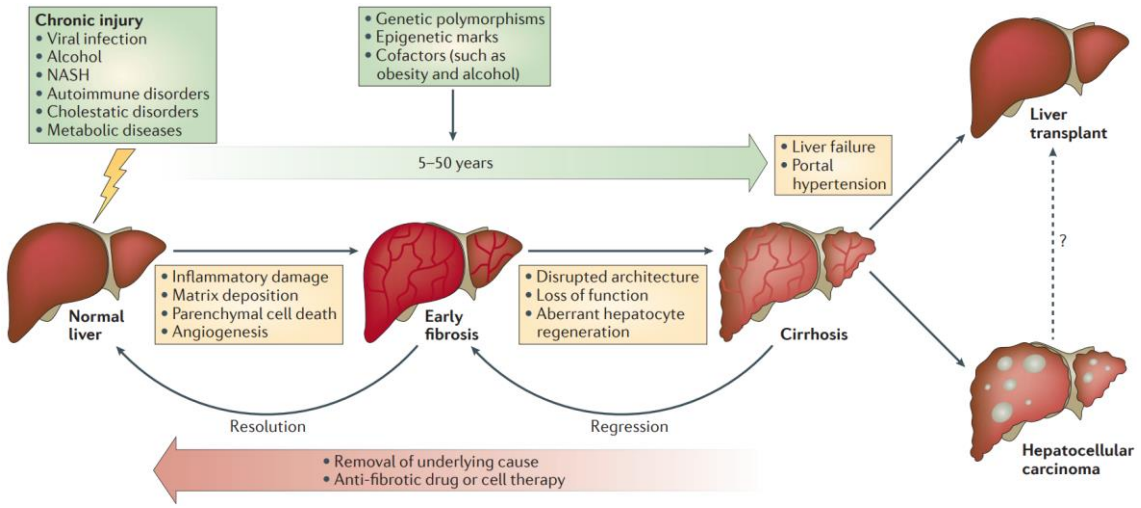

Figure 1. Natural history of chronic liver disease. Chronic injury caused by viral infection, alcohol or non-alcoholic steatohepatitis (NASH), among other aetiologies, trigger inflammatory damage, extracellular matrix deposition, parenchymal cell death and angiogenesis leading to progressive fibrosis. The scar matrix typically accumulates very slowly and if the cause of fibrosis is eliminated, resolution (that is, complete reversal to near-normal liver architecture) of early hepatic fibrosis can occur. In cirrhosis, although resolution is not possible, regression (that is, improvement but not reversal) of fibrosis improves clinical outcomes. Currently, liver transplantation is the only available treatment for liver failure or for some cases of primary liver cancer. Extracted from Pellicoro A. et *al* [2].

The key cellular player in liver fibrosis is the hepatic stellate cell (HSC). Under physiological conditions, HSC are found in a quiescent state in the space of Disse (between hepatocytes and sinusoidal endothelial cells) and its primary function is the storage of vitamin A in the form of lipid droplets [9]. In response to injury, damaged hepatocytes and biliary cells release inflammatory cytokines that activate Kupffer cells (resident macrophages) and stimulate the recruitment of activated T cells, amplifying the inflammatory microenvironment [1]. In response to these signals, HSC become activated and transdifferentiate into myofibroblast-like cells, being the main contributors to ECM deposition independently of the aetiology [10]. The activation process requires differentiation from the HSC adipogenic phenotype to a myofibroblastic one, characterized by the loss of vitamin A droplets, expression of contractile fibres such as α-smooth muscle actin (α-SMA), increase in proliferation and chemotaxis [9]. This profibrogenic activation is driven by various cytokines and growth factors. Amongst them, the transforming growth factor-beta (TGF-β) is the most significant one, considered the master regulator of fibrosis in multiple organs, including the liver [11]. TGF-β is produced by injured hepatocytes, Kupffer cells and even activated HSC as an autocrine signalling loop important for HSC activation [1]. In HSC, TGF-β promotes transdifferentiation into myofibroblasts, inhibits apoptosis and induces the synthesis of ECM proteins including collagens and fibronectin. In addition to the production of ECM, TGF-β also inhibits its degradation by decreasing matrix-degrading proteases and upregulating protease inhibitors [12].

Upon removal of the etiological agent, approximately 50% of the activated HSC undergo apoptosis, dictated by the balance between pro-apoptotic and pro-survival signals. Those activated HSC that escape apoptosis downregulate the profibrogenic gene expression, becoming senescent or reversing towards a phenotype similar to the quiescent HSC, in a process described as inactivation [13, 14]. In this regard, it has been observed that in mice, in the recovering liver after fibrosis resolution, HSC

population is renewed with the appearance over time of HSC that present identical characteristics to quiescent HSC from fibrosis-naïve mice [13].

1.2. Cholangiocarcinoma

Cholangiocarcinoma (CCA) is a highly aggressive malignancy originating from the biliary tract. It is the second most common primary liver cancer after HCC and is subclassified into intrahepatic (iCCA) or extrahepatic (eCCA) based on the anatomical origin along the biliary tree. eCCAs can be further sub-classified into perihilar (pCCA) and distal (dCCA), based on the location relative to the cystic duct (**Figure 2**) [15]. In this thesis we will focus on iCCA subtype.

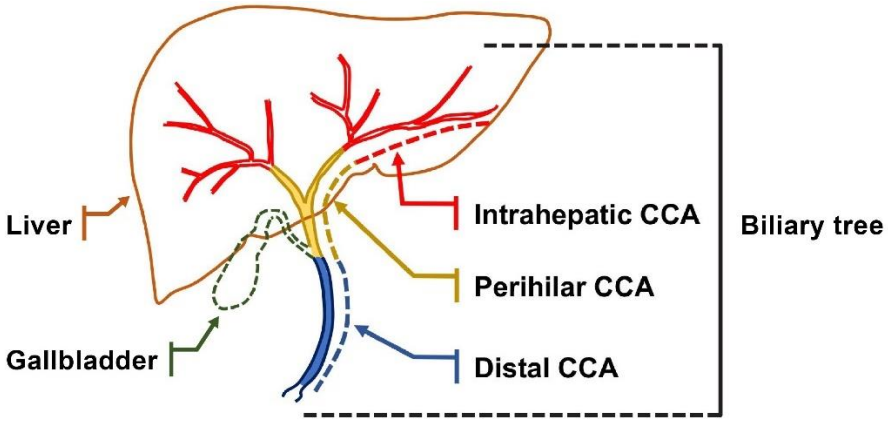

Figure 2. Anatomical classification of cholangiocarcinoma. According to their anatomical location, CCAs are classified into intrahepatic, perihilar and distal. Adapted from Kendall T. *et al.* [16].

Despite being relatively rare, accounting for 3% of gastrointestinal cancers [17], CCA presents an increasing incidence and mortality in the Western countries. Several risk factors are known which include liver flukes (particularly in Asian countries), primary sclerosing cholangitis, viral hepatitis, alcohol consumption and metabolic dysfunction-associated steatotic liver disease (MASLD). However, most cases are sporadic with no identified cause [18].

The clinical management of CCA is particularly challenging due to its asymptomatic early stages that lead to a late diagnosis, as well as resistance to therapies. Surgical resection remains the only curative option, but only a minority of patients are eligible for it. For unresectable or advanced stages, chemotherapy

regimens with gemcitabine and cisplatin have been the standard of care for many years, although providing only modest improvements in survival. Combination with immunotherapy (durvalumab or pembrolizumab) was recently approved as the new standard of care, improving survival for the first time in years, although many patients remain unresponsive [19-21].

A growing number of studies has highlighted the role of the tumour microenvironment (TME) in the progression of CCA. CCA is characterized by a prominent desmoplastic stroma, composed mainly of cancer-associated fibroblasts (CAF). CAFs originate mainly from HSC and portal fibroblasts and express markers such as α-SMA, α-1 type I collagen (COL1A1), vimentin or fibroblast activation protein (FAP). In addition, these stromal cells produce a dense ECM composed of collagens, fibronectins and other proteins that form a physical barrier that impairs delivery of therapies to the tumour site, thus contributing to increased tumour growth and resistance to therapies. In fact, a prominent stroma has been clinically related to poor prognosis [22-24], and targeting CAFs pharmacologically or genetically has shown positive results in terms of reduced tumour progression and increased overall survival in preclinical models [25]. Moreover, CAFs and the secreted ECM interact with the immune cell populations in a complex and intricate crosstalk [26]. CCA is considered a “cold” tumour regarding immune infiltration, particularly in the case of cytotoxic T cells and natural killers, while there are abundant immunosuppressive players, such as myeloid-derived suppressor cells. Moreover, the expression of immune-checkpoint molecules such as programmed cell death protein 1 (PD-1) and its ligand programmed cell death ligand 1 (PD-L1) as well as cytotoxic T-lymphocyte associated protein 4 (CTLA4) is increased on the tumour-infiltrating immune cells, indicating an immunosuppressive milieu (**Figure 3**) [27].

The recent use of scRNA-seq technology has allowed for the classification of different CAF subpopulations based on their transcriptome. Some of the most accepted ones are the myofibroblastic CAFs (myCAF), enriched in ECM transcripts, the inflammatory CAFs (iCAFs) enriched in inflammatory response and growth factor transcripts, the antigen-presenting CAFs (apCAF) enriched in major histocompatibility complex II transcripts, the vascular CAFs (vCAF) enriched in vascular development transcripts or the epithelial-to-mesenchymal CAFs (eCAF) expressing epithelial-to-mesenchymal markers [28]. The most abundant types found in CCA TME are iCAFs or vCAFs, followed by myCAFs. Interestingly, it has been

shown that each subpopulation interacts with the tumour cells in a distinct manner. For instance, myCAF promote tumour growth via hyaluronan synthase 2 (HAS2) expression, while iCAF promote tumour proliferation through the expression of hepatocyte growth factor (HGF) [29].

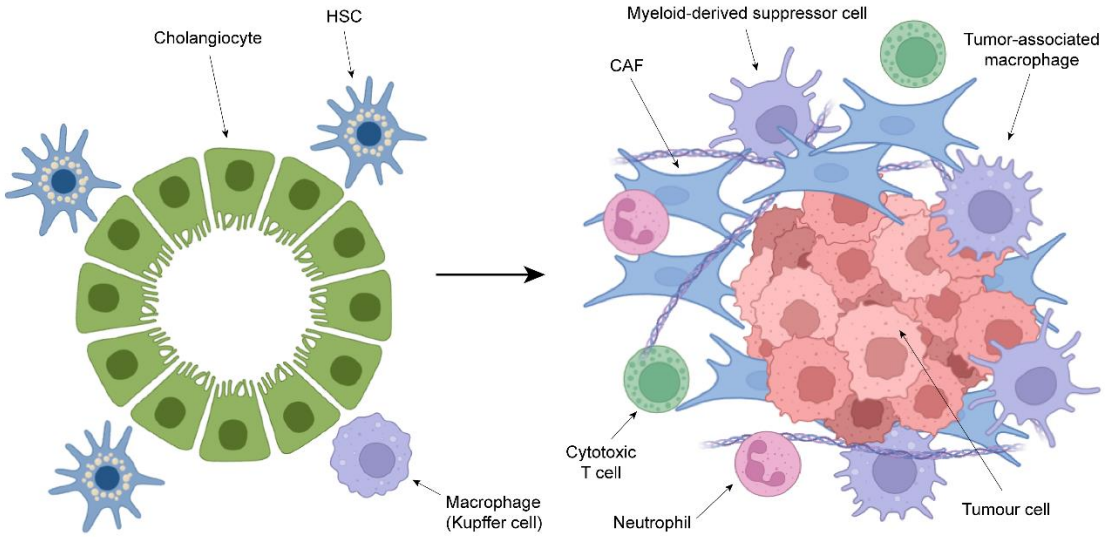

Figure 3. Changes in the stroma during cholangiocarcinogenesis. Under physiological conditions, normal bile ducts are surrounded by a thin layer of extracellular matrix (ECM) and quiescent hepatic stellate cells (HSC). In response to liver injury or paracrine signals released by transformed cholangiocytes, HSC transdifferentiate into an activated state and become cancer-associated fibroblasts (CAF). CAF are characterized by the expression of α-smooth muscle actin and secretion of ECM in huge amounts, leading to a prominent and stiff stroma that supports tumour growth, confers chemoresistance and suppresses the immune response against tumour cells. For instance, the fibrotic stroma excludes cytotoxic T cells and favours the presence of myeloid-derived suppressor cells, tumour-associated macrophages and neutrophils related with defective immune responses. Created with Biorender.com.

TGF-β activates a complex signalling pathway that regulates different cellular processes, including proliferation, migration or cell death [30]. In HCC TGF-β acts as a tumour suppressor in the early stages of tumour development, while in advanced stages it exerts tumour-promoting actions. However, the role of TGF-β in CCA is not well understood [31]. In the CCA tumour cell it is still a controversial topic, with reports conferring this cytokine a pro epithelial-to-mesenchymal transition (EMT) role [32], while others show that it can exert tumour suppressor effects in CCA cell lines [33]. Preliminary results from our group indicated that TGF-β acts as a tumour suppressor in CCA cells, strongly reducing cell viability, whereas inhibiting TGF-β effects through a TGR-β Receptor II inhibitor (galunisertib) had the opposite effect, promoting tumour

cell proliferation and growth in three dimensional (3D)-spheroids (unpublished, manuscript under review).

In contrast, in the TME the literature indicates that TGF-β is predominantly associated with pro-tumorigenic effects. Concretely, TGF-β helps to generate an advantageous TME by activating CAF, inducing angiogenesis and promoting immune suppression and evasion (**Figure 4**) [30]. Indeed, CCA stroma undergoes profound changes during tumorigenesis with an upregulation of genes related to TGF-β pathway and inflammation [31]. Nevertheless, the last phase II/III clinical trial (NCT04066491) using a TGF-β inhibitor in combination with chemotherapy did not reach the expected success and has been discontinued [34].

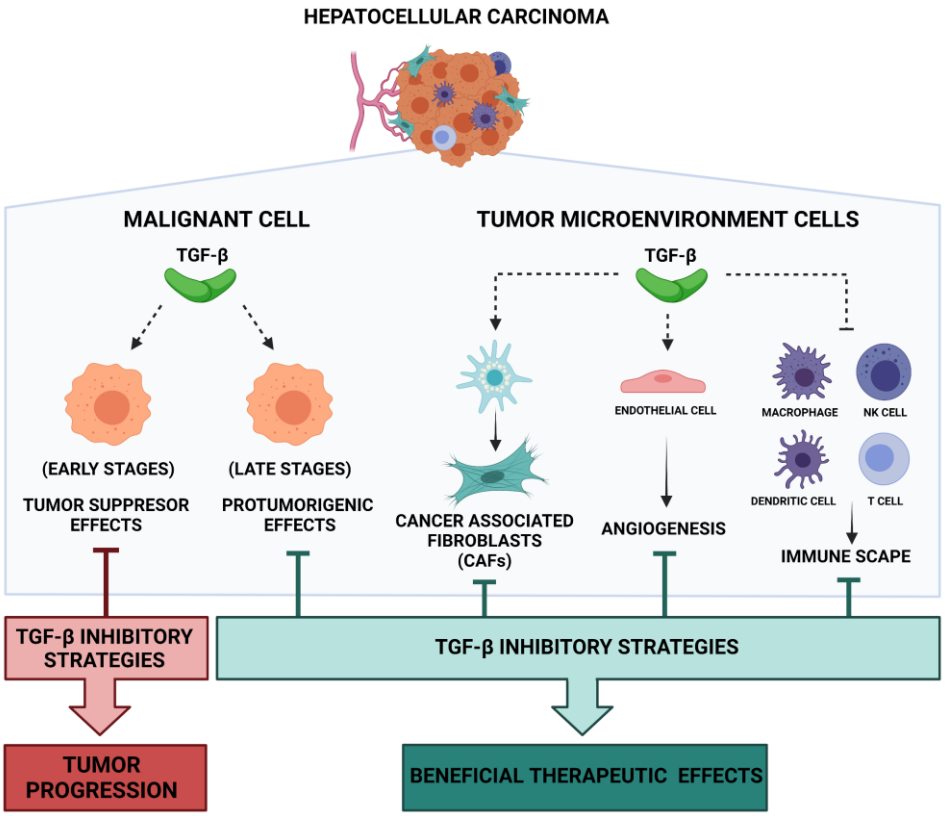

Figure 4. Role of TGF-β pathway in hepatocellular carcinoma (HCC). TGF-β plays a dual role in HCC, acting as a tumour suppressor at early stages but favouring tumour progression at late stages. In the tumour microenvironment, TGF-β contributes to hepatic stellate cell activation to cancer-associated fibroblasts (CAF), promotes angiogenesis by endothelial cells and exerts immunosuppressive effects in the immune cell populations. Extracted from Gonzalez-Sanchez E. *et al.* [35].

2. Role of senescence and iron homeostasis in fibrotic pathologies

2.1. Senescence

Cellular senescence is a physiological process in which cells stop proliferating and enter a state of permanent cell cycle arrest. Senescence can be triggered by several types of stress such as replicative exhaustion, oncogene activation or chemotherapeutic agents. It is considered to originally have a protective role from tumour-driver mutations and help in tissue remodelling during development [36]. Senescent cells express cyclin-dependent kinases inhibitors such as p16 or p21, responsible for the proliferative arrest, present enlarged cell morphology, enhanced β-galactosidase activity and produce a wide variety of factors known as the senescence-associated secretory phenotype (SASP) that influence neighbouring cells [37]. The SASP can play both beneficial and detrimental effects. On one side, it contributes to the recruitment of immune cells to clear senescent/damaged cells [36], and it may have tumour suppressor activities by reinforcing the cell cycle arrest in an autocrine manner [38] and the polarization of macrophages towards tumour-inhibiting M1 state [39]. On the other side, the SASP mediates a continuous systemic inflammation that aggravates many age-related conditions and diseases, including idiopathic pulmonary fibrosis, obesity, osteoarthritis and type 2 diabetes [40].

Accumulating data have indicated that cellular senescence plays a relevant role in the occurrence and development of liver disease [41]. Senescent hepatocytes accumulate in chronic liver disease independently of the aetiology and their proportion correlates with the degree of fibrosis [42-45]. Indeed, it has been demonstrated that senescence induces the secretion of pro-inflammatory cytokines by hepatocytes, as part of the SASP, which activate HSCs [46, 47], impair liver regeneration [48, 49] and promote the recruitment of pro-inflammatory macrophages, contributing to the progression of liver disease [50]. Therefore, elimination of senescent hepatocytes or inhibition of hepatocyte senescence have been proposed as potential therapeutic strategies for MASLD or liver fibrosis [51]. In contrast, senescence in HSC has been linked to fibrosis resolution [52]. The number of senescent activated HSC increases in livers recovering from liver fibrosis. Senescence of myofibroblasts decreases the secretion of ECM, increases the expression of ECM-degrading enzymes, enhances immune surveillance and, consequently, reduces liver fibrosis in mice [53]. For example, upregulation of IL-22

promotes HSC senescence and inhibits the expression of α-SMA, and mice overexpressing IL-22 have reduced levels of fibrosis [54].

2.2. Iron homeostasis

In vertebrates, iron is absorbed in the intestine and circulates through the bloodstream bound to a protein named transferrin (TF) to be delivered to all cells. In the plasma membrane, cells express transferrin receptors (TFR1 and TFR2) and the homeostatic iron regulator (HFE) that bind to the circulating iron-bound transferrin and internalize the complex by clathrin-mediated endocytosis (**Figure 5**, [55]).

Iron homeostasis in the body is regulated at the absorption level. This may be attributed to the fact that during our species evolution, the challenge in human nutrition has been primarily iron deficiency, not excess of it, so there is no physiological pathway for iron removal from the body, which only happens with blood loss and epithelial cell desquamation in the gastrointestinal and urinary tracts, skin and hair [56]. The central regulator of iron metabolism is the hormone hepcidin produced by hepatocytes. Hepcidin decreases the expression of divalent metal transporter (DMT)-1 protein on the apical surface of enterocytes that mediates iron uptake, and thus reduces intestinal iron absorption (**Figure 5**). Hepcidin gene mutations that disrupt its function lead to excessive iron absorption and accumulation in the liver and other organs [57].

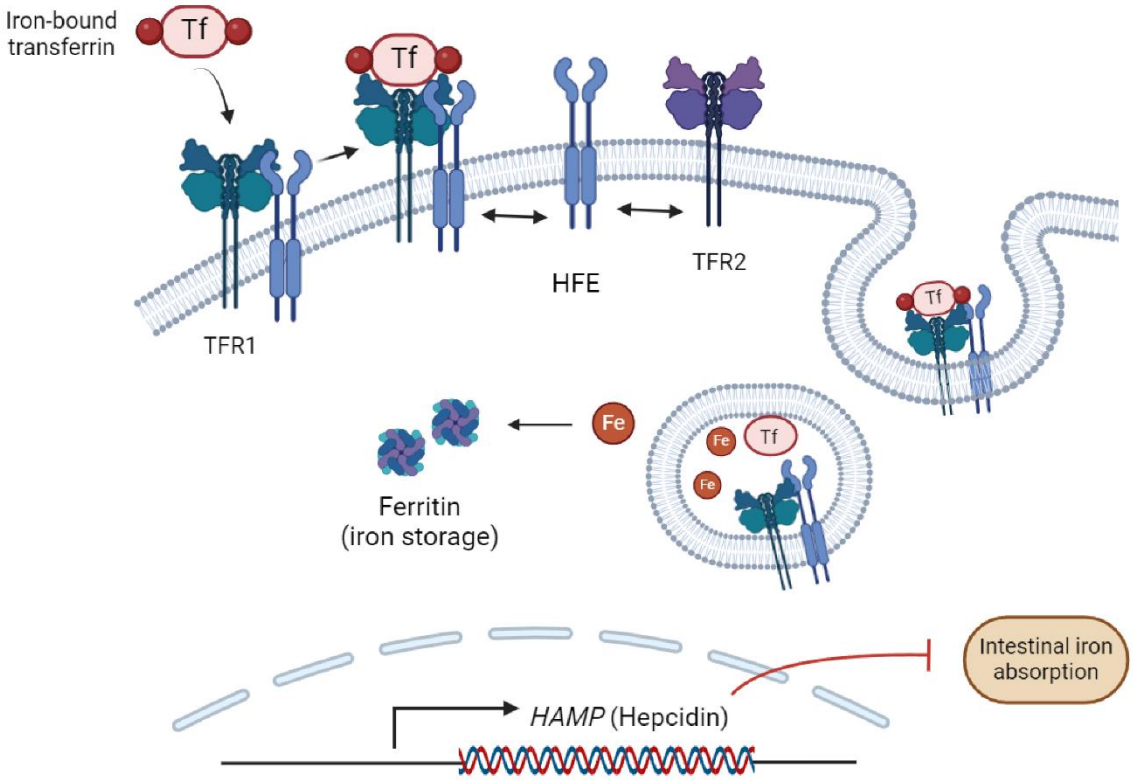

Figure 5. Schematic representation of iron homeostasis in hepatocytes. Iron is carried by transferrin (TF) through circulation. Hepatocytes express transferrin receptors 1 and 2 (TFR1, TFR2) in the plasma membrane. The homeostatic iron regulator protein (HFE) interacts with the transferrin receptors and helps the binding of iron-bound transferrin. Then, the complex is internalized by clathrin-mediated endocytosis. Inside the cell, the endosomes fuse with lysosomes, acidifying the pH, which triggers the release of iron atoms from transferrin. Iron is stored bound to ferritin and the TFRs are recycled to the plasma membrane. When iron levels are high, different mechanisms lead to the upregulation of *HAMP* (hepcidin), to decrease iron absorption at the intestinal level. Created with Biorender.com.

The capacity of iron to switch between the Fe^{2+} and Fe^{3+} states explains its role as mediator of biochemical reactions in organisms. But this feature is a two-edged sword because it can easily turn into a source of oxidative damage. For this reason, iron atoms in the body are normally bound to the active sites of enzymes, securely stored in ferritin or being carried by transferrin [58]. A small fraction of iron can be found interacting with small molecules such as citrate [59], glutathione [60], ADP, acetate, pyruvate or other macromolecules [61]. This is referred as labile iron pool and can react with peroxides catalysing the formation of other ROS such as the hydroxyl radical, which in turn oxidize any chemical group nearby [58].

2.3. Crosstalk between iron metabolism and senescence

At the beginning of this thesis project, preliminary data from the group led by Dr. Manuel Serrano (IRB, Barcelona, Spain) suggested that in conditions of tissue damage, cells accumulated iron concomitant with the development of senescence, which was related to fibrotic responses. Recently, they published that in lung and kidney, senescent cells accumulate iron, which triggers ROS production and SASP. Moreover, these pathological hallmarks were counteracted by the treatment with an iron chelator, deferiprone, attenuating fibrosis in these organs. Thus, Maus M *et al*. established a connection between cellular damage, iron accumulation, senescence and fibrosis in kidney and lung, proposing iron metabolism as a therapeutic target for senescence-associated diseases [62].

In the liver, hereditary hemochromatosis, caused by mutations in hepcidin gene, leads to iron overload in hepatocytes that causes replicative arrest, senescence and ultimately necrosis and inflammation foci, and patients are at higher risk to develop liver fibrosis and cirrhosis [63]. But hepatic iron overload has been reported in other hepatic pathological conditions not related to gene mutations. Patients with alcoholic liver disease (ALD) often present increased iron levels [64], and this has been related to, among other mechanisms, hepcidin downregulation by alcohol, resulting in increased iron content in approximately 50% of patients [65]. In MASLD, a third of patients present also hepatic iron deposition, which appears to be associated with the pathogenesis of the disease. Meanwhile, iron depletion triggered improved metabolic alterations in these patients [66].

Despite this evidence, additional work is necessary to better understand whether iron overload is a general characteristic of chronic liver diseases, the relationship between iron accumulation and senescence and the underlying mechanisms by which these factors can facilitate fibrotic responses.

3. NADPH oxidases in liver disease

3.1. Structure and activity

The NADPH oxidases (NOX) family consists of seven members in most mammals, named NOX1-5 and DUOX1-2. These transmembrane enzymes transfer electrons from the NADPH to molecular oxygen, forming reactive oxygen species (ROS) as products. Although this family of enzymes is evolutionarily conserved,

being widely expressed in eukaryotes [67], and with evidence of homologues in procaryotes [68]; they present differences in structure, activity and the final ROS molecule generated [69]. All NOX/DUOX family members contain an homologous COOH-terminal domain with an NADPH binding site, a FAD-binding region, six conserved transmembrane α-helices and four heme-binding histidines [70]. However, differences in the mode of activity allow for the classification of the members of the family into three groups [71].

NOX1, NOX2 and NOX3 can be pooled into one group. These NOX proteins need to heterodimerize with a transmembrane protein named p22phox to be active. In addition, cytosolic proteins can bind to the transmembrane complex and regulate its activity. These regulators are organizers (p47phox and NoxO1) and activators (p67phox and NoxA1). The organizers facilitate assembling of other cytosolic subunits into the NOX complex. p47phox contains an autoinhibitory region that can be inactivated by phosphorylation allowing translocation to the membrane and binding to p22phox and p67phox, triggering the NADPH oxidase activity [72, 73]. NoxO1 is constitutively active although it can be modulated by phosphorylation and interacts with NoxA1, allowing for acute activation of ROS formation [74, 75]. p67phox interacts with another protein called p40phox that is considered activator of NOX2 [76]. Additionally, the G-protein Rac binds to the NADPH oxidase complexes of the members of this group to activate superoxide formation (**Figure 6**, [72]).

NOX5, DUOX1 and DUOX2 constitute another group of NADPH oxidases that do not bind to cytosolic factors but instead depend on the binding of Ca^{2+} to their intracellular EF-hand domains. DUOX1-2 require, however, the maturation and binding of the membrane factors DuoxA1 and DuoxA2, respectively [77]. While NOX5 produces superoxide, DUOX1-2 produce hydrogen peroxide probably because of the presence of a peroxidation domain in their structure (**Figure 6**, [71]).

NOX4 constitutes an independent group. Like NOX1-3, NOX4 requires the formation of a complex with p22phox to be stable and functional [78]. Traditionally, it has been considered to be constitutively active because no other regulatory proteins are known and therefore, modulated at the transcriptional level [79]. However, there have been reports of activation by a direct binding to Toll-like receptor 4 (TLR4) [80], Rac1-dependent activation under stimulation with angiotensin II and high glucose [81, 82] or negative regulation by phosphorylation by tyrosine kinase FYN [83]. In addition, NOX4 can be ubiquitinated by heat shock protein 70 (Hsp70) and others,

and thus degraded through the proteasomal system [84]. NOX4 releases hydrogen peroxide instead of superoxide since a special loop in its structure presents superoxide dismutase activity [85].

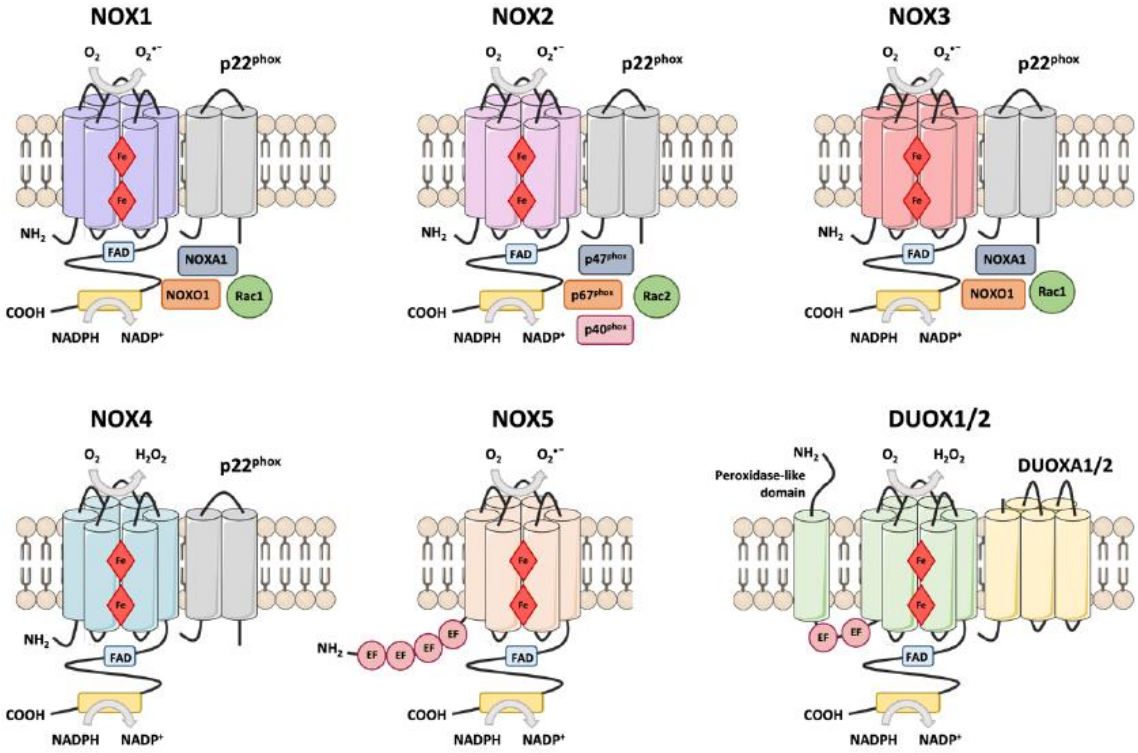

Figure 6. Representation of the NADPH oxidase family members. Image adapted from Vermot A. *et al.* [86].

The subcellular localization of NOX4 has been controversial, being described in the endoplasmic reticulum [87], the mitochondria [88], the plasma membrane, and even the nucleus [89]. On the one hand, these different localizations suggest a cell-type specificity or the expression of different NOX4 isoforms by different cells [90]. In terms of functionality, this might contribute to the compartmentalization of ROS generation and the interaction with specific proteins and related signalling pathways, which in turn could explain the wide variety of functions regulated by NOX4 among cell types. On the other hand, many of the experiments intended to localize NOX4 within the cell are performed in models that exogenously express high levels of the protein and thus, it may be difficult to precisely distinguish between accumulation at its synthesis site and its final location [69, 90]. The lack of specific antibodies recognizing NOX4 could also explain these differences [87].

3.2. Functions in liver disease

The ROS generated by NADPH oxidases are not mere by-products of a biochemical reaction, but rather serve specific functions in physiology and pathology. Dysregulation of NOXs expression or activity leads to pathological states such as cardiovascular diseases, cancer, diabetes and neurodegenerative diseases [91].

In the liver, NOX isoforms are distinctly expressed by different cell types and serve different functions. In hepatocytes, NOX1, together with Src, mediate the activation of the tumour necrosis factor (TNF)-α-converting enzyme/A disintegrin and metalloproteinase 17 (TACE/ADAM17), and therefore increases the shedding of different growth factors and cytokines, including the epidermal growth factor receptor ligands [92]. In endothelial cells, upon stimulation by Fas ligand or TNF-α, a translocation of NOX2 to the lamellipodia leading edge occurs, where a rearrangement of cytoskeleton induced by ROS facilitates cell migration [93]. NOX1 in macrophages mediates tumour progression by activation of inflammatory cytokines production, ultimately accelerating HHC development [94]. The generated superoxide by NOX2 during liver inflammation also induces hepatocyte DNA damage, which ultimately may contribute to tumour initiation and promotion [95]. Moreover, NOX1 has been found to support the metabolic switch responsible for lipids, proteins and nucleotides anabolism, necessary for cell growth, contributing to HCC [96]. In this regard, our group published that expression of NOX4 and NOX1-2 inversely correlate in HCC cells and when NOX4 is attenuated, the expression of NOX1/NOX2 is induced, producing a redox imbalance and metabolic reprogramming mediated by Nrf2/MYC that promotes HCC progression [97].

Many of the functions displayed by NOXs are governed by TGF-β, which regulates many aspects of liver biology in health and disease. In hepatocytes, our group demonstrated that NOX4 inhibits proliferation [98] and was required in TGF-β-induced apoptosis (**Figure 7**) [99], and deletion of NOX4 favours liver regeneration after partial hepatectomy [100]. Furthermore, the overactivation of survival signals, such as the MEK/ERK pathway impairs NOX4 upregulation, conferring resistance to TGF-β-induced cell death [101]. These results indicate that NOX4 functions as a tumour suppressor in HCC. However, we have recently published that NOX4 may also mediate protumourigenic actions, since it is required for the TGF-β-regulated cytoskeleton dynamics and focal adhesions. Concretely, NOX4 is necessary for the

increase in the chaperone Hsp27 and correct subcellular localization of Hic-5 within focal adhesions, as well for upregulation of the metalloprotease MMP9 [102].

3.3. NADPH oxidases in fibroblast activation

It has been well established that ROS are indispensable for the initiation of fibroblast activation in response to fibrotic insults in different organs, and accumulated evidence suggests that NOX4 is the source of ROS required in this process. Concretely, TGF-β, the most potent inducer of fibroblast activation, induces NOX4 expression, which mediates the fibrotic response in lung [103], kidney [104], heart [105], and prostate [106]. The mechanism by which TGF-β induces NOX4 expression and ROS generation in these organs is through the Smad2/3 pathway.

In the liver, our group and others obtained similar results, describing NOX4 upregulation and activation downstream TGF-β/Smad3 in HSC differentiation in mouse models of liver fibrosis [107, 108]. In fact, TGF-β ligands and NOX4 expression levels are increased in fibrotic patients [108, 109]. In addition to NOX4, other NOXs play a relevant role in hepatic fibrosis. It has been suggested that NOX1 promotes HSC proliferation through oxidation and inactivation of phosphatase and tensin homolog (PTEN), leading to the activation of AKT/FOXO4/p27(kip) [110]. Moreover, a study described that both NOX1 and NOX4 knockout mice presented attenuated liver fibrosis induced by CCl_4 [111]. Furthermore, NOX2 plays a key role in phagocytosis of apoptotic bodies by HSCs, which is known to induce collagen 1 expression and liver fibrogenesis *in vivo* (**Figure 7**) [112].

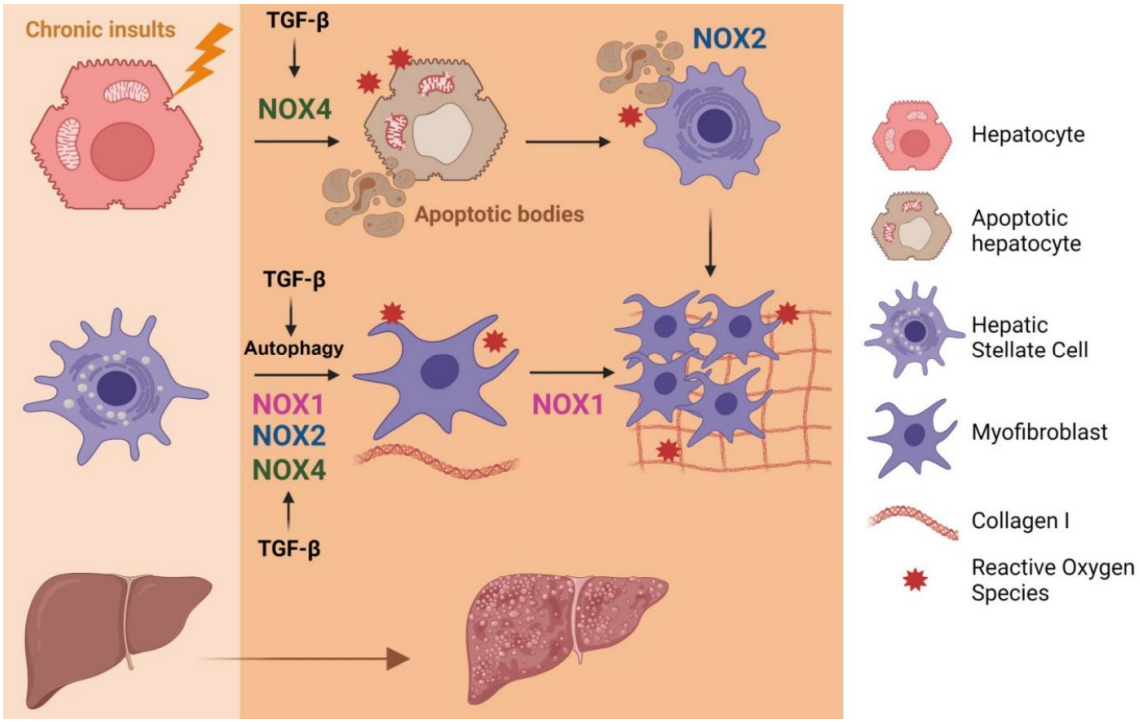

Figure 7. TGF-β/NOX axis in liver fibrosis. Activation of different NOXs by TGF-β contribute to activation of HSC towards myofibroblasts. TGF-β-induced NOX4 mediates hepatocyte apoptosis. Apoptotic bodies are phagocytosed by HSCs, a process that requires NOX2, which also contributes to their proliferation and activation. Extracted from Herranz-Itúrbide M. *et al.* [113].

II. HYPOTHESES

Iron accumulation and senescence mediate fibrosis progression in kidney and lung. In the liver, iron overload, specifically in hepatocytes, has been linked to hepatic diseases such as hereditary hemochromatosis, MASLD or ALD. Therefore, we hypothesized that iron and senescence could have a role in liver fibrosis progression, and in this context, an iron chelator could become a potential therapeutic approach.

Preliminary results from our group showed that in CCA, TGF-β has tumour suppressor effects. However, TGF-β has been linked to protumorigenic effects in the TME. Previous literature indicated that NOX4 plays a role downstream TGF-β in hepatic stellate cell activation towards matrix-producing myofibroblasts. This evidence suggested that NOX4 could be playing a role in CAF activation in CCA. Since CAF support and promote CCA progression and chemoresistance, we hypothesized that targeting NOX4 could have therapeutic effects.

III. OBJECTIVES

1. **Analysis of iron chelation as a new therapeutic approach in liver fibrosis.**
    1.1. To evaluate whether iron accumulates, correlating with characteristics of cell senescence, in a mouse model of liver fibrosis induced by CCl_4.
    1.2. Evaluation of iron chelation by deferiprone as a therapeutic approach for liver fibrosis *in vivo*.
    1.3. Analysis of the efficacy of deferiprone to attenuate iron accumulation and senescence *in vitro*.
    1.4. To explore the translational relevance of iron accumulation and senescence in the development of liver fibrosis in patients.

2. **Analysis of the potential therapeutic role of targeting NOX4 in hepatic stellate cell activation. Implications in cholangiocarcinoma.**
    2.1. Analysis of NOX4 expression in CCA tumour and stromal cells.
    2.2. Generation and characterization of a syngeneic orthotopic CCA model in wild type and $NOX4^{-/-}$ mice to evaluate the role of stromal NOX4 on tumour progression.
    2.3. Generation of loss of function experimental models of NOX4 in human hepatic stellate cells by CRISPR-Cas9 and siRNA to analyse transdifferentiation into myofibroblasts *in vitro*.
    2.4. Evaluation of the efficacy of NOX4 inhibitors on HSC transdifferentiation in *vitro*.
    2.5. Evaluation of the efficacy of NOX4 inhibitors on tumour progression in a murine AKT-YAP hydrodynamic tail vein injection CCA model.

IV. MATERIALS AND METHODS

1. Human samples

Human samples were collected with the required informed consent from each patient and the approval of the Institutional Review Board (Comité Ético de Investigación Clínica (CEIC), Bellvitge University Hospital (HUB)). Patients' written consent form and the study protocol conformed to the ethical guidelines of the 1975 Declaration of Helsinki.

Tissues from non-tumoral and tumoral areas were collected from patients during surgical procedures by Dr. Emilio Ramos (Department of Surgery, Liver Transplant Unit, University Hospital of Bellvitge, L'Hospitalet de Llobregat, Spain) and frozen at -80 °C and analysed at the gene expression level.

2. Cell lines and *in vitro* cultures

HH4 non-transformed human hepatocyte cell line was created in the Dr. Fausto lab (University of Washington School of Medicine, Seattle, WA, USA) [114]. LX2-HSC and hTERT-HSC cells derived from human HSC were kindly provided by Dr. Laura Fouassier (CRSA, Paris, France). HSC-GFP cells, commercial human primary HSC transfected with green fluorescent protein (GFP), were kindly provided by Dr. David G Molleví (IDIBELL, L'Hospitalet de Llobregat, Spain). HuCCT1 cells, derived from human iCCA, were kindly provided by Dr. Laura Fouassier. SB1 cells, derived from mouse iCCA, were kindly provided by Dr. Gregory J Gores and Dr. Sumera Ilyas (Mayo Clinic, Rochester, USA). All culture media and supplements were obtained from Gibco, Thermo Fisher Scientific (Waltham, MA, USA). HH4 cells were cultured in MEM (M2279) supplemented with non-essential amino acids (SH3023801, Cytiva) and L-glutamine (25030-024). SB1, LX2-HSC and hTERT-HSC cells were cultured in DMEM 4.5 g/l glucose (31966-021). HSC-GFP were cultured in DMEM/F-12 (10565018). HuCCT1 cells were cultured in DMEM 1 g/L glucose (21885-025), 10 mM HEPES (15630-056). All media were supplemented with 100 IU/mL penicillin and 100 µg/mL streptomycin (15140-122), 0.25 mg/mL amphotericin B (15290018) and 10% FBS (10270-106), except for HH4 that were cultured in 15% FBS. Cells were maintained in a humidified atmosphere at 37 °C containing 5% CO2. Immortalized cell lines were never used for experiments after more than 25 passages from receipt or resuscitation, except for HSC-GFP that were used under 12 passages from receipt because they are not immortalized.

2.1. CAF isolation and culture

Human primary CAF were isolated by outgrowth from tumoral tissue obtained from iCCA resections. CAF from Barcelona were from resections from Hospital Clinic de Barcelona, under the HCB/2021/0732 ethical approval from the Hospital Clinic ethics committee. In the case of CAF from Paris, the Committee for Personal Protection of Nord Ouest I (CPP) gave a favourable opinion on 11 April 2024 (National number: 2019-A01679-48 / SI number: 19.01424.061615-MS03.1 / Internal ref: APHP190473). Participants signed an informed consent during the inclusion visit. CAFs were maintained in DMEM Glutamax 10% FBS 1% Penicillin/Streptomycin and were used between passages 3 and 10.

Primary CAF derived from 3 different patients (2 patients from Barcelona and 1 from Paris) were plated independently in a 12-well plate and were maintained in DMEM Glutamax 10% FBS 1% Penicillin/Streptomycin. When reaching 70% confluence, cells were starved using DMEM Glutamax 1% FBS 1% Penicillin/Streptomycin overnight and were treated with vehicle (DMSO), TGF-β (2 ng/mL, T7039, Sigma-Aldrich), setanaxib or the combination of both. After 48 h, cells were collected in lysis buffer (RIPA Buffer 1x (Sigma-Aldrich), Protease Inhibitor (Roche) and Phosphatase inhibitor (Roche)), for protein extraction.

2.2. Spheroids formation

Spheroids were created using the hanging drop method. For all the experiments, cells were suspended at a concentration of 300.000 cells/mL for tumour cells alone or 300.000 + 300.000 cells/mL for mixed spheroids containing tumour cells and HSC-GFP cells in a 1:1 ratio. Cells were suspended in medium with 0,24% of methylcellulose (M7027, Sigma-Aldrich) in the absence or presence of setanaxib (40 µM). Twenty-five µl drops were pipetted onto the lid of 100 mm plates, that were inverted over plates containing 5 ml of cell culture medium to prevent drying. After 4 days of incubation at 37 °C and 10% CO_2, spheroids were transferred by pipetting onto a low-attachment 6-well culture plate (3471, Corning). Images of 10–20 spheroids per experiment were acquired with a NIKON Eclipse Ti2 microscope and spheroids size was measured with ImageJ software (National Institute of Health, USA).

2.3. Senescence models

The hepatocyte HH4 cells were plated in MEM with 15% FBS and after 24 h, medium was replaced by fresh medium with 2% FBS. Twenty-four hours later, treatments were initiated, and cells were cultured for 6 days more. Treatments were as follows: vehicle; 50 nM doxorubicin (S1208, Selleck Chemicals, Cologne, Germany) as senescent inducer; 50 µM deferiprone (379409, Sigma-Aldrich); and doxorubicin + deferiprone. Culture media and treatments were refreshed after 3 days (**Figure 8A**). The HSC LX-2 cells were cultured in DMEM with 10% FBS, and 24 h later, medium was replaced by fresh medium containing 0.5% FBS. The following day, cells were treated with vehicle, 2 ng/mL TGF-β, 50 nM doxorubicin or 80 µM deoxycholic acid (DCA, ref. D6750, Sigma-Aldrich) as senescence inducers, or both TGF-β and the senescent inducer in the absence or presence of 20 µM deferiprone and maintained for 6 days, refreshing the media and treatments after 3 days (**Figure 8B**).

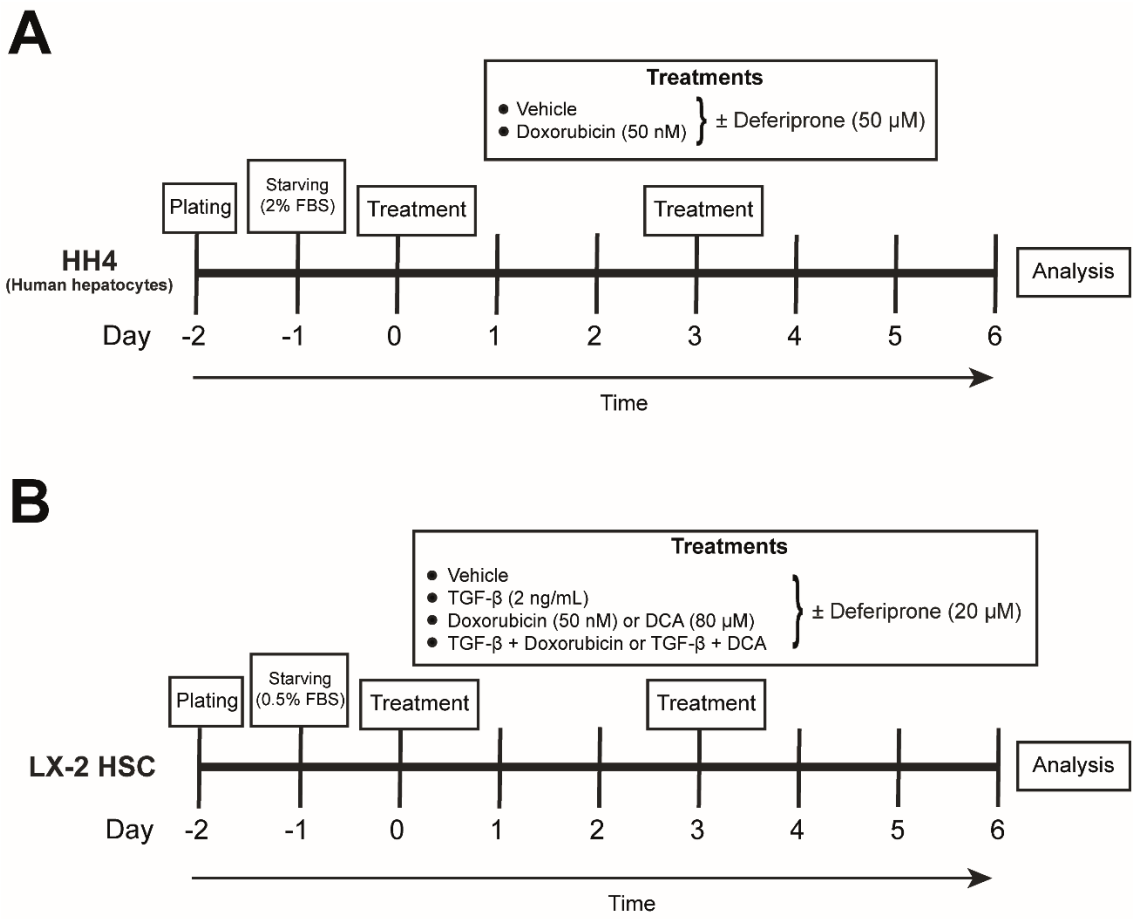

Figure 8. Schematic representation of the experimental designs for *in vitro* cellular senescence induction. **A.** The human hepatocyte cell line HH4 was cultured in MEM with 15% FBS and 24 h later starved with 2% of FBS. The next day (day 0), cells were treated with doxorubicin (50 nM) for 6 days to induce senescence and co-treated in the presence or absence of deferiprone (50 µM) for different analyses. **B.** LX-2 cell line was cultured in DMEM with 10% FBS and 24 h later starved with DMEM 0.5% FBS. The following day (day 0), cells were treated with vehicle, TGF-β (2 ng/mL), doxorubicin (50 µM) or deoxycholic acid (DCA, 80 µM) as senescent inducers, or the combination of TGF-β and the senescence inducer and maintained for 6 days in presence or absence of deferiprone (20 µM). Both in A and B, media and treatments were refreshed at day 3.

2.3.1. SA-β-GAL staining

Cells were stained for senescence-associated β-galactosidase activity with a commercial kit (#9860, Cell Signaling Technology, Danvers, MA, USA), following manufacturer's instructions. Staining of mouse liver tissue was done as stated in Maus et al. [62].

2.4. NOX4 loss-of-function CRISPR/Cas9 cell model

To generate a pool of hTERT-HSC cells lacking NOX4 protein, we used the CRISPR/Cas9 system. Two short-guide RNAs (gRNA) had been previously designed to target the human NOX4 gene and then cloned into the pSpCas9(BB)-2A-puro vector (Addgene, Watertown, MA, USA) by Dr. Noel P. Fusté (IDIBELL) and Dr. Gabriel Pons (University of Barcelona). The sequences of these gRNAs, identified as #1 and #2, are listed in **Table 1**. The vector encoded an RNA polymerase III promoter for the transcription of the guide, the Cas9 endonuclease, and a gene providing resistance to puromycin. hTERT-HSC cell line was transfected for two hours with a mix of plasmids containing the gRNA #1 and #2 in a 1:1 ratio using Lipofectamine® 2000 Reagent (11668-027, Thermo Fisher Scientific), generating the hTERT CRISPR-NOX4 cell line. An empty vector without gRNA was used as negative control, yielding the CRISPR-Control cell line. Cells were allowed to recover from the transfection process for 48 hours and then puromycin was added for an additional 48 h at 2 µg/mL for selection.

Table 1. Guide RNA sequences targeting *NOX4* human gene.

Guide RNA	Forward (5' – 3')	Reverse (5' – 3')
#1	CACCGGGTAGTGATACTCTGGCCCT	AAACAGGGCCAGAGTATCACTACCC
#2	CACCGTCACTACCTCCACCAGATGT	AAACACATCTGGTGGAGGTAGTGAC

2.5. RNA silencing

In addition to the NOX4 stable loss-of-function model generated with CRISPR/Cas9 technology, we performed transient downregulation of *NOX4* and *NOX1* by using small interfering RNA (siRNA) sequences (**Table 2**). Transfections were performed with 100 nM siRNA using DharmaFECT 4 (T-2004-03, Thermo Fisher Scientific). Cells were seeded in 6-well plates and 24 h later were transfected with the corresponding siRNA. The next day, cell culture media was changed to remove transfection complexes. Then, the appropriate protocol for each experiment was followed.

Table 2. siRNA sequences for transient gene expression downregulation.

Gene	Sense sequence (5' – 3')
NOX1	ACAAGCUGGUGGCCUAUAU
NOX4	GCCUCUACAUAUGCAAUAA
Control	GUAAGACACGACUUAUCGC

3. Animal models

All procedures complied with the EU Directive 2010/63/UE for animal experiments and the institution's guidelines and were approved by the General Direction of Environment and Biodiversity, Government of Catalonia (#4589, #6292) and the Ethical Committee for Animal Experimentation at IDIBELL, with the number EST-FOR-90.01.

Experimental groups included animals from different breedings and were randomly allocated to the different groups before starting the experiment. Investigators' blindness to group allocation during the experiment was not possible due to procedural reasons.

3.1. Carbon tetrachloride-induced liver fibrosis

Carbon tetrachloride (CCl_4) is one of the most used hepatotoxins to induce liver fibrosis. CCl_4 is metabolically activated in hepatocytes by P450 cytochromes forming trichloromethyl (CCl_3) radicals, which trigger hepatocyte injury and death. In response to this damage, macrophages are activated and/or recruited, leading to the

release of pro-fibrotic and pro-inflammatory cytokines that trigger the activation and expansion of HSC and the development of fibrosis [115].

To generate this model, CCl_4 (289116, Sigma-Aldrich, St. Louis, MO, USA) was diluted in ultrapure mineral oil (M5310, Sigma-Aldrich) and injected intraperitoneally twice a week for 4-8 weeks (480 mg/kg) into 8-weeks old male C57BL/6J mice (schematized in **Figure 9A**). To assess the potential of deferiprone as a therapeutic molecule, another experiment was performed where one week after the first CCl_4 injection, half of the animals of both mineral oil and CCl_4 groups received 1 mg/mL deferiprone dissolved in the drinking water until the end of the experiment at 4 weeks. Mice were sacrificed 3 days after the last CCl_4 injection and liver samples were collected (**Figure 9B**).

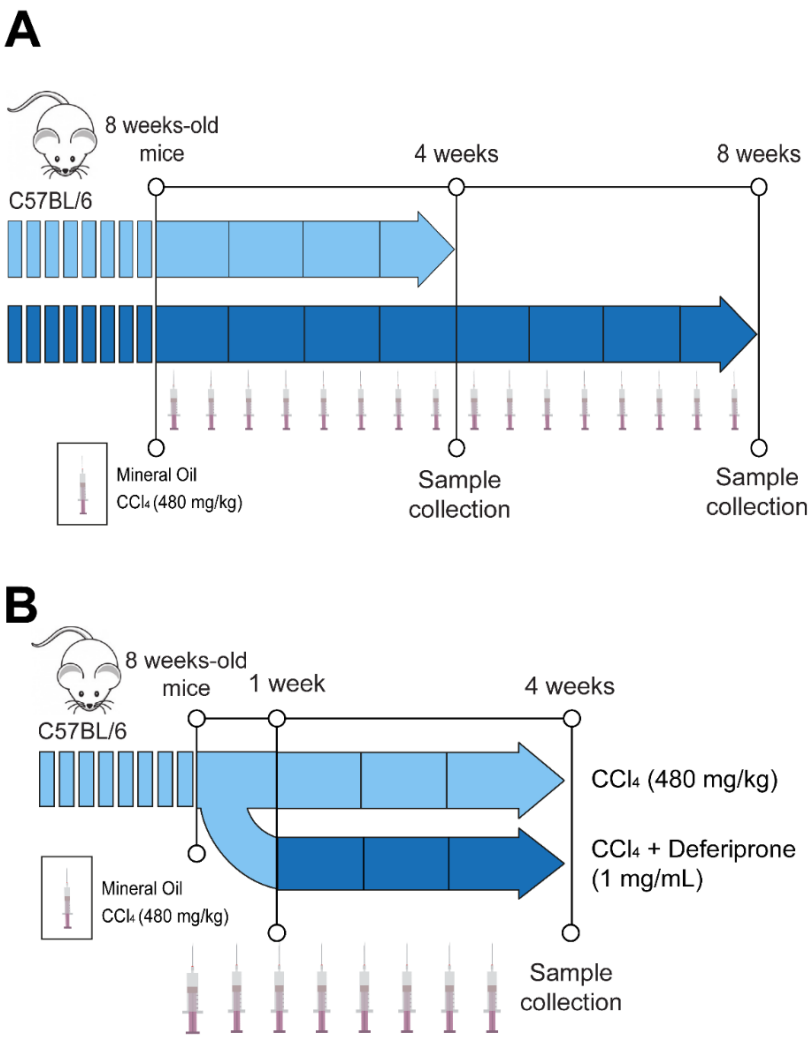

Figure 9. Generation of a CCl_4-induced liver fibrosis murine model. **A.** Eight-weeks old mice (C57BL/6 strain) were injected intraperitoneally twice a week with a CCl_4 solution (480 mg/kg of body weight) or vehicle (mineral oil). After 4 or 8 weeks, mice were sacrificed, and liver tissues were collected for analysis. **B.** To evaluate deferiprone as a potential therapeutic drug in a model of CCl_4-induced liver fibrosis, mice were injected intraperitoneally with CCl_4 (480 mg/kg) or mineral oil (M. Oil) twice a week for 4 weeks. A subgroup of both the control (M. Oil) and CCl_4-injected mice received deferiprone 1 mg/mL in the drinking water from 1 week after the first injection until the end of the experiment.

3.2. Syngeneic, orthotopic mouse model of CCA

NOX4−/− (B6.129-Nox4tm1Kkr/J) mice, generated in Dr. Krause's Laboratory (University of Geneva, Geneva, Switzerland) [116], were obtained from Jackson Laboratories (together with C57BL/6J mice, the appropriated controls, as suggested by the provider) and housed at IDIBELL. Murine SB1 CCA cells derived from an oncogene-driven murine model of CCA were maintained in culture medium, as previously described [117]. Under deep anaesthesia induced by isoflurane (IsoFlo 250 mL, Zoetis, Parsippany, NJ, USA), the abdominal cavity was opened by a 1 cm incision below the xiphoid process. Using a 27-gauge needle, 40 µL of standard media containing 500.000 SB1 cells were injected into the lateral aspect of the medial lobe. Subsequently, the abdominal wall and skin were closed in separate layers with absorbable chromic 3-0 gut suture material. Four weeks following SB1 cell implantation, mice were sacrificed, and tumour and adjacent liver tissues were collected for the different analyses (**Figure 9**).

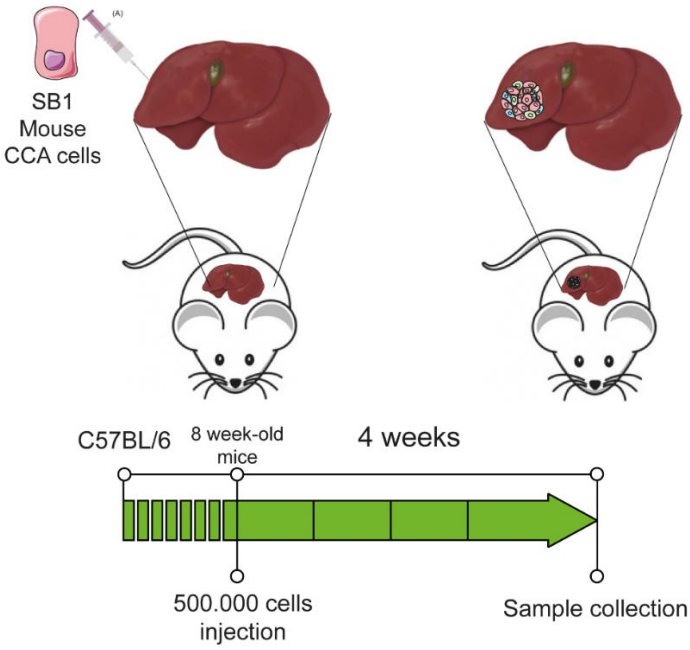

Figure 10. Generation of a syngeneic orthotopic intrahepatic cholangiocarcinoma murine model. Schematic representation of the experimental procedure is shown. Eight-weeks old mice from the C57BL/6 strain, both NOX4 knockout or wild type were injected with 500.000 SB1 mouse CCA cells in the liver parenchyma. Tumours were allowed to grow for 4 weeks and then mice were sacrificed and tissue samples from the tumour and non-tumoral liver were collected for analysis.

3.3. Hydrodynamic tail vein injection model of CCA

Wild-type male FVB/N mice were purchased from Charles River (Charles River Laboratories Les Oncins, France). The hydrodynamic injection was performed as described previously [118]. Briefly, 20 µg pT3-EF1α-HA-myr-AKT and 20 µg pT3-EF1α-YapS127A (AKT-YAP model) with 2 µg pCMV/sleeping beauty transposase

(SB) were diluted in 2 mL of saline (0.9% NaCl), filtered through 0.22-µm filter, and injected into the lateral tail vein of 6- to 8-week-old mice in 5 to 7 seconds. Four weeks after the injection, when the tumours were developed, 60 mg/kg of setanaxib or the vehicle (1% (w/v) carboxymethylcellulose (C9481 Sigma-Aldrich, 0.25% (v/v) Tween80 (59924 Sigma-Aldrich), and 0.05% (v/v) Antifoam (59920C Sigma-Aldrich,) in purified water) were daily administered through oral gavage to the mice during two weeks prior to sacrifice for the obtention of tissue samples (**Figure 11**).

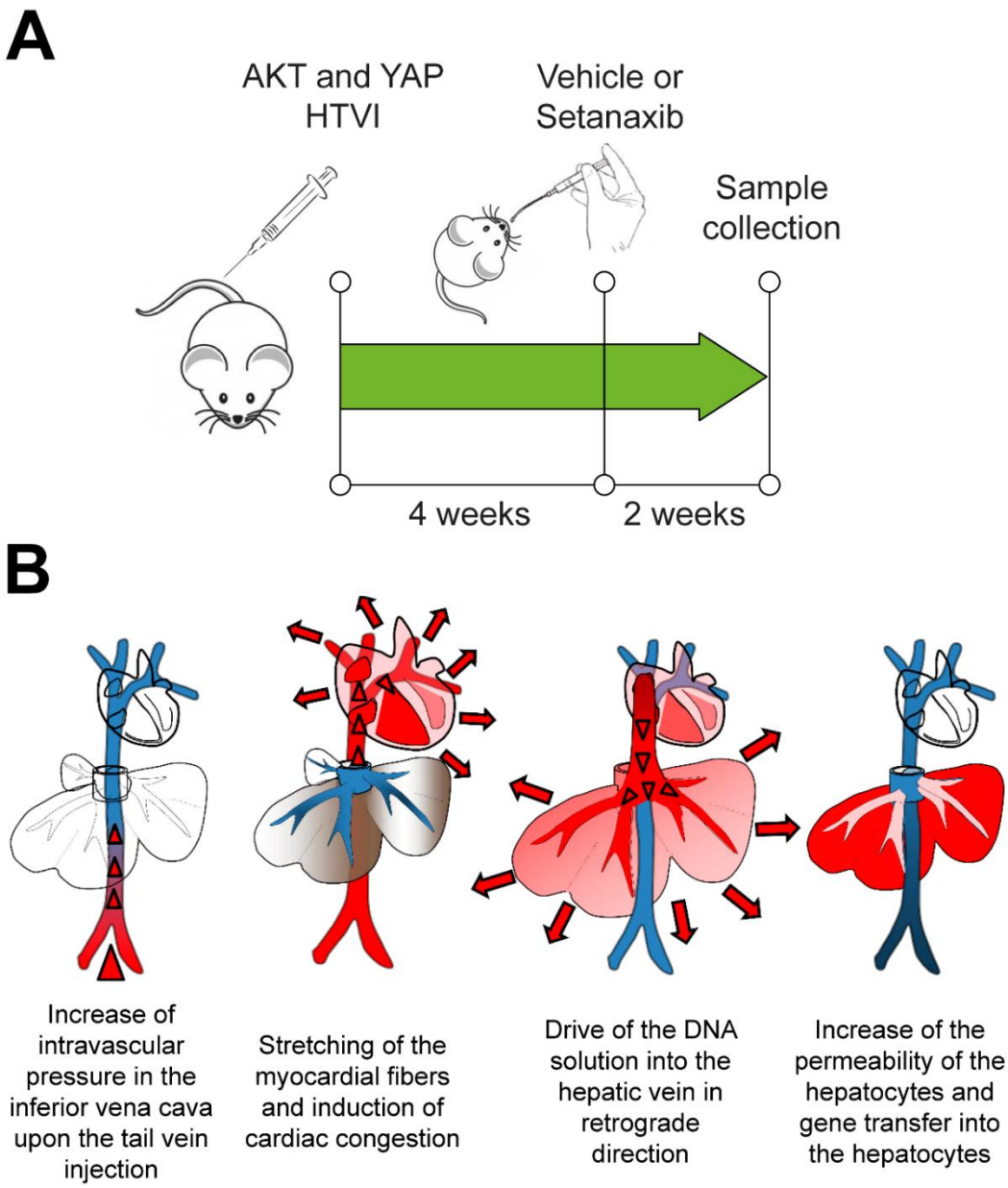

Figure 11. Generation of a CCA mouse model by hydrodynamic tail vein injection of AKT-YAP vectors. A. Schematic representation of the protocol. **B.** Description of the mechanisms of hydrodynamics-based delivery to the liver extracted from Kamimura K. *et al.* [119].

4. Gene expression analysis

4.1. RT-qPCR

Total RNA was isolated from the different cells or tissues using EZNA Total RNA Kit II (Omega Bio-tek, Norcross, GA, USA) following manufacturer's instructions. cDNA was produced using the High-capacity cDNA Reverse Transcription Kit (Applied Biosystems, Waltham, MA, USA). RT-qPCR was performed in duplicate in a Light Cycler 480 II (Roche) using PowerUp™ SYBR™ Green Master Mix (Applied Biosystems) in 384-well plates. Primer sequences are listed in **Tables 3 and 4**.

Table 3. Mouse primer sequences used for RT-qPCR.

Gene	Forward (5' – 3')	Reverse (5' – 3')
Acta2	TCACCATTGGAAACGAACGC	CCCCTGACAGGACGTTGTTA
Col1a1	GAAACCCGAGGTATGCTTGA	GACCAGGAGGACCAGGAAGT
Hfe	CTCAAAGCTGATGCCTCTGGA	CCAAGCCAAATGACAGCTTCC
Krt19	CCCTCCCGAGATTACAACCA	GGCGAGCATTGTCAATCTGT
Rpl32	ACAATGTCAAGGAGCTGGAG	TTGGGATTGGTGACTCTGATG
Tf	AGAACCGCTGGTTGGAACAT	GCGCAGCCTTGACTGAAAAA
Tfrc1	GCACCACTCGCCCAAGTTAT	TGGAATCCCATTATGCACGGT
Tfrc2	GGACTACTTGCAGAGTTCAGG	TTCCACGCGTCTGTAGATGG

Table 4. Human primer sequences used for RT-qPCR.

Gene	Forward (5' – 3')	Reverse (5' – 3')
ACTA2	AGAGTTACGAGTTGCCTGATG	GCTGTTGTAGGTGGTTTCATG
CDKN1A	CCAGCATGACAGATTTCTACCAC	GATGTAGAGCGGGCCTTTGA
COL1A1	CCCCTGGAAAGAATGGAGATG	TCCAAACCACTGAAACCTCTG
CYBA	TCCTGCATCTCCTGCTCTC	CACAGCCGCCAGTAGGTAG
CYBB	AGGAGTTTCAAGATGCGTGG	TTGAGAATGGATGCGAAGGG
DUOX1	CCTGCCTAAGGAACACACTC	GGGGCTCAGGGATTAGAATGTC
DUOX2	CAACCCTAATGTGGACCCCC	GTCGAGGACAATGGCACTGA
FN1	ACTGTACATGCTTCGGTCAG	AGTCTCTGAATCCTGGCATTG
GAPDH	AGCCACATCGCTCAGACAC	GCCCAATACGACCAAATCC
HAMP	TTTTCCCACAACAGACGGGA	CTCCTTCGCCTCTGGAACAT

HMOX1	AGACACCCTAATGTGGCAGC	ATGGCCGTGTCAACAAGGAT
KRT19	GCGAGCTAGAGGTGAAGATC	AATCCTGGAGTTCTCAATGGTG
NOX1	GCCTTGATTCTCATGGTAACTTCAGCTAC	ATTCATGCTCTCCTCTGTTTGACCC
NOX3	ATGGGACGGGTCGGATTGTT	ATCCATTTCCAAGCCGAGGGTTC
NOX4	GCAGGAGAACCAGGAGATTG	CACTGAGAAGTTGAGGGCATT
NOX5	CTGTATAACCAAGGGCCAGAG	AGGTAAGCCAAGAGTGTTCG
NOXA1	GGCTTCTTCCAGCGAGGAGT	CATTGTGTAGCACCTCCCAGGC
NOXO1	GTGCAGATCAAGAGGCTCCAAACG	CTTTGGGAGAACGCGGTCAGAT
RAC1	GCTTTTCCCTTGTGAGTCCTG	CCTTCAGTTTCTCGATCGTGTC
RPL32	AACGTCAAGGAGCTGGAAG	GGGTTGGTGACTCTGATGG
TFR1	TGAAGGTCTGACACGTCTGC	TGATGGTTCACTCACGGAGC

4.2. RNA-seq

4.2.1. RNA-seq of mouse hepatocytes

4.2.1.1. Isolation of mouse hepatocytes

Primary mouse hepatocytes were isolated as previously described [120]. Briefly, after 4 weeks of treatment (with mineral oil or CCl_4), livers were perfused with Hank's balanced salt solution supplemented with 10 mM Hepes and 0.2 mM EGTA for 5 min, followed by a 15 min perfusion with William's medium E containing 10 mM Hepes and 0.03% collagenase type 1 (125 U/mg; LS0041, Worthington Biochemical Corp, Lakewood, NJ, USA). Livers were further minced, filtered through a 70 µm cell strainer (BD Biosciences, Franklin Lakes, NJ, USA) and viable hepatocytes were selected by centrifugation in Percoll (17089101, Cytiva, Marlborough, MA, USA) and stored at -80 ºC.

4.2.1.2. Short-read RNA sequencing

Total RNA from *Mus musculus* was quantified by Qubit® RNA BR Assay kit (Thermo Fisher Scientific, Bremen, Germany) and the RNA integrity was estimated by using RNA 6000 Nano Bioanalyzer 2100 Assay (Agilent, Santa Clara, CA, USA). The RNA-seq libraries were prepared with KAPA Stranded mRNA-Seq Illumina® Platforms Kit (Roche, Basel, Switzerland) following the manufacturer's recommendations starting with 500 ng of total RNA as the input material. The library was quality controlled on an Agilent 2100 Bioanalyzer with the DNA 7500 assay. The

libraries were sequenced on NovaSeq 6000 (Illumina, San Diego, CA, USA) with a read length of 2x151 bp, following the manufacturer's protocol for dual indexing. Image analysis, base calling and quality scoring of the run were processed using the manufacturer's software Real Time Analysis (RTA v3.4.4).

4.2.1.3. RNA-seq data processing and analysis

RNA-seq reads were processed using fastp v0.21 (23), including adapter removal, trimming of low-quality reads (Q<30) and removal of reads with undetermined bases. Afterwards, processed reads were aligned against Mus musculus reference genome using GENCODE release M32 (GRCm39) using STAR v2.7.9 (24) and quantification of aligned reads to TPM was done with RSEM v1.3.1 (25). Gene expression related to iron accumulation was analysed with a gene signature previously designed by Maus *et al.* [62]. Analysis of a SASP-related gene expression was analysed using two different gene signatures: Reactome and SenMayo (26). ROS and TGF-β signalling gene signatures were obtained from Hallmark collection. Oxidative phosphorylation was analysed using a gene signature (In-house) generated selecting genes that were in at least 2 out of the 3 oxidative phosphorylation signatures from MSigDB v2023.1 (Hallmark, WikiPathway, and Gene Ontology Biological Process collections).

4.2.2. RNA-seq of human HSC

4.2.2.1. HSC culture and RNA isolation

Human LX2-HSC and hTERT-HSC HSC cell lines were plated in 60 mm dishes in DMEM 4.5 g/l glucose (31966-021). HSC-GFP cells were cultured in DMEM/F-12 (10565018). All media were supplemented with 100 IU/mL penicillin and 100 µg/mL streptomycin (15140-122), 0.25 mg/mL amphotericin B (15290018) and 10% FBS (10270-106). The following day, cells were starved in the corresponding medium with 0.5% FBS for 24 h. Then, medium with 0.5% FBS was refreshed, and cells were treated with setanaxib (40 µM) or the vehicle (DMSO) for 48 h. For RNA extraction, cells were washed with 1x PBS and collected through 0.05% trypsin digestion followed by centrifugation. Total RNA was isolated from the different cells using the EZNA Total RNA Kit II (Omega Bio-tek, Norcross, GA, USA) following manufacturer's instructions.

4.2.2.2. Short-read RNA sequencing

Total RNA quantification was performed using the Qubit® RNA BR Assay kit (Thermo Fisher Scientific), and the RNA integrity was assessed using the RNA 6000 Nano Bioanalyzer 2100 Assay (Agilent Technologies, Santa Clara, CA, USA). To prepare the RNASeq libraries, the KAPA Stranded mRNA-Seq Illumina Platforms Kit (Roche, Basilea, Switzerland) was used, following the manufacturer's recommendations with 500 ng of total RNA as the input material. Library quality was assessed on an Agilent 2100 Bioanalyzer using the DNA 7500 assay. The libraries were sequenced on the NovaSeq 6000 (Illumina, San Diego, CA, USA) with a read length of 2x151 bp, in accordance with the manufacturer's protocol for dual indexing. Image analysis, base calling, and quality scoring of the run were executed using the manufacturer's Real Time Analysis (RTA 3.4.4) software.

4.2.2.3. RNA-seq data processing and analysis

RNA-seq reads were trimmed using Trim Galore (https://github.com/FelixKrueger/TrimGalore), setting the length parameter at 35 and the stringency at 10. Trimmed reads were mapped against human reference genome (GRCh38) using STAR aligner version 2.7.8a [121] with ENCODE parameters, and annotated genes were quantified with RSEM version 1.3.0 [122] using GENCODE v42 as reference. Differential expression analysis was performed with limma v3.4.2 R package, using TMM normalization. The 'voom' function23 was used to estimate mean-variance relationship and to compute observation-level weights. The linear model was fitted for each cell line with the corresponding voom-transformed counts, and contrasts were extracted. Genes were considered differentially expressed (DEG) with a p-value adjusted below 0.05 and subsets of DEG were represented in heatmaps with the pheatmap R package, using voom-transformed counts scaled by row. A gene set enrichment analysis (GSEA) was performed on each list of genes pre-ranked by the limma moderated t-statistic, with the fgsea v1.12 R package [123], against the Reactome database.

5. Protein expression analysis

5.1. Tissue histopathological analysis

For analysis of collagen deposition, 5 µm-cut paraffin-embedded tissue sections were dewaxed and rehydrated in an Autostainer XL (Leica Biosystems, Deer Park, IL, USA) and stained with Picro-Sirius Red (Picric acid 197378; Direct-Red 80 365548, Sigma-Aldrich). To detect iron accumulation, enhanced Perl's Prussian Blue staining was performed as described previously [62]. To specifically identify activated myofibroblasts in the CCl_4-induced liver fibrosis model, anti-α-SMA primary antibody was diluted 1:50, incubated overnight at 4 °C and binding developed with the Vectastain ABC kit (PK-4001, Vector Laboratories, Burlingame, CA, USA). Nuclei were stained with haematoxylin solution (MHS32, Sigma-Aldrich) and preparations were mounted in DPX (100579, Sigma-Aldrich). p21 immunohistochemistry was done as described [62]. Slides were scanned on a virtual slide scanner NanoZoomer 2.0 HT (Hamamatsu, Tokyo, Japan) at the Histopathology Facility of Institute for Research in Biomedicine - IRB (Barcelona, Spain). For quantifying positive stained area, ImageJ analysis software v1.44o (National Institutes of Health, Bethesda, MD, USA) was used. Percentage of positive stained cells was quantified with QuPath software v0.4.4 (20).

For cytokeratin 19 (CK19) immunohistochemistry (IHC), antigen retrieval was achieved in TE buffer (pH 8.0), while sodium citrate buffer (pH 6.0) was used for all other targets. For α-SMA, Ki67, cCasp3, PD-L1 and CD4 immunodetection in the CCA models, slides were submerged in retrieval buffer and heated in a microwave on a high level for 10 minutes. After cooling down, slices were blocked with goat serum and the Avidin-Biotin blocking kit (Vector Laboratories, Burlingame, CA). Specimens were incubated with the designated primary antibody at 4 °C overnight. Subsequently, 3% hydrogen peroxide was applied for 10 min to quench endogenous peroxidase activity. Slices were incubated in the biotin-conjugated secondary antibody (Life Technology, Waltham, MA) at a 1:500 dilution for 30 min at room temperature. The Vectastain Elite ABC Kit (Vector Laboratories) and diaminobenzidine (DAB) substrates (Dako North America, Carpinteria, CA) were applied to visualise the immunostainings. Stained sections were scanned on a virtual slide scanner Pannoramic 1000 Flash RX® (Sysmex Europe SE, Norderstedt, Germany). Quantification of positive cells or positive-stained areas was performed using Slideviewer and ImageJ analysis software (National Institutes of Health,

Bethesda, MD, USA) respectively. Quantitative analyses were conducted in at least 10 tumours per mouse. In the case of intratumoral CD4 positive cells, only the inner area of the tumour was considered. All used antibodies are listed in **Table 5**.

5.2. Western blot

To analyse protein levels by Western blot, liver tissue or cultured cells were lysed in RIPA lysis buffer supplemented with a cocktail of protease inhibitors (11697498001, Roche Diagnostics, Rotkreuz, Switzerland) and 1 mM orthovanadate (S6508, Sigma) at 4 °C. Lysis of liver tissue was performed in a Tissue Lyser II (QIAGEN, Venlo, The Netherlands) and cells from in vitro cultures were scrapped. Protein concentration was determined using a Pierce™ BCA protein assay kit (Thermo Fisher Scientific). Proteins were denaturalized at 95 ºC for 5 min and separated with denaturalizing SDS-polyacrylamide gel electrophoresis (SDS-PAGE). Subsequently, transference to a nitrocellulose membrane in wet conditions was performed. For immunoblotting, membranes were incubated in 5% bovine serum albumin (A7906, Sigma) in PBS-Tween 0.05% for 1 h at room temperature. Afterwards, membranes were incubated with the primary antibodies, overnight at 4 °C. The next day primary antibodies were washed with PBS-Tween 0.05% and binding was developed with secondary antibodies diluted 1/2000 in PBS-Tween 0.05% (NA934V anti-Rabbit or NA931V anti-Mouse), incubated for 1 h at room temperature, followed by PBS-Tween 0.05% washes. Finally, positive hybridization was visualized with a chemiluminescent solution (GE HealthCare, Little Chalfont Amersham, UK) in a ChemiDoc™ Touch Imaging System (Bio-Rad, Munich, Germany). Densitometric analysis was performed using Image Lab™ software (Bio-Rad).

Table 5. Primary antibodies used for immunodetection.

Protein	Reference	Company	Source	Application	Dilution
α-SMA	ab5694	Abcam	Rabbit	WB, IHC	1:1000 – 1:2000, 1:50
α-Tubulin	T9026	Sigma	Mouse	WB	1:1000
β-Actin	A5441	Sigma-Aldrich	Mouse	WB	1:5000
CD4	CST 25229	Cell Signaling Technology	Rabbit	IHC	1:100
CK19	ab133496	Abcam	Rabbit	IHC	1:4000

COL1	PA2140-2	Boster Biological Technology	Rabbit	WB	1:2000
F4/80	CST 70076	Cell Signaling Technology	Rabbit	IHC	1:200
NOX1	ab55831	Abcam	Rabbit	WB	1:500
NOX4	A00403	Boster Biological Technology	Rabbit	WB	1:1000
p21	M7202	Dako-Agilent	Mouse	IHC	1:50
p22phox	TA334647	ORIGENE	Rabbit	WB	1:500
PDL-1	CST 64988	Cell Signaling Technology	Rabbit	IHC	1:100

WB: Western blot, IHC: immunohistochemistry.

5.3. Analysis of the SASP in liver tissue

Liver tissues were lysed in RIPA buffer and centrifuged to separate insoluble debris. Afterwards, protein concentration was determined using a Pierce™ BCA protein assay kit (Thermo Fisher Scientific) and adjusted so that all samples contained the same amount of protein. Samples were shipped to an external commercial laboratory (Eve Technologies Corp, Calgary, Canada) and a Mouse Cytokine/Chemokine 44-Plex Discovery Assay® Array (MD44) was performed.

6. Fluorescence-based methodologies

6.1. Detection of intracellular iron

Labile iron was measured using the FerroOrange probe (36104, Cell Signaling Technology) following manufacturer's instructions. A 24 h treatment with an aqueous solution of 330 µM iron sulphate (F8633, Sigma-Aldrich) and 330 µM iron nitrate (F8508, Sigma-Aldrich) was used as positive control. Representative images of the cells were taken with a Leica DM IRB Inverted Fluorescence Microscope (Leica Microsystems, Wetzlar, Germany). For analysis by flow cytometry, cells were detached and processed in a MoFlo Astrios Cell Sorter (Beckman Coulter) at the Biology-Bellvitge Unit from Scientific and Technological Centres (CCiTUB), University of Barcelona.

6.2. Analysis of ferroptosis by flow cytometry

Lipid peroxidation as a hallmark of ferroptosis was determined using the C11-BODIPY probe (D3861, Invitrogen, Carlsbad, CA, USA). Briefly, cells were incubated with 5 µM C11-BODIPY for 40 min. Then, both floating (dead) and attached (alive)

cells were collected for each condition and run on a GalliosTM Cytometer (Beckman Coulter) at the Biology-Bellvitge Unit from Scientific and Technological Centres (CCiTUB), University of Barcelona. The ferroptosis inducer RSL3 (S8155, Selleck Chemicals) was used at 2 µM as positive control and incubated overnight. To determine viability, cells were stained with 4′,6-diamidino-2-phenylindole (DAPI).

6.3. Hydrogen peroxide production

Extracellular hydrogen peroxide (H2O2) levels were detected using Amplex® Red assay kit (A36006, Invitrogen, Thermo Fisher Scientific). Cells were seeded on 12-well plates in DMEM with 10% FBS. The next day, cells were deprived of serum for 24 h in DMEM without phenol red (21063-029) at 0.5% FBS and cultured with the corresponding treatment for 24 h. Then, media was refreshed containing Amplex® UltraRed reagent (10 µM) and horseradish peroxidase (0.1 U/mLl). After 2 h incubation at 37 ºC, fluorescence was measured in duplicate in a BMG FLUOstar OPTIMA fluorescence plate reader (BMG Labtech, Ortenberg, Germany) with excitation and emission at 530 nm and 590 nm, respectively. H2O2 concentration was extrapolated using a standard curve and values were normalized to cell viability by crystal violet staining (61135, Sigma-Aldrich).

7. Analysis of public data bases

7.1. Fibrosis-related published data

Single-cell RNA-sequencing data from Yang et al. cohort [124] was accessed through GEO accession number GSE171904 and the processed Seurat object was used to quantify gene expression signatures in non-parenchymal liver cell types with the AddModuleScore function. Comparisons between conditions were assessed using Mann-Whitney U-test and adjusted for multiple comparisons.

Gene expression from acute CCl_4 damage in mouse hepatocytes was assessed using Godoy et al. cohort (accessed through ArrayExpress E-MTAB-4444) [125]. Raw data was downloaded and normalized using robust multi-array average (RMA) [126]. Additionally, mouse liver gene expression data from chronic CCl_4-bulk sequencing (Hammad *et al.* cohort, [127]) was also downloaded and normalized using RMA through Gene Expression Omnibus (GEO) accession number GSE222576.

To analyse human gene expression, Fujiwara *et al.* cohort of liver biopsies from HCC-naïve MASLD patients [128] was accessed through GEO accession number GSE193066. Relative log-expression normalized data was directly downloaded from GEO. Trepo *et al.* cohort of liver biopsies from HCC-naïve alcoholic steatohepatitis (ASH) and alcoholic cirrhosis patients [129] was accessed through GEO accession GSE103580 and raw data was downloaded and normalized using RMA.

For each cohort, a collection of gene signatures was obtained from MSigDB v2023 [130] and gene set variation analysis (GSVA) [131] was used to assess the relative activation of the signatures in the samples. Heatmaps showing relative activation for each gene signature were plotted using ComplexHeatmap package for R.

Correlation in human samples between two gene signatures was assessed using Pearson correlation. Kendall's τ was used to assess the association between the gene signatures and fibrosis stage in cohorts of patients. All p-values were adjusted for multiple testing with Bonferroni test correction. All analyses were performed using R v4.0.4 [132].

7.2. CCA-related published data

7.2.1. TCGA cohort

The mRNA expression levels of ACTA2, COL1A1 and NOX4 in non-tumoral tissue and CCA tumours from the repository of The Cancer Genome Atlas (TCGA) were analysed through the GEPIA database (http://gepia.cancer-pku.cn/) [133] and were represented as means ± SEM. The mRNA expression levels of NOX4 versus ACTA2 and COL1A1 in CCA tumours from the repository of TCGA were analysed through the cBioPortal database (https://www.cbioportal.org/) and represented as Spearman correlation coefficients (r) and P-values to assess the significance [134, 135].

7.2.2. TIGER-LC cohort

Raw microarray data was downloaded from GEO (accession ID: GSE76297) (TIGER-LC cohort) and processed using robust multiarray method implemented in the affy package version 1.56 available through the Bioconductor software project (https://bioconductor.org) using R v4.0.4.6 Probe-set to gene mapping was done

using the array annotation file available at Gemma database (https://gemma.msl.ubc.ca/arrays/showArrayDesign.html?id=785), selecting the most expressed probe as representative of gene expression when multiple mapping probes occurred to avoid duplicated genes. Comparison of median gene expression of NOX4 between tumoral and non-tumoral samples was done with Mann– Whitney U test.

7.2.3. Single-cell RNA-seq

The single-cell RNA-seq dataset was processed, analysed and visualized using the Trailmaker® (https://scp.biomage.net/) hosted by Biomage (https://biomage.net/). First, pre-filtered count matrices from Shi *et al.* (GSE201425) were uploaded to Trailmaker®. Briefly, to pre-process the data, barcodes with low unique molecular identifiers (UMIs) and or high mitochondrial reads were filtered out. Next, to exclude outliers, a robust linear model was fitted to all samples. Lastly, barcodes with high doublet scores were excluded from the analysis, resulting in high quality barcodes that were used in subsequent integration steps. Briefly, to integrate the barcodes, data were log-normalised and the top 2000 highly variable genes were selected. Next, principal component analysis (PCA) was performed, and the top 30 principal components, explaining 89.67% of the total variance, were used to perform sample batch correction with the integrated Harmony R package. Louvain method of clustering was employed. To reduce dimensionality, data was visualised using t-distributed stochastic neighbour embedding (t-SNE). To identify cluster-specific marker genes, the marker genes of each cluster were compared to all other clusters and appropriately annotated. The CAF subset identified from this analysis was further examined via the sample subset feature. Filtering steps were disabled (due to pre-filtered data) and the subset was analysed via the same integration steps outlined above.

7.2.4. Survival analyses

Survival analyses were conducted in the GSE244807 dataset, which had available gene expression and overall survival data for 246 patients with intrahepatic cholangiocarcinoma (iCCA) [136]. Kaplan-Meier curves were plotted, and hazard ratios and 95% confidence intervals were obtained from a Cox Proportional Hazards model adjusted for sex and age clinical covariates. GSVA was used to assess the relative activation of the setanaxib treatment signature in the samples [131]. Median

GSVA scores, in the case of signatures, or median gene expression value, in the case of individual genes (i.e., NOX1, NOX4), were used to stratify patients in low or high group, respectively. All analyses were performed using R 4.0.4.

7.2.5. Active CD4 T cells infiltration evaluation

Active CD4 T cell signatures were obtained from a previous study [137]. GSVA was used to assess the relative infiltration of CD4 T cells in the samples [131]. Differences in median CD4 T cell infiltration scores between setanaxib signature low and setanaxib signature high groups were tested using a Mann- Whitney U test. P-values were corrected for multiple testing with False Discovery Rate (FDR).

8. Statistical analysis

Results were analysed using the GraphPad Prism 5.0 statistical software (GraphPad Software, Boston, MA, USA). Data are shown as mean ± standard deviation (SD) or standard error of the mean (SEM), as indicated in each figure legend. For comparisons between two groups, parametric Student's t test or nonparametric Mann–Whitney tests were used. For multiple comparisons, one-way ANOVA was used with Sidak's correction. Differences were considered statistically significant when $p<0.05$.

V. RESULTS

1. Iron chelation as a new therapeutic approach to prevent senescence and liver fibrosis progression

1.1. Analysis of iron accumulation and senescence in a mouse model of liver fibrosis induced by CCl_4.

Liver fibrosis in mice was induced by CCl_4 chronic treatment for 4 or 8 weeks, as described in Material and Methods and schematized in **Figure 9A**. After euthanising the mice at the corresponding time point, liver tissues were collected and processed for histological examination. Collagen fibres, analysed by Picro-Sirius Red staining, and appearance of α-SMA positive areas, indicating the presence of activated myofibroblasts, were observed both after 4 and 8 weeks of treatment (**Figure 12**).

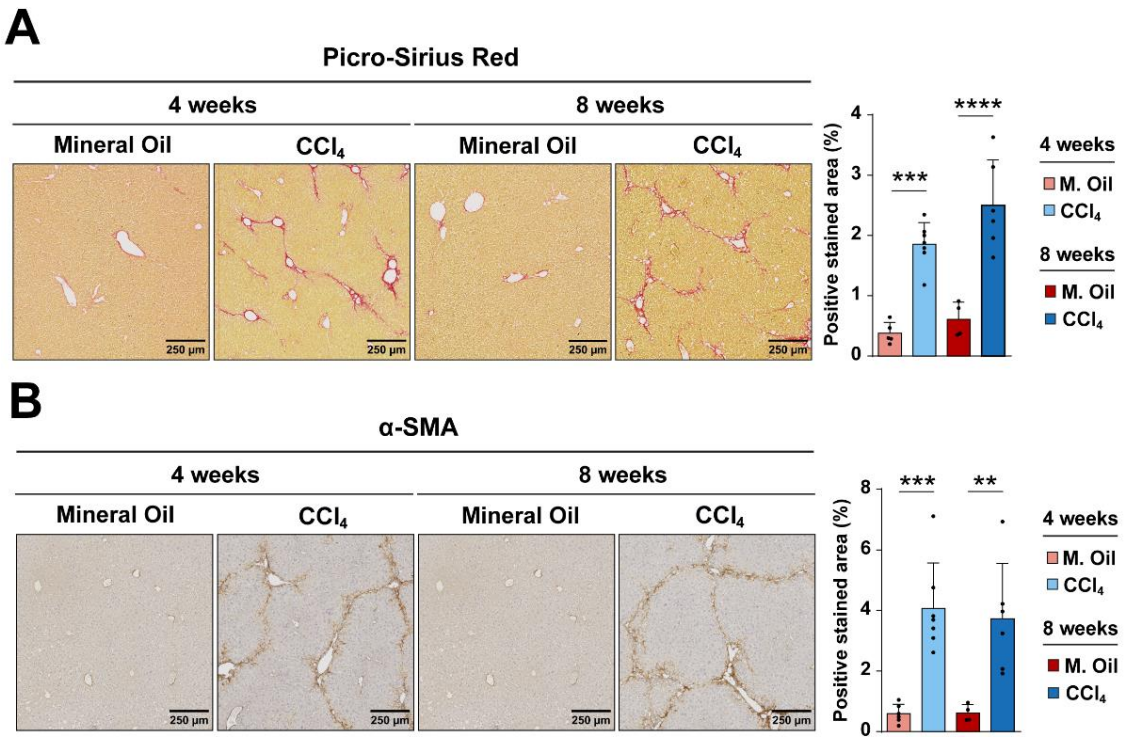

Figure 12. Characterization of fibrosis in a CCl_4-induced liver fibrosis mouse model at 4 and 8 weeks. A. Picro-Sirius Red staining was conducted to reveal collagen deposition. **B.** Immunostaining of α-SMA as a marker of myofibroblasts. Images of representative areas are shown. The percentage of positive stained area was calculated using ImageJ software. Each dot represents the arithmetic mean of the percentage of positive stained area from three different regions for each animal. Data are presented as mean (SD) for each group. Number of animals per group is as follows: M. Oil 4 weeks (5), CCl_4 4 weeks (7), M. Oil 8 weeks (4), CCl_4 8 weeks (6). Statistical analysis was done using GraphPad Prism software (two-tailed Mann-Whitney U-test). **p<0.01; ***p<0.001; ****p<0.0001.

Deposits of iron were observed too near the fibrotic areas (**Figure 13A**), as well as some positive cells for p21, a hallmark of senescence (**Figure 13B**). Importantly, a positive correlation between iron content and p21 was found after 4 weeks of CCl_4 treatment (**Figure 14**). These findings suggested a potential relationship between iron deposition and cellular senescence, which appeared to occur concomitantly with liver fibrosis progression.

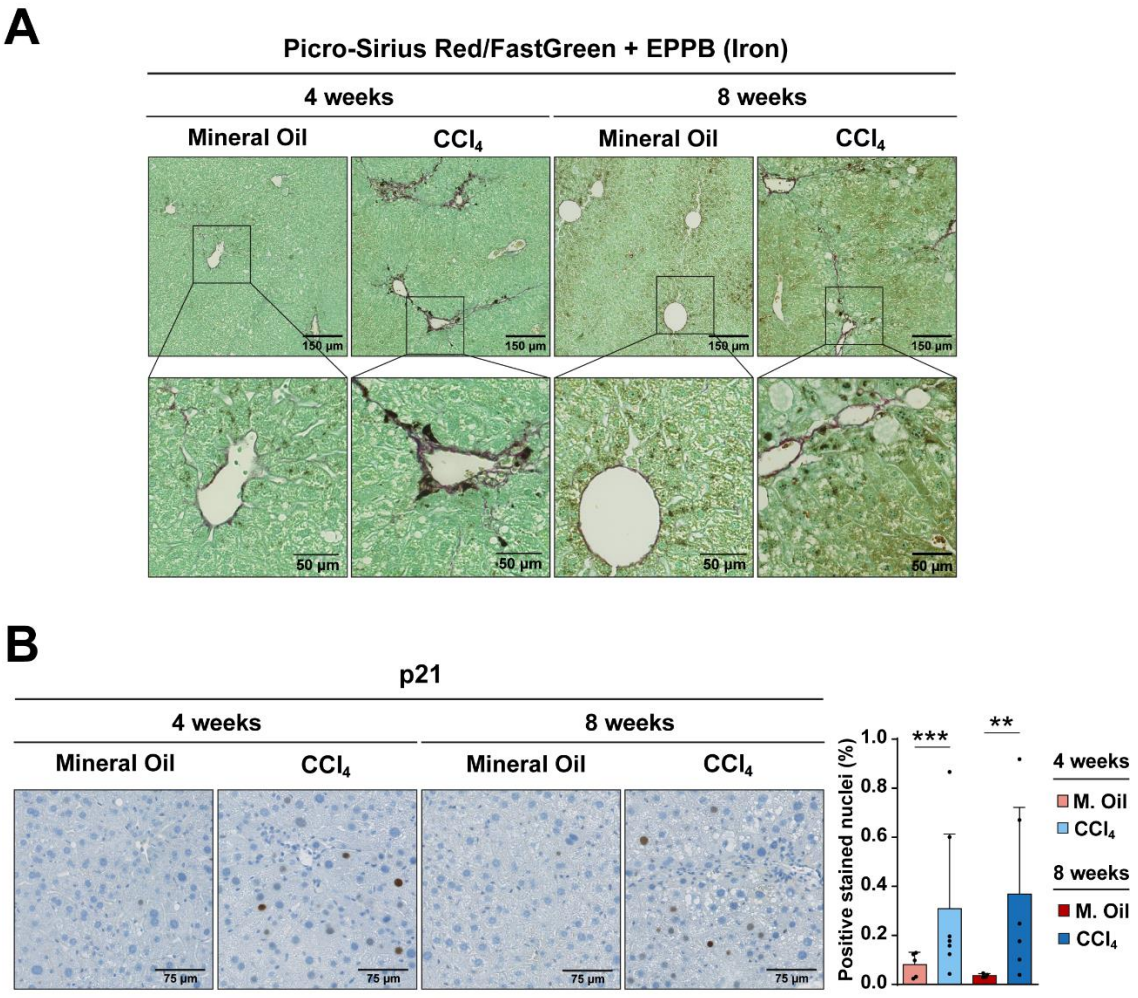

Figure 13. Characterization of iron accumulation and senescence in a CCl_4-induced liver fibrosis mouse model at 4 and 8 weeks. A. To simultaneously detect fibrotic areas and iron accumulation, Picro-Sirius Red/FastGreen staining was combined with enhanced Perl's Prussian Blue (EPPB). **B.** Immunohistochemistry for the senescent marker p21. Images of representative areas are shown. In B, percentage of positive nuclei were calculated using QuPath software. Each dot represents the percentage of positive nuclei quantified in a whole liver lobe for each animal. Data are presented as mean (SD) for each group. Number of animals per group is as follows: M. Oil 4 weeks (5), CCl_4 4 weeks (7), M. Oil 8 weeks (4), CCl_4 8 weeks (6). Statistical analysis was done using GraphPad Prism software (two-tailed Mann-Whitney U-test). *p<0.05; **p<0.01; ***p<0.001; ****p<0.0001.

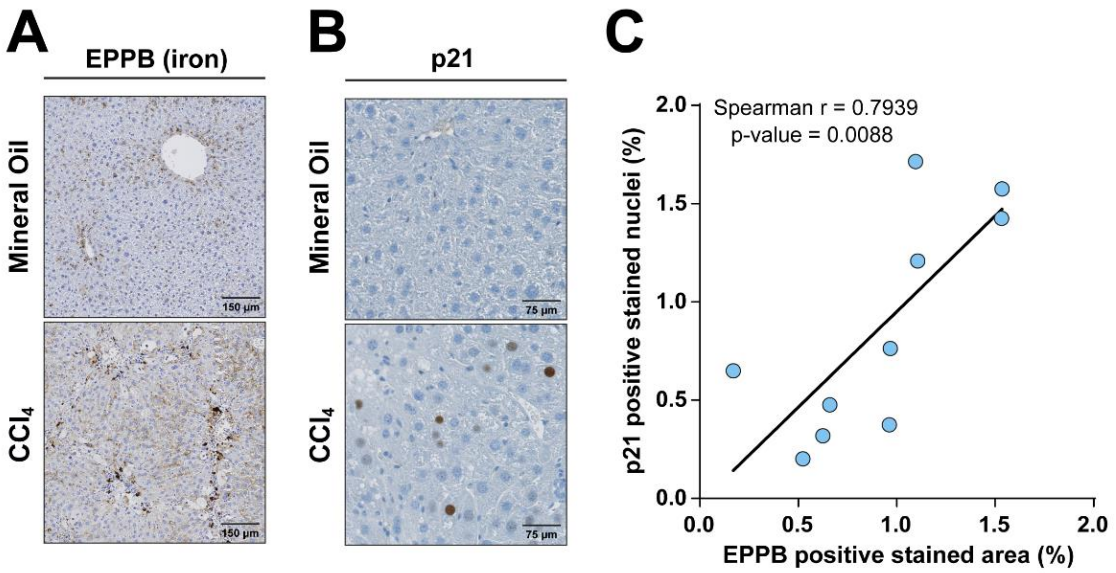

Figure 14. Correlation between iron accumulation and senescence in a CCl_4-induced liver fibrosis murine model at 4 weeks. **A.** Enhanced Perl's Prussian Blue (EPPB) staining for iron detection. **B.** Immunohistochemistry for p21 as a hallmark of senescence. **C.** Spearman correlation analysis between the percentage of area stained by EPPB and the percentage of positive nuclei for p21, as analyzed by IHC. In EPPB staining, three representative regions from different liver lobes of each animal were selected and the percentage of positive stained area was quantified with ImageJ analysis software v1.44o. Then, the arithmetic mean of the percentage of stained area of the three regions was calculated for each animal. The percentage of p21-positive stained cells was quantified with QuPath software v0.4.4 in a whole liver lobe for each animal. Each dot represents a different animal (n=10). Statistical analysis was done using GraphPad Prism software (Spearman's correlation analysis).

To have a better overview of the changes occurring in the liver upon fibrosis development and its relationship with iron metabolism and senescence, hepatocytes were isolated from mice after 4 weeks of CCl_4 injections and submitted to transcriptomic analysis by RNA-seq. The isolation of hepatocytes was done in the laboratory of Aránzazu Sánchez and Blanca Herrera (Complutense University of Madrid, Madrid, Spain) and samples were sequenced at Centre Nacional d'Anàlisi Genòmica (CNAG, Barcelona, Spain). The bioinformatic analysis of this RNA-seq and public transcriptomic data was performed by Ania Alay (ICO-IDIBELL, L'Hospitalet de Llobregat, Spain). We first explored iron metabolism in these samples and found a significant regulation in the expression of genes related to an iron accumulation gene signature designed by Maus *et al*. [62] (**Figure 15**), which correlated with induction of ROS-related genes and activation of the TGF-β pathway (**Figure 16**), as hallmarks of hepatocyte damage and a liver fibrotic process.

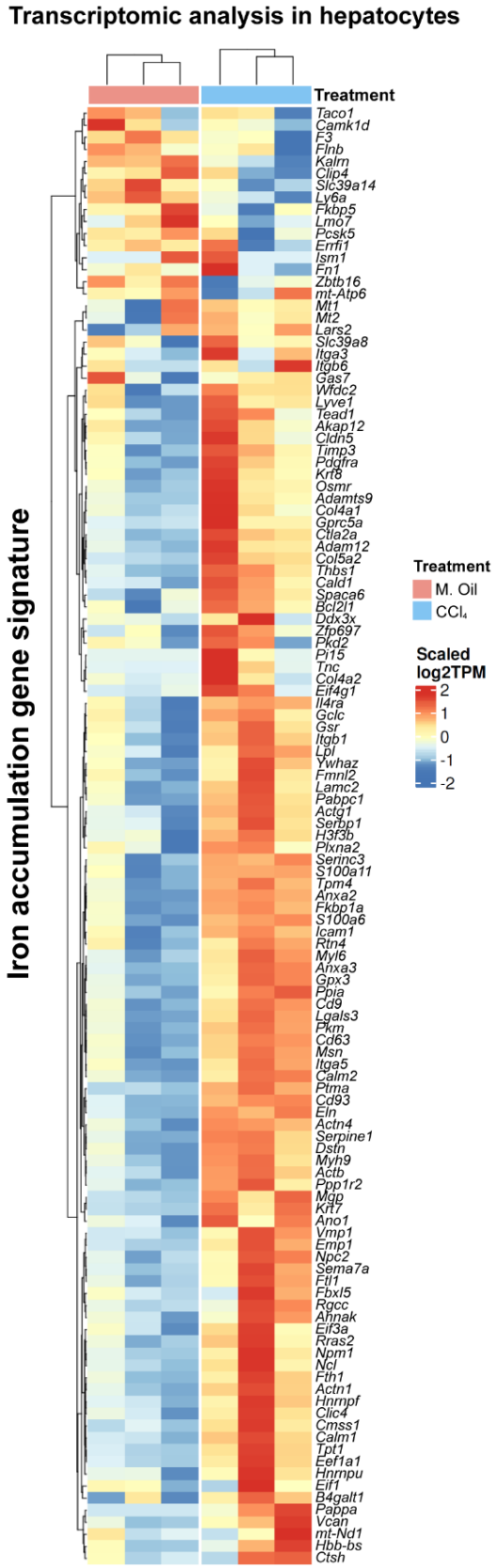

Figure 15. Analysis of an iron accumulation gene signature in hepatocytes from the CCl_4-induced liver fibrosis murine model. RNA-seq analysis was performed in hepatocytes isolated from mice treated with CCl_4 or mineral oil (M. Oil) for 4 weeks (n=3 mice/group) and a heatmap showing changes in gene expression for an iron accumulation gene signature (designed by Maus *et al.*, (19)) is presented.

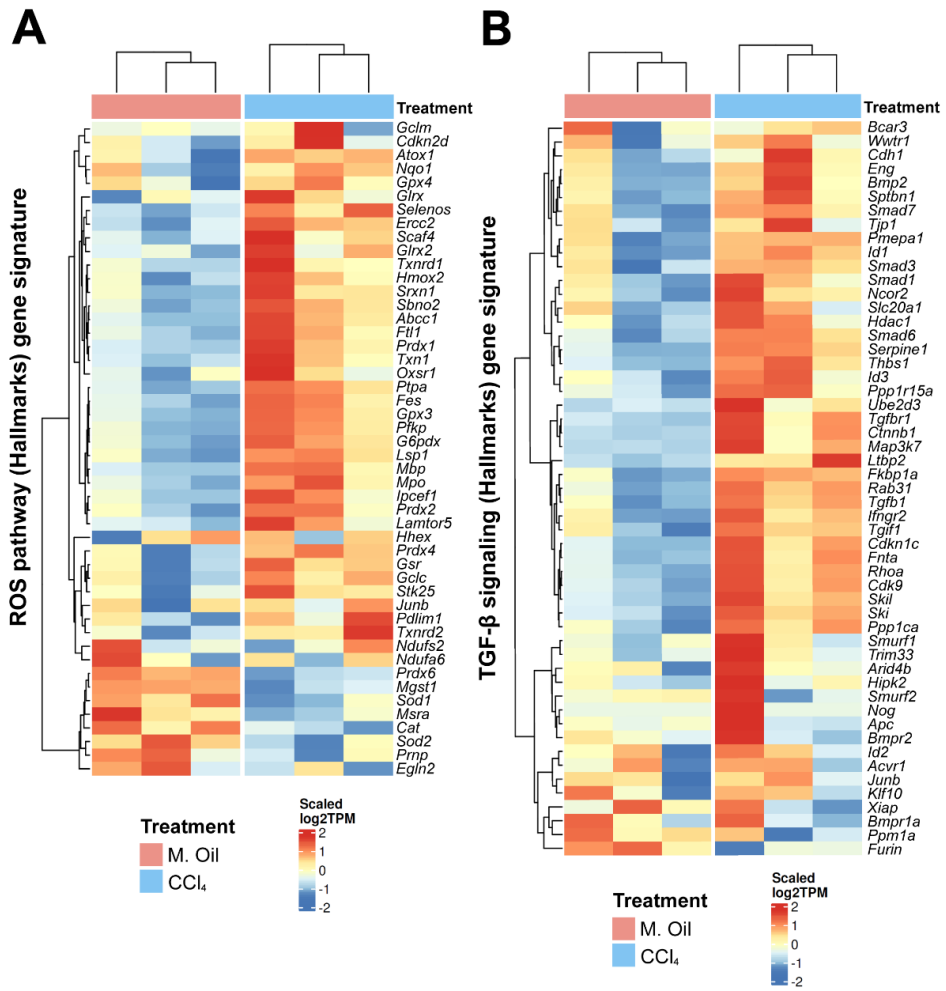

Figure 16. Analysis of fibrosis-related gene transcriptomes in hepatocytes from untreated or CCl_4-treated mice. RNA-seq analysis in hepatocytes from mice treated with CCl_4 or mineral oil (M. Oil) for 4 weeks (n=3 mice/group). Samples were tested for fibrotic hallmarks through ROS pathway (**A**) and TGF-β signaling (**B**) gene signatures from Hallmarks collection.

The analysis of a SASP-related gene expression, which was analyzed using two different gene signatures (Reactome and SenMayo [138]) that do not have any gene in common in mouse (**Figure 17A**), revealed an up-regulation in CCl_4-treated livers (**Figure 17B-C**).

To complement the transcriptomic data relative to the SASP gene signatures in hepatocytes with analysis at the protein level in the liver tissues, where the cytokines would be secreted, we sent the liver samples to a specialized company (EveTechnologies, Calgary, Canada) to explore the levels of a panel of 45 SASP-related cytokines. The results revealed an increase in some proteins that are regulators of immune cell fate, such as chemokines involved in the recruitment and stimulation of monocytes (IP-10, MCP-1, MCP-5), or leukocytes (MDC, Fractalkine)

(**Figure 18**), which reflected a role of fibrotic/senescent hepatocytes in regulating inflammation and immune microenvironment.

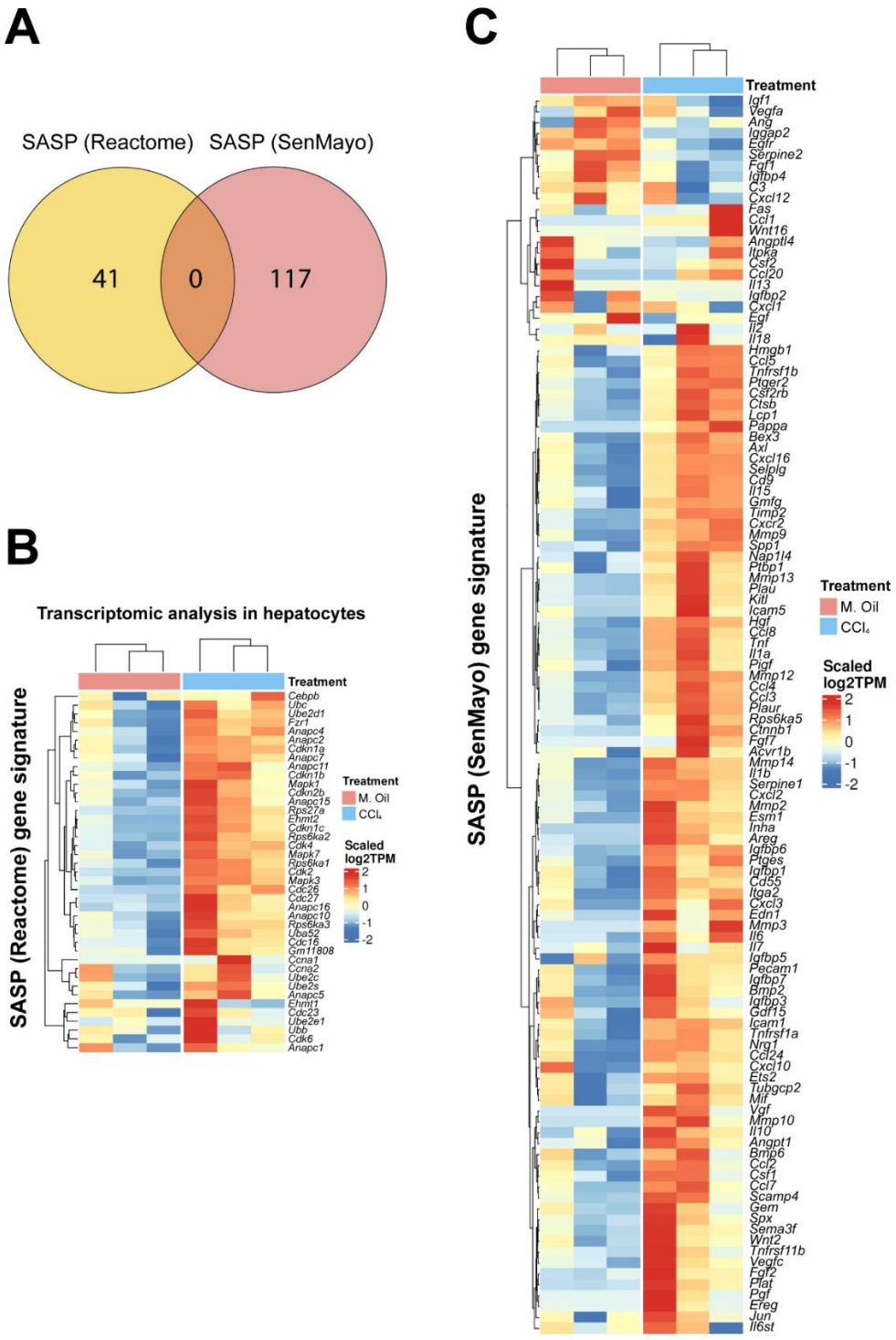

Figure 17. Analysis of SASP-related gene transcriptomes in hepatocytes from untreated or CCl_4-treated mice. RNA-seq analysis in hepatocytes from mice treated with CCl_4 or mineral oil (M. Oil) for 4 weeks (n=3 mice/group). **A.** Venn diagram showing the number of common mouse genes between the two SASP gene signatures (Reactome and SenMayo) tested in this study. **B.** Heatmap showing changes in gene expression of the SASP gene signature from the Reactome collection in hepatocytes from CCl_4-treated mice compared to controls. **C.** Heatmap showing changes in gene expression from the SASP SenMayo gene signature in the same samples.

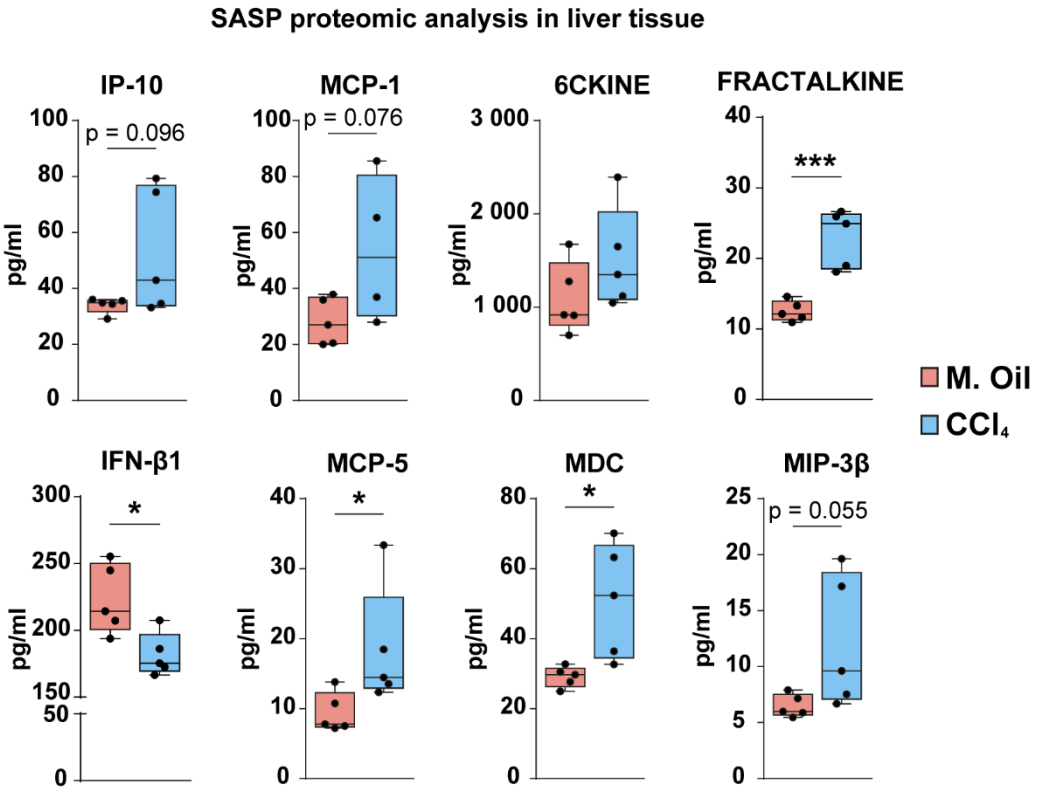

Figure 18. Analysis of SASP-related gene transcriptomes in hepatocytes from untreated or CCl_4-treated mice. Liver tissue was collected from mice treated with CCl_4 or mineral oil for 4 weeks and a panel of 45 SASP-related cytokines were quantified at the protein level (n=5 mice/group). A selection of some cytokines relevant for fibrosis are shown. Statistical analysis was done with two-tailed Mann-Whitney U-test. *p<0.05.

Metabolism dysregulation is a feature of senescent cells. In this regard, hepatocytes isolated from the CCl_4-treated mice also showed strong changes in metabolism-related gene expression, particularly oxidative phosphorylation and fatty acid oxidation pathways (**Figure 19A-B**). Overall, the activity of these pathways decreased coincident with the increase in iron accumulation and SASP pathways (**Figure 19C**).

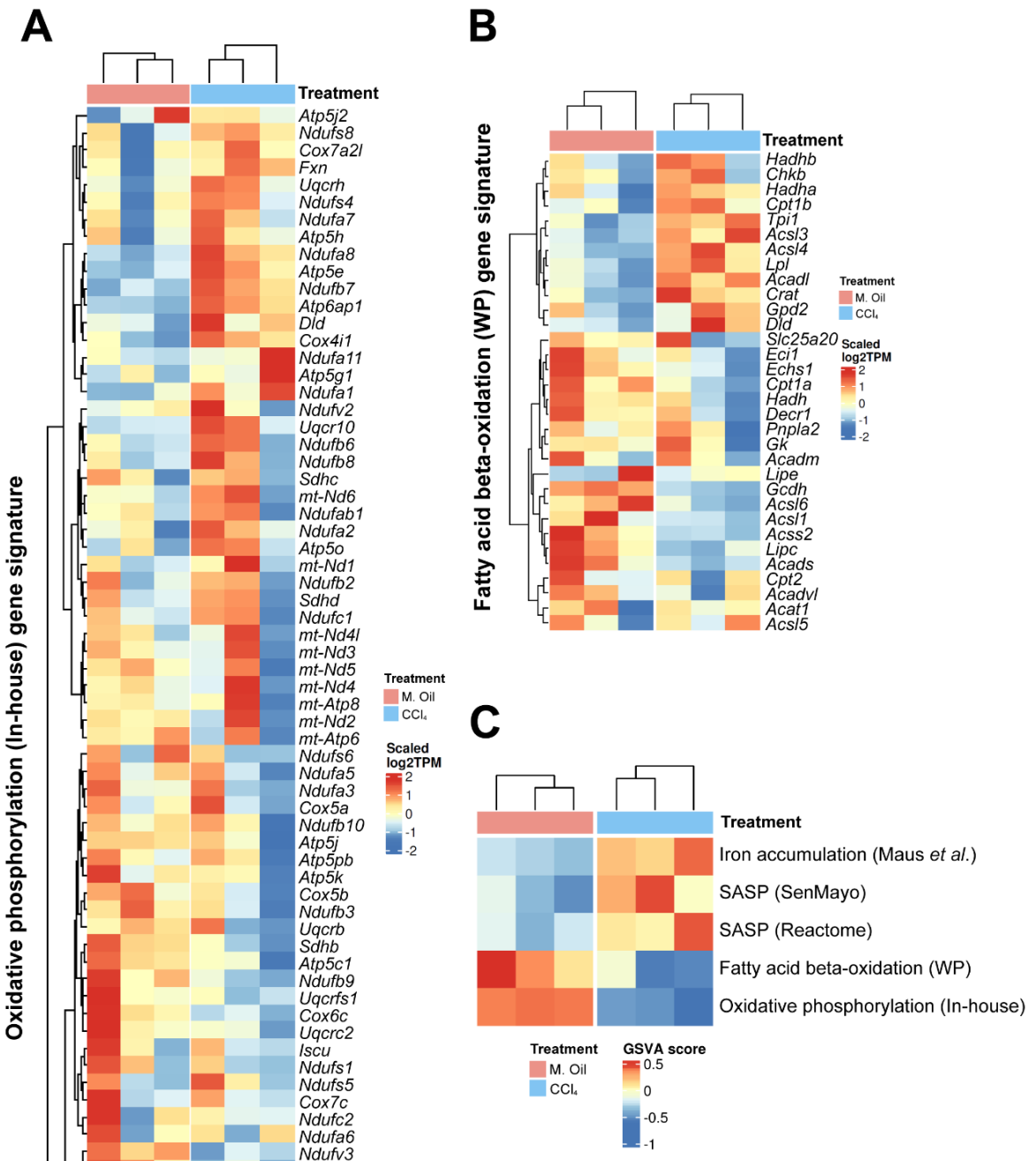

Figure 19. Analysis of oxidative metabolism-related gene transcriptomes in hepatocytes from untreated or CCl_4-treated mice. RNA-seq analysis in hepatocytes from mice treated with CCl_4 or mineral oil (M. Oil) for 4 weeks (n=3 mice/group). **A.** Heatmap showing changes in gene expression for an oxidative phosphorylation gene signature (In-house) generated by selecting genes that were in at least 2 out of the 3 oxidative phosphorylation signatures from MSigDB v2023.1 (Hallmark, WikiPathways: WP, and Gene Ontology Biological Process: GOBP collections). **B.** Heatmap showing changes in gene expression for a fatty acid beta-oxidation gene signature (WP). **C.** Heatmap showing changes in relative activation of gene expression signatures analyzed with GSVA.

Looking at previously published transcriptomic data from hepatocytes treated *in vitro* with CCl_4 [125], we could observe that iron accumulates after three days of treatment, concomitant with an increase in SASP, ROS and TGF-β gene transcriptomic pathways (**Figure 20A**). In another study that performed RNA-seq analysis in the whole liver cell population [127], we observed the same tendency with iron apparently accumulating during the progression of liver fibrosis, concomitant with an increase in SASP, TGF-β and fibrotic gene transcriptomic pathways, but all these pathways decreased at longer times, in the tolerance phase (**Figure 20B**). These data supported our findings about gene signatures upregulation in isolated mouse hepatocytes from the CCl_4 model. However, whether other hepatic cells different from hepatocytes can also accumulate iron and develop senescence in this model was still unresolved. Therefore, we looked for a published single-cell RNA-seq dataset from CCl_4-treated livers [124] and performed the same analyses in all cell populations. Interestingly, we observed that iron accumulates also in other non-parenchymal liver cell types, significantly correlating with senescence in HSC, endothelial cells and cholangiocytes (**Figure 21**).

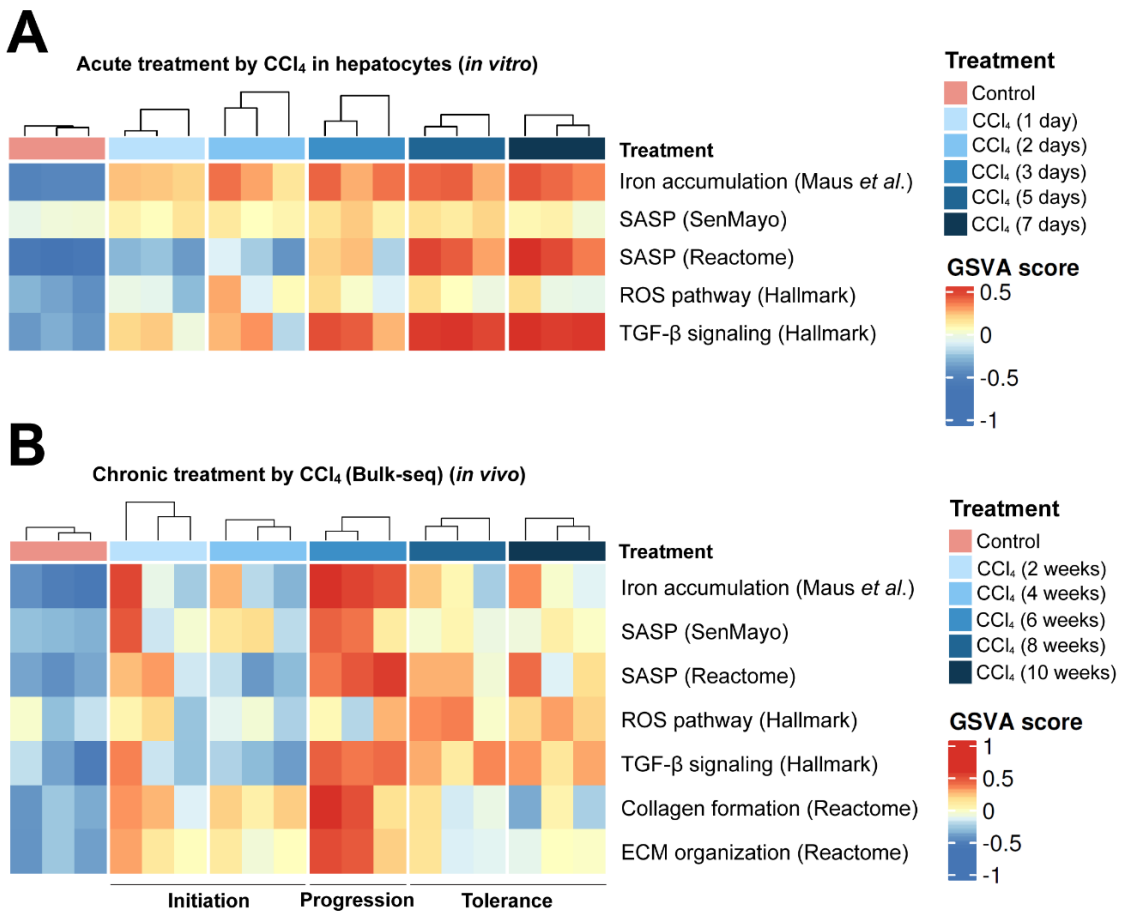

Figure 20. Analysis of iron accumulation, SASP expression and fibrotic hallmarks induced by CCl_4 in mouse (previously published data [125, 127]). A. Heatmap showing changes in relative activation of gene expression signatures analysed with GSVA in cultured mouse hepatocytes treated with CCl_4 [125]. **B.** Heatmap showing changes in relative activation of gene expression signatures analysed with GSVA in bulk RNA isolated from mouse livers under chronic treatment with CCl_4 at different phases of fibrosis progression [127].

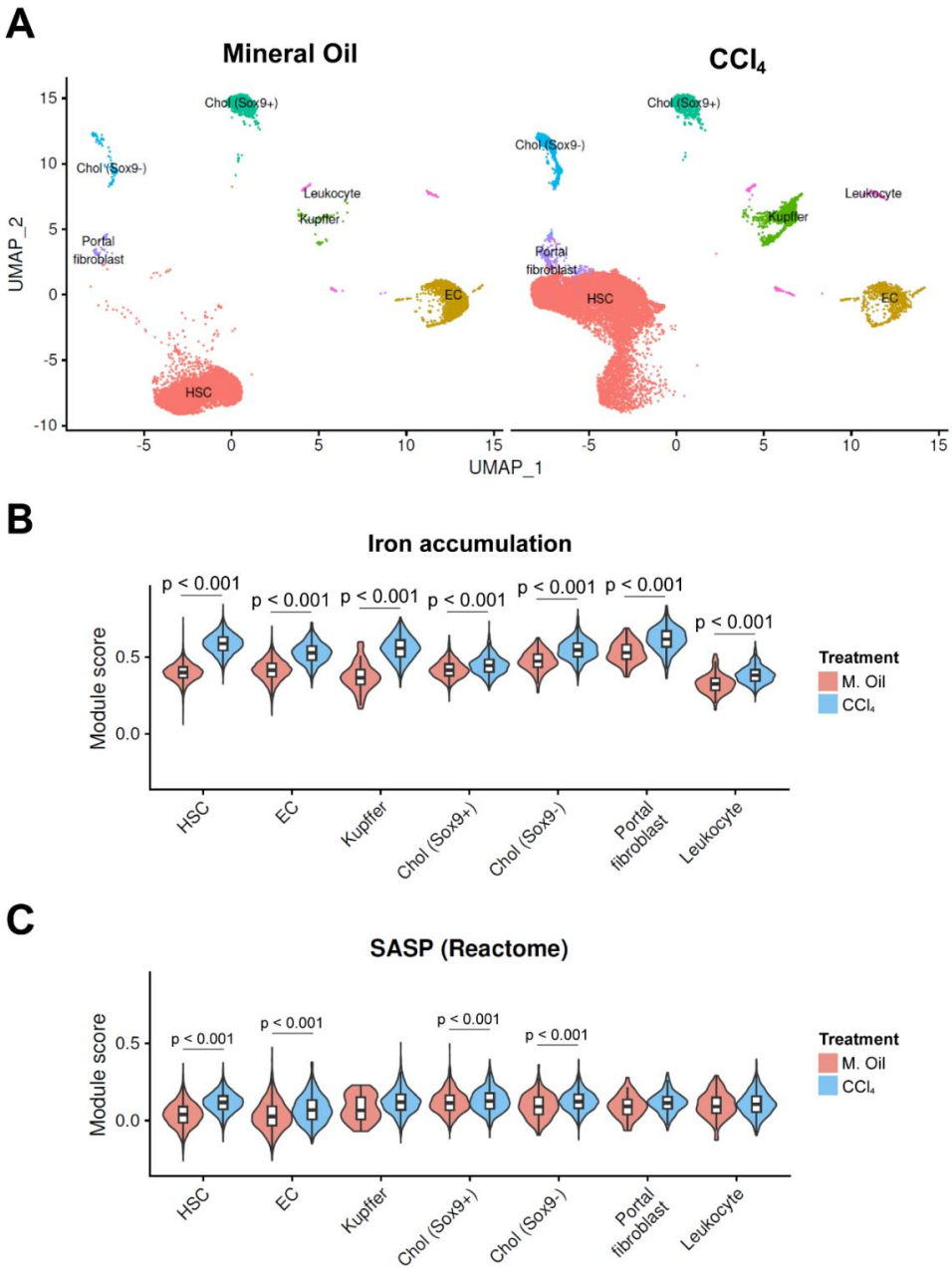

Figure 21. Single-cell transcriptomic analysis of non-parenchymal liver cells from CCl_4-treated mice (previously published data [124]). A. UMAP visualization of non-parenchymal cell types in each treatment condition (n=9.647 cells for Mineral Oil-treated and n=16.774 cells for CCl_4-treated mice). **B-C.** Relative quantification of iron accumulation (B) and SASP (Reactome) (C) gene expression signatures in single-cell RNA-seq data from mineral oil- and CCl_4-treated mice. Statistical analysis was done using Mann-Whitney U-test and adjusted for multiple comparisons. HSC: hepatic stellate cells; EC: Endothelial Cells; Chol: Cholangiocytes.

1.2. Effect of iron chelation by deferiprone on CCl_4-induced liver fibrosis in mice.

After demonstrating that iron accumulation occurs in the liver parenchyma of a model of liver fibrosis in mouse, concomitant with senescence development in hepatocytes, we decided to analyse the relevance of iron accumulation in the fibrosis progression, as well as its relevance in senescence. Hence, a new experiment was performed in mice that were injected with CCl_4 for 4 weeks to induce liver fibrosis and were treated with deferiprone, an iron chelator, from one week after the first CCl_4 injection, as described in Materials and Methods and schematized in **Figure 9B** Representative images of the livers are shown (**Figure 22A**). The variation in body weight along the experiment (**Figure 22B**) showed a better progression in the group of mice that were injected with CCl_4 and received deferiprone, compared with CCl_4 alone, suggesting a potential therapeutic effect. Immunohistochemical analysis revealed that the iron deposits found in the CCl_4-treated mice significantly decreased by the treatment with deferiprone (**Figure 22C**). Expression of the transferrin receptors 1 and 2 (*Tfr1/2*) and the homeostatic iron regulator (*Hfe*), which regulates the binding and endocytosis of the circulating Fe-transferrin into the cell, were found upregulated in livers from mice treated with deferiprone, indicating a potential response of the cells in a situation of decreased iron levels (**Figure 22D**). However, these changes were small, suggesting that deferiprone was not causing a systemic iron deficiency.

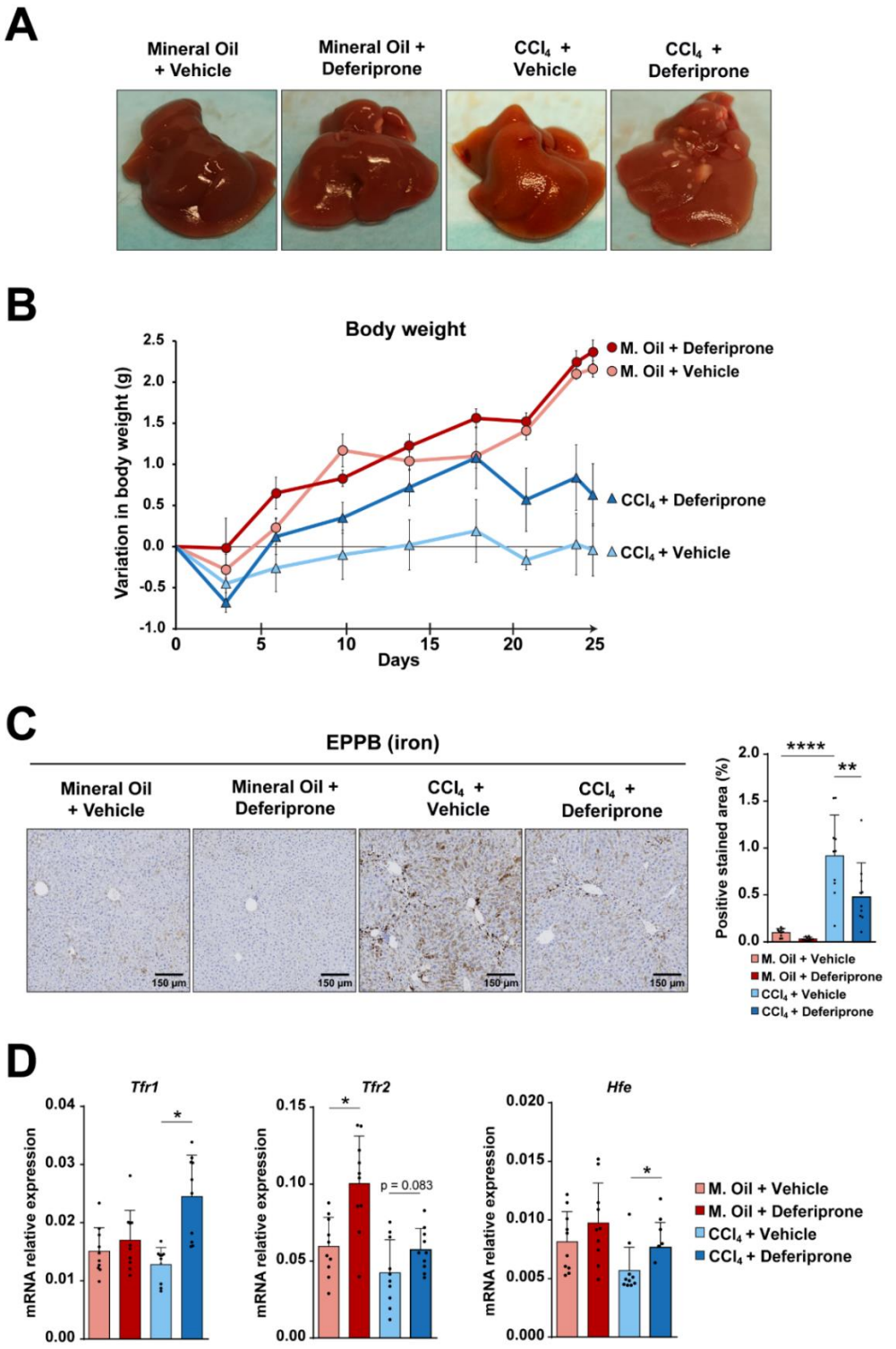

Figure 22. Effects of deferiprone on iron accumulation in the model of CCl_4-induced liver fibrosis. A. Representative images of the livers from each group at sacrifice. **B.** Variation in body weight along the experiment. **C.** Iron accumulation analysed by enhanced Perl's Prussian Blue (EPPB) staining in paraffin-embedded liver sections. Representative areas are shown for each group. Percentage of positive stained area was quantified for each animal using ImageJ software. Each dot represents the arithmetic mean of the percentage of positive stained area from three different regions for each animal. RT-qPCR analysis of a panel of genes related to iron metabolism. Data are presented as mean (SD) (n=10 mice/group). Statistical analysis was done with one-way ANOVA with Sidak's correction. *p<0.05; **p<0.01; ***p<0.001; ****p<0.0001.

Having confirmed that deferiprone was preventing iron accumulation upon CCl_4 treatment, we analysed the effects on fibrosis. The fibrotic collagen area, as stained by Picro-Sirius Red, was decreased in the mice treated with deferiprone compared to CCl_4 alone (**Figure 23A**). Analysis of α-SMA, as a myofibroblastic marker, showed similar results, with a significant decrease when analysed both by IHC and Western blot (**Figure 23B-C**). These results indicated that deferiprone attenuates liver fibrosis induced by CCl_4 in mice.

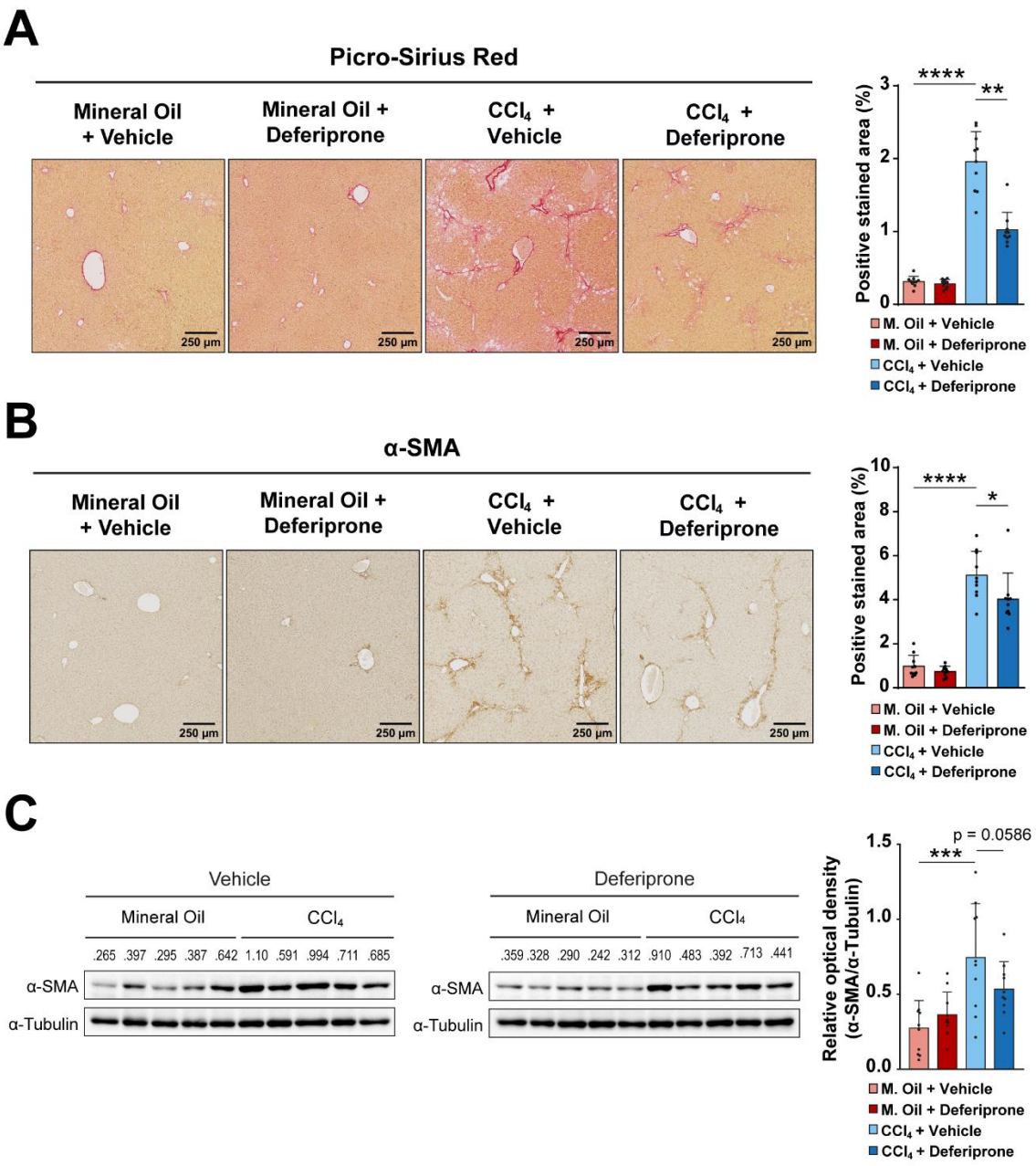

Figure 23. Effects of deferiprone on fibrosis hallmarks in the mouse CCl_4-induced liver fibrosis model. Fibrosis was analysed in paraffin-embedded tissue sections after 4 weeks of CCl_4 treatment: **A.** Picro-Sirius Red staining. **B.** α-SMA immunohistochemistry as a marker of myofibroblasts. **C.** Western blot analysis of α-SMA protein levels in liver tissue from mice. In A

and B, the percentage of positive stained area was quantified for each animal using ImageJ software. Each dot represents the arithmetic mean of the percentage of positive stained area from three different regions for each animal. In C, two representative gels are shown. Densitometric analysis was performed in all 10 mice/group using Image Lab™ software (Bio-Rad). Results are shown as mean (SD) (n=10 mice/group). Two-tailed Mann-Whitney U-test was used for statistical analysis. *p<0,05; **p<0.01; ***p<0.001; ****p<0.0001.

Then, we moved to analyse hallmarks of senescence. As seen in **Figure 24A**, the staining for β-Galactosidase activity showed presence of senescent cells around the fibrotic area in the CCl_4 group and, remarkably, deferiprone treatment significantly decreased the percentage of senescent area. Analysis of the SASP-related proteome, analysed as described in **Figure 18**, revealed that CCl_4 treatment induced the production of inflammatory cytokines such as MCP-1, 6CKINE or MDC. This cytokine regulation pattern was not found in animals treated with deferiprone (**Figure 24B**). Moreover, anti-fibrotic or anti-inflammatory cytokines, such as IFN-β1, IL-4, IL-9, IL-10, IL-13 or IL-20, were significantly increased in the CCl_4-treated mice that received deferiprone, compared to CCl_4 alone. IL-2, a cytokine that mediates the specific expansion of Tregs, which may ameliorate tissue damage following CCl_4 administration [139], also presented higher levels in the CCl_4+deferiprone group.

Altogether, these results suggest that oral treatment with deferiprone decreases iron accumulation, senescence and liver fibrosis hallmarks induced by CCl_4 in mice.

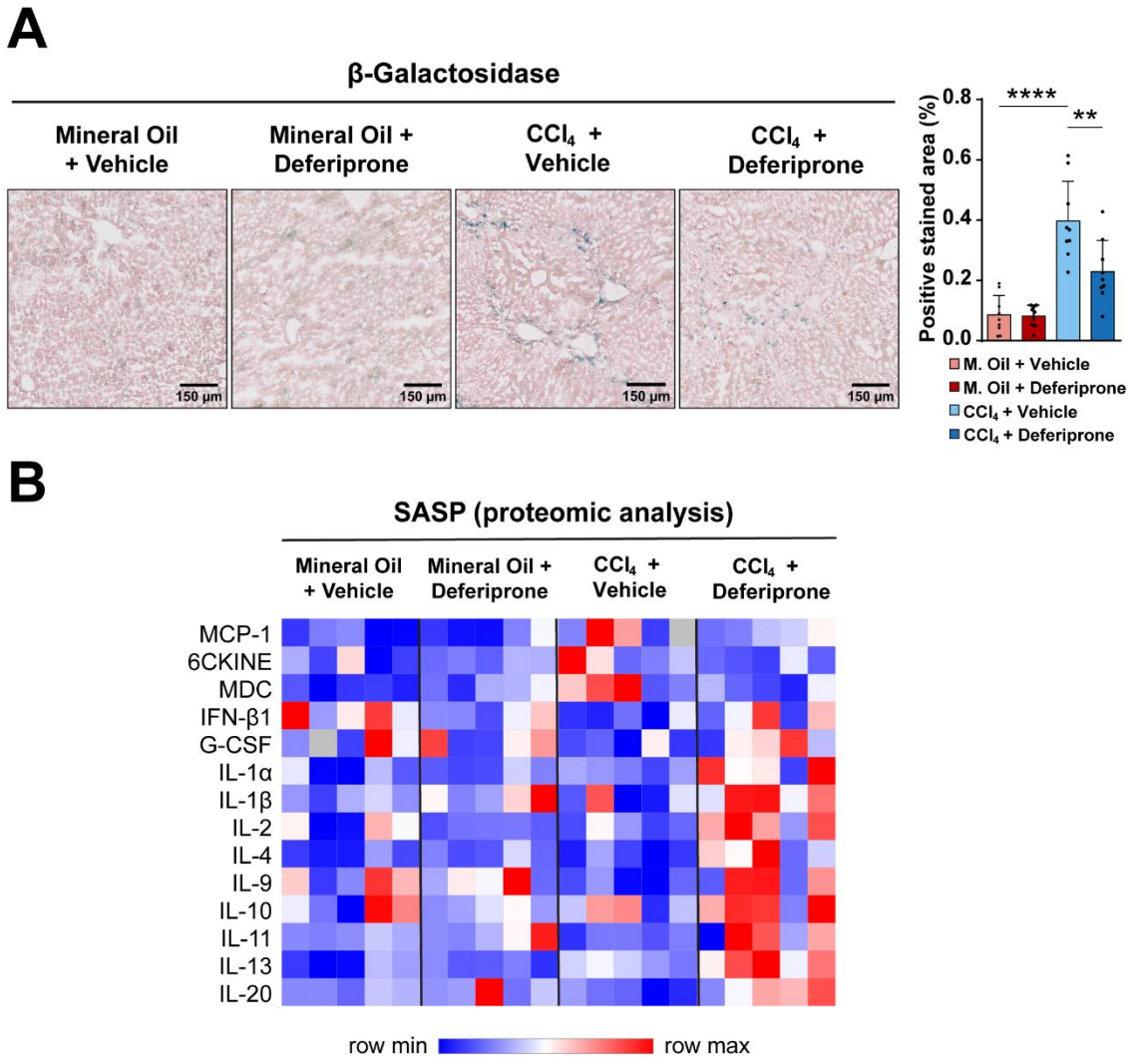

Figure 24. Effects of deferiprone on senescence hallmarks in the mouse CCl_4-induced liver fibrosis model. A. Fresh liver tissues embedded in OCT were cut in sections and stained for detection of β-Galactosidase activity. Images of representative areas are shown for each group. Percentage of positive stained area was quantified for each animal using ImageJ software. Each dot represents the arithmetic mean of the percentage of positive stained area from three different regions for each animal. Results are shown as mean (SD) (n=10 mice/group). Two-tailed Mann-Whitney U-test was used for statistical analysis. *p<0,05; **p<0.01; ***p<0.001; ****p<0.0001. **B.** A panel of 45 cytokines and chemokines characteristic of the SASP were analysed at the protein level in tissue samples, n=5 mice/group. Data were analysed carefully and those factors with statistically significant changes (one-way ANOVA with Sidak's post-hoc test, p-value < 0.05) are summarized in a heatmap format.

1.3. Analysis of the efficacy of deferiprone to attenuate iron accumulation and senescence in human hepatocytes and HSC in *in vitro experiments.*

After deciphering the effects of deferiprone in a mouse model of liver fibrosis, we wanted to explore whether hepatocytes are the major cell type responsible for

these therapeutic effects. To shed light on this matter, we used *in vitro* cell cultures, where we can work in a more controlled environment with less variables interplaying with the results. We wondered whether deferiprone could prevent senescence in a human hepatocyte cell line (HH4 cells) *in vitro*. To induce senescence, we decided to use doxorubicin, a DNA intercalating agent that inhibits the DNA topoisomerase II impairing DNA synthesis [140] and that is frequently used as a senescence inducer in research [141].

We treated HH4 cells with doxorubicin (50 nM), alone or in co-treatment with deferiprone (50 µM) for 6 days, as detailed in Materials and Methods section and schematized in **Figure 8A**. Correlating with previous results [62], doxorubicin increased the intracellular labile iron content, as revealed by the increase in fluorescence by the FerroOrange probe. Noteworthy, the levels of labile iron were attenuated by deferiprone, as seen in microscope images and quantification by flow cytometry (**Figure 25A-B**). Moreover, in the presence of deferiprone, a reduction in the expression of iron-induced genes, such as *HMOX1* or *HAMP* (hepcidin), was seen (**Figure 25C**).

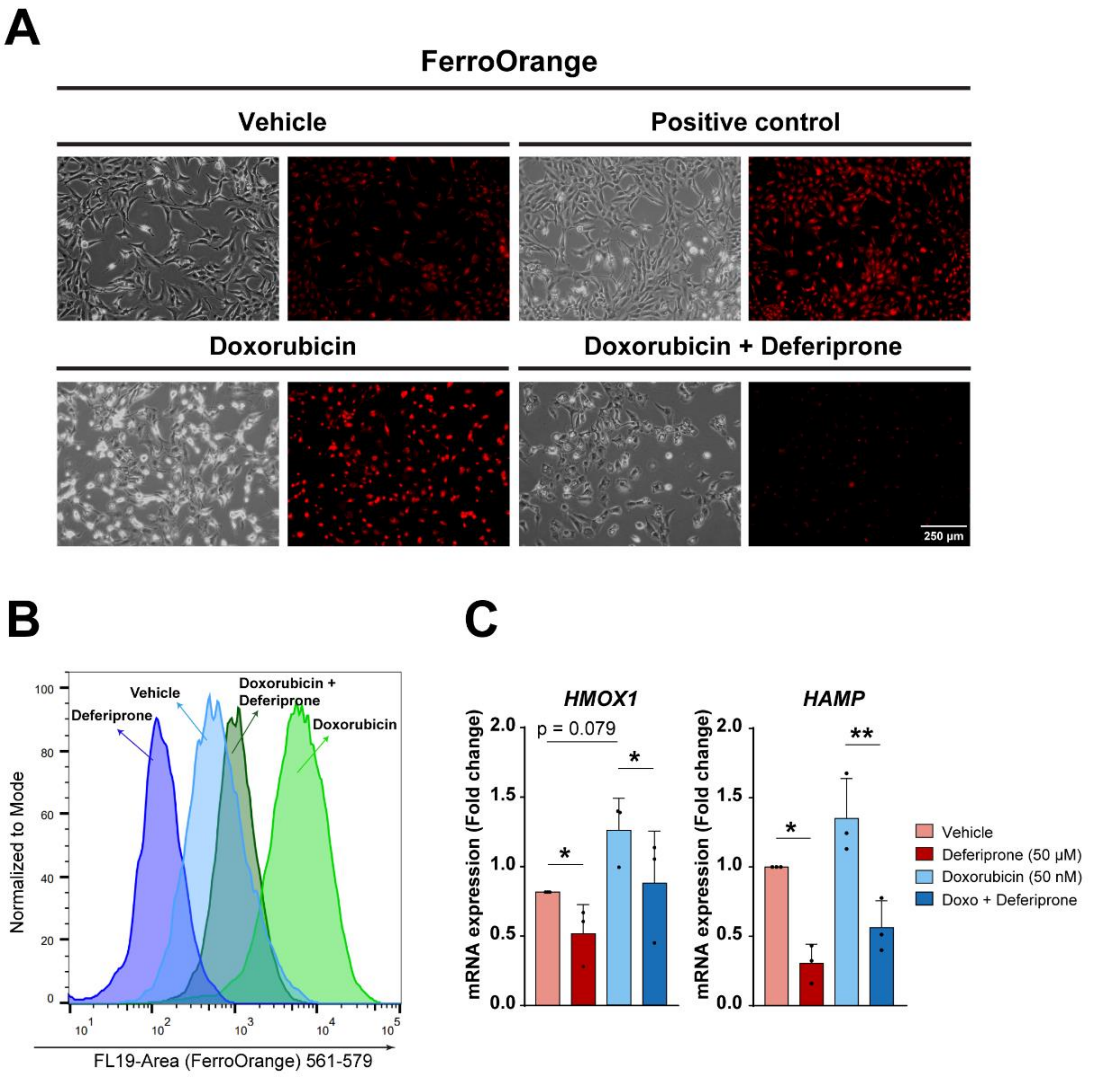

Figure 25. Effects of deferiprone on iron accumulation in human hepatocytes. The human hepatocyte cell line HH4 was cultured as described in **Figure 8A**. **A.** FerroOrange probe was used to analyse iron accumulation. Treatment for 24 h with iron (660 µM) was used as positive control. Representative images were taken with a fluorescence microscope (left). **B.** Quantification of fluorescence by flow cytometry. **C.** Gene expression of *HMOX1* and *HAMP* as relevant genes related to iron metabolism, analysed by RT-qPCR. All analyses were done after 6 days of the corresponding treatment. Statistical analysis was done with one-way ANOVA with Sidak's correction (n=3 independent experiments). In A and B, a representative experiment is shown. *p<0.05; **p<0.01.

We then confirmed the induction of senescence through *CDKN1A* (p21) gene expression and β-Galactosidase activity, both increased upon doxorubicin treatment (**Figure 26A-B**). The increase in β-Galactosidase activity observed in hepatocytes was markedly reduced by deferiprone (**Figure 26B),** which also slightly attenuated the up-regulation of CDKN1A (**Figure 26A**). The analysis of SASP-related gene expression revealed that doxorubicin induced the expression of *CX3CL1* (Fractalkine), *CCL22* (MDC), *IL6*, *CCL20* (MIP-3α) or *LIF* in hepatocytes, which was

clearly attenuated with the simultaneous presence of deferiprone (**Figure 26C**). Furthermore, deferiprone significantly attenuated the decrease in cell viability (**Figure 27A**) and apoptosis produced by doxorubicin in hepatocytes (**Figure 27B**).

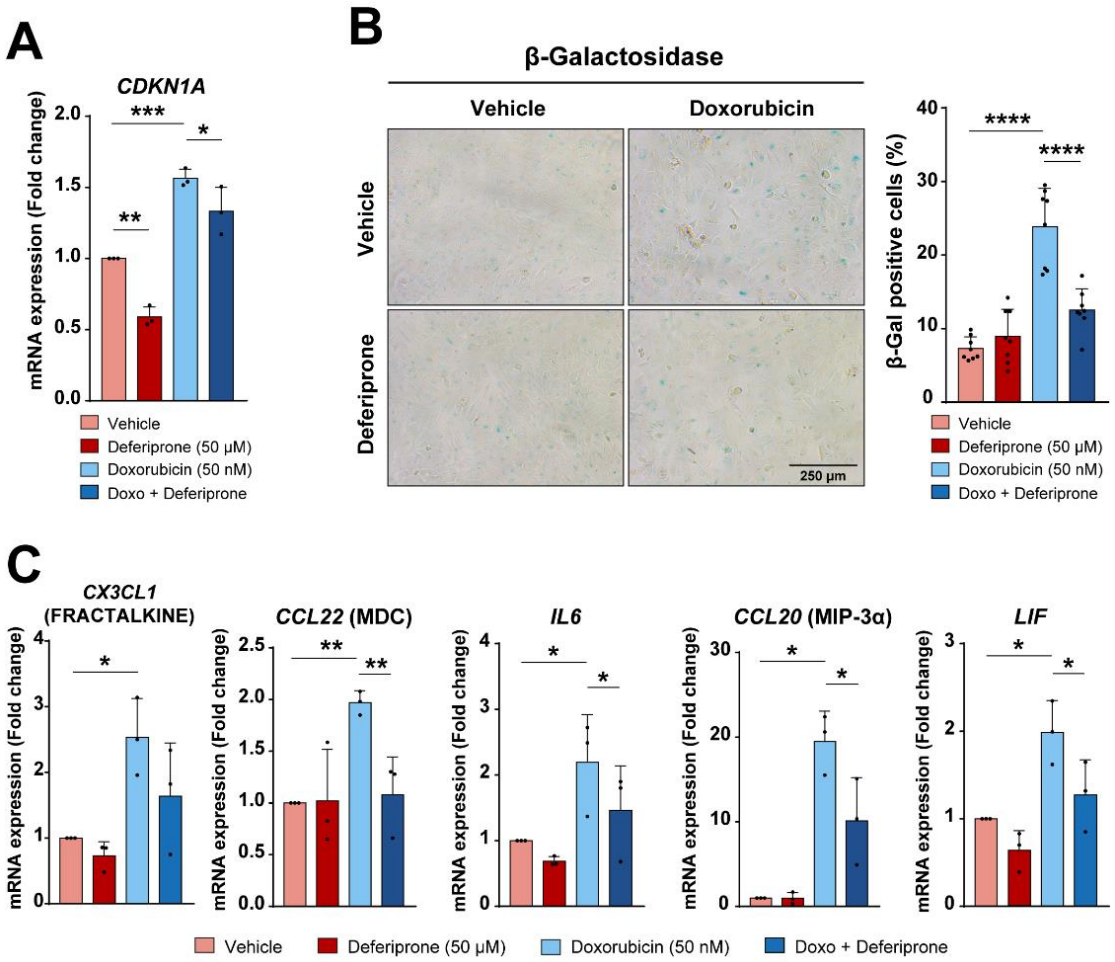

Figure 26. Effects of deferiprone on senescence in human hepatocytes. **A.** Gene expression of *CDKN1A* gene as marker of senescence, analysed by RT-qPCR. **B.** β-Galactosidase staining assay analysing senescence. At least 10 images were taken from random fields by phase contrast microscopy (left) and percentage of positive cells was quantified (right). **C.** RT-qPCR of a panel of SASP-related genes (*CX3CL1*, *CCL22*, *IL6*, *CCL20* and *LIF*. All analyses were done after 6 days of the corresponding treatment. Statistical analysis was done with one-way ANOVA with Sidak's correction (A) or two-tailed Mann-Whitney U-test (B, C) (n=3 independent experiments). In B, a representative experiment is shown. *p<0.05; **p<0.01; ***p<0.001; ****p<0.0001.

We next wondered if ferroptosis, a new form of iron-induced cell death discovered in recent years, could be relevant in our models. Ferroptosis is described as a modality of programmed cell death driven by iron-dependent lipid peroxidation that plays a relevant role in many pathological states, such as tumours, neurological diseases, acute kidney injury, ischemia/reperfusion, etc. [142, 143]. With this purpose, we used a probe that becomes fluorescent in conditions of lipid peroxidation associated with ferroptosis (BODIPY C11). As seen in **Figure 28A**, there was no increase in fluorescence (ferroptosis) in our model of senescent hepatocytes either in dead or alive cells. In addition, a transcriptomic analysis in our *in vivo* CCl_4 model-derived hepatocytes did not support the induction of ferroptosis (**Figure 28B**). Indeed, we propose that iron accumulation during chronic liver damage induces senescence and SASP in hepatocytes, which would contribute to liver inflammation and fibrosis.

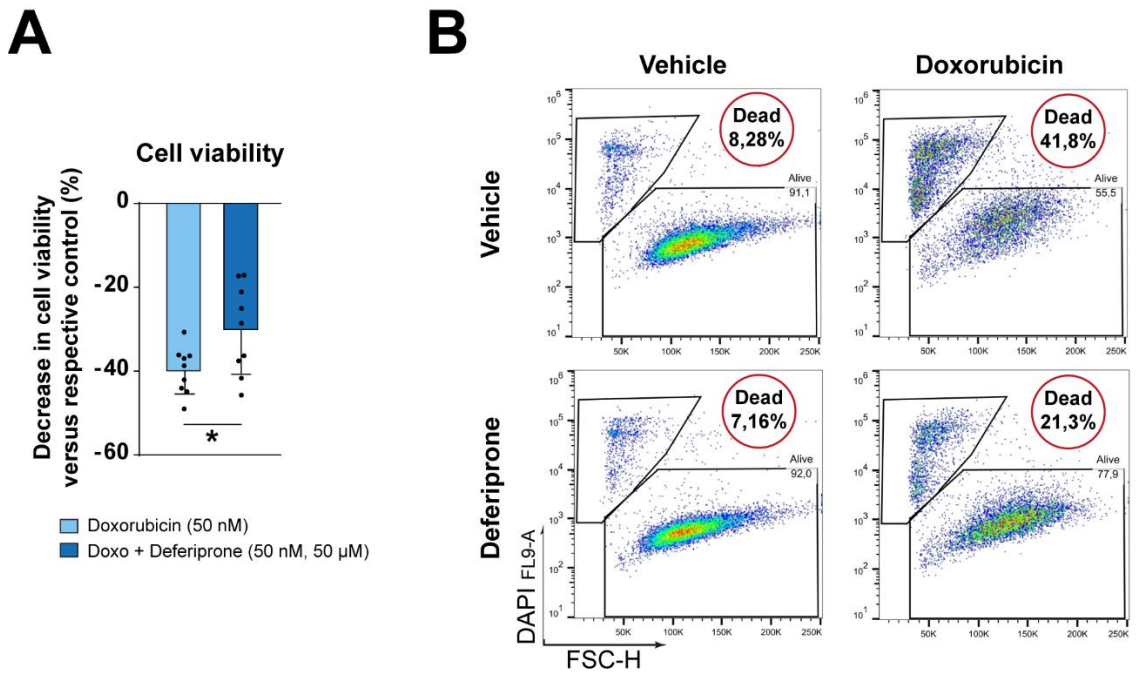

Figure 27. Effects of deferiprone on cell viability in human hepatocytes. **A.** Cell viability was assessed by crystal violet and expressed as loss of viability *versus* the respective control (vehicle or deferiprone). **B.** Flow cytometry with DAPI staining was used to determine the percentage of dead cells. All analyses were done after 6 days of the corresponding treatment. Statistical analysis was done with two-tailed Mann-Whitney U-test (A) (n=3 independent experiments in triplicate). In B, a representative experiment is shown. *p<0.05.

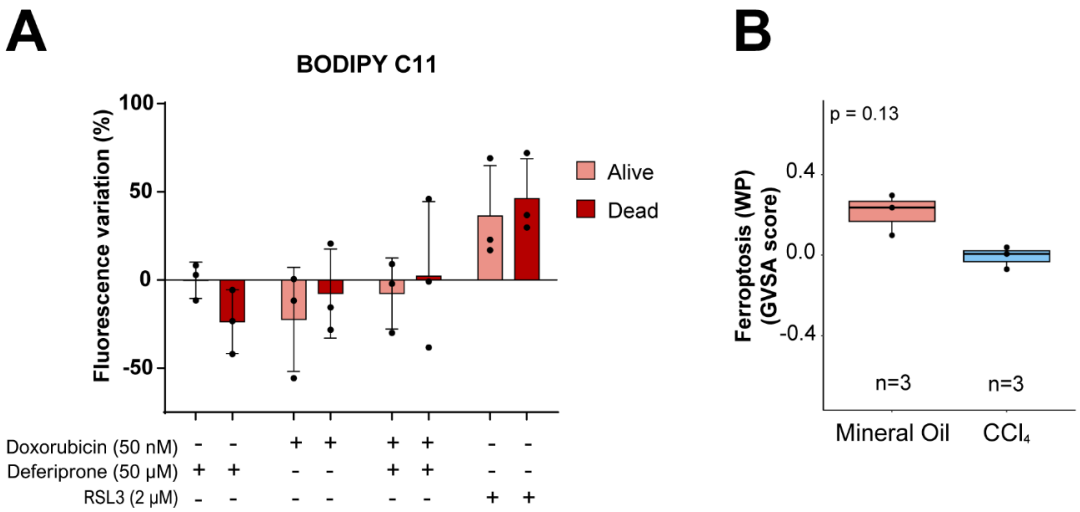

Figure 28. Analysis of ferroptosis in human hepatocytes (*in vitro*) and murine hepatocytes isolated from the *in vivo* CCl_4 model. A. HH4 hepatocyte cell line was cultured as detailed in **Figure 8A** and then incubated 40 min with BODIPY C11 (5 µM) probe as an indicator of lipid peroxidation linked to ferroptosis. Attached (alive) and floating (dead) cells were then collected, stained with DAPI to analyze cell viability, and run in a GalliosTM Cytometer. RSL3 (2 µM) treatment overnight was used as positive control. Three independent experiments were done. Results are shown as mean (SD) expressed as percentage of fluorescence variation versus control cells (untreated). **B.** Boxplot of relative enrichment for the ferroptosis gene signature in hepatocytes isolated from mice treated with CCl_4 or mineral oil for 4 weeks, analyzed by RNA-seq (n=3 mice/group). Statistical analysis was done with two-tailed Mann-Whitney U-test.

As we have described before, not only hepatocytes, but also other cell types in the liver accumulate iron and become senescent in profibrotic conditions. Therefore, we checked whether iron chelators could also modulate senescence and/or profibrotic activity (in response to TGF-β) in HSC, the major players in liver fibrosis, by using the LX-2 cell line, as schematized in **Figure 8B**. After 6 days of treatment, an increase in iron accumulation by doxorubicin was also observed and was attenuated by deferiprone (**Figure 29A-B**). Furthermore, deferiprone induced an upregulation of *TFR1* gene expression (**Figure 29C**), suggesting a situation of decreased iron availability. However, the increase in the percentage of β-Gal-positive cells produced by doxorubicin was not altered by the presence of deferiprone (**Figure 30A**), correlating with no effects on *CDKN1A* upregulation (**Figure 30B**). The analysis of SASP-related gene expression revealed that doxorubicin induced the expression of *IL1A*, *IL1B*, *CCL20* (MIP-3α) or *LIF* (which also showed up-regulation by TGF-β). However, deferiprone was not able to attenuate the doxorubicin-induced SASP-related gene expression in HSC (**Figure 30C**). A fundamental biological process in HSC during fibrosis is the transdifferentiation towards myofibroblasts. We have previously mentioned that senescence of HSC limits their fibrotic phenotype

[53]. In accordance with this, senescence induced by doxorubicin attenuated the TGF-β-mediated activation of LX-2 HSC, as evidenced by the decreased expression of *COL1A1* or *FN1*, and, interestingly, this attenuation was not affected by the presence of deferiprone (**Figure 30D**).

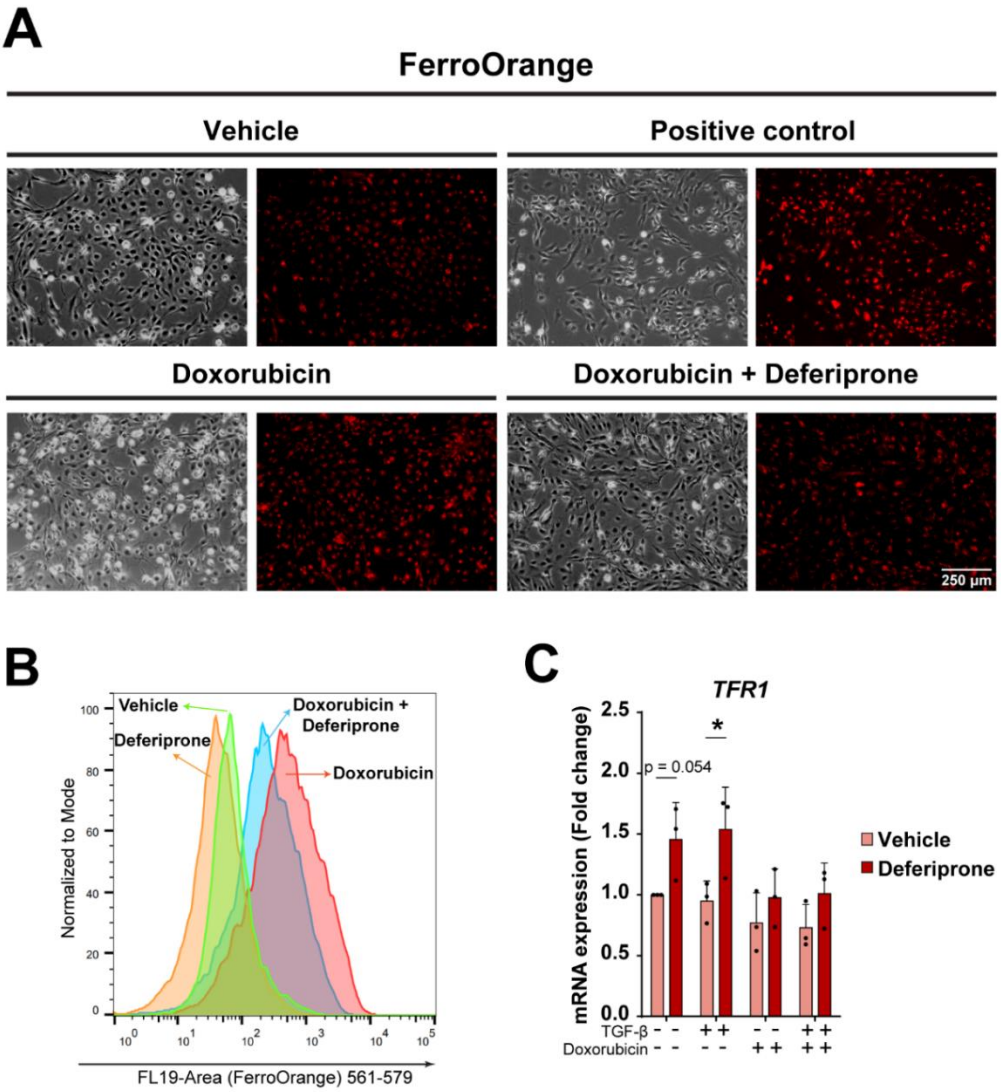

Figure 29. Effects of deferiprone on iron accumulation in a human HSC senescence model induced by doxorubicin. The human HSC cell line LX-2 was cultured as detailed in **Figure 8B** with doxorubicin as a senescent inducer. **A.** FerroOrange dye was used to analyse iron accumulation. Treatment for 24 h with iron (660 µM) was used as positive control. Representative images were taken with a fluorescence microscope. **B.** Quantification of fluorescence signal was performed by flow cytometry. **C.** *TFR1* mRNA levels were analysed by RT-qPCR. C. β-Galactosidase staining assay was performed to analyse senescence. Six images were taken from random fields by phase contrast microscopy (left) and percentage of positive cells were quantified (right). D-F. Analysis of mRNA levels by RT-qPCR of CDKN1A, a panel of SASP related genes (IL1A, IL1B, CCL20 and LIF) and HSC activation related genes (COL1A1, FN1). All analyses were done after 6 days of the corresponding treatment. Statistical analysis was done with one-way ANOVA with Sidak's correction (n=3 independent experiments). In A and B, a representative experiment is shown *p<0.05.

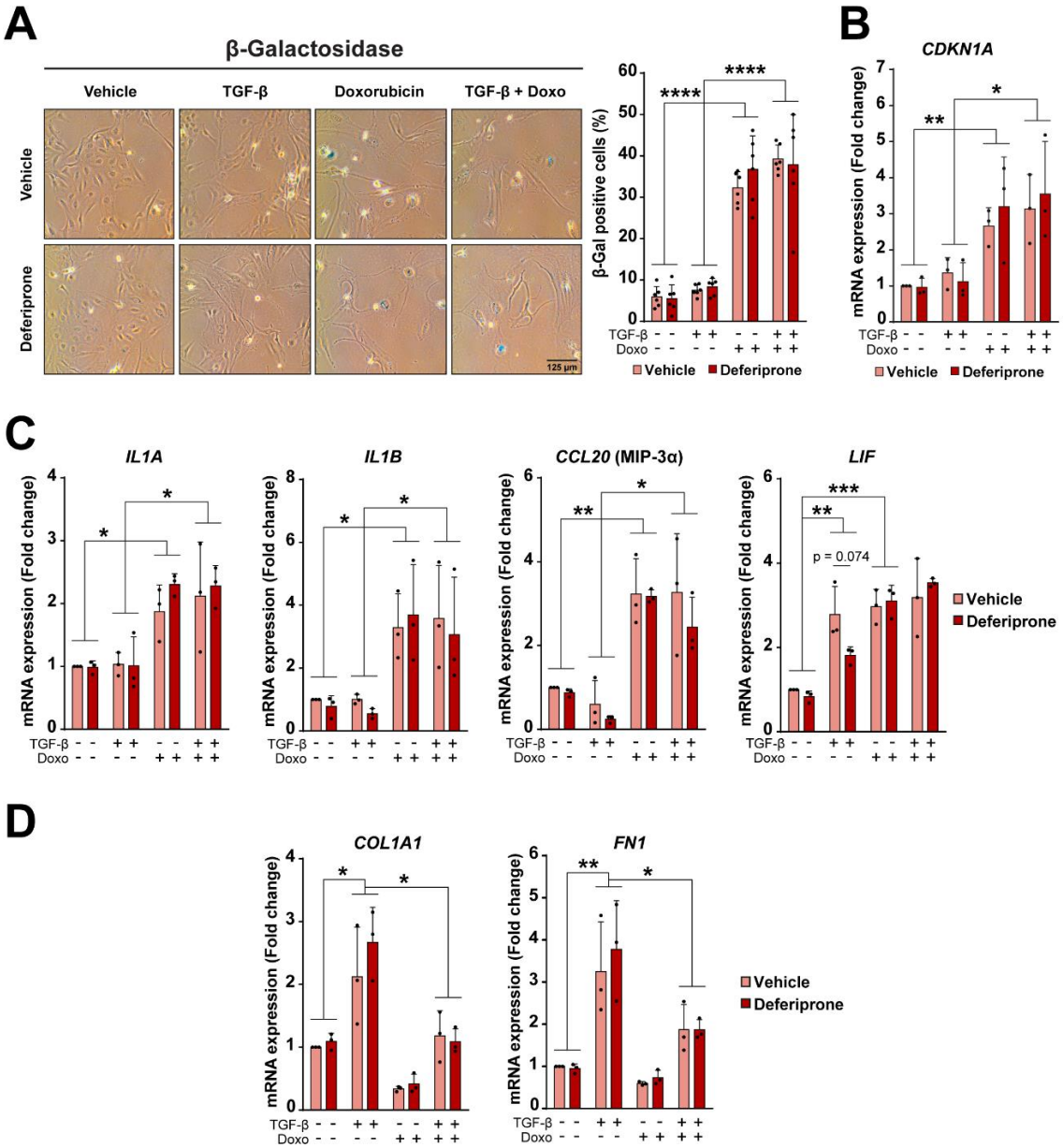

Figure 30. Effects of deferiprone on senescence and activation markers in a human HSC senescence model induced by doxorubicin. The human HSC cell line LX-2 was cultured as detailed in **Figure 8B** with doxorubicin as a senescent inducer. **A.** β-Galactosidase staining assay was performed to analyse senescence. Six images were taken from random fields by phase contrast microscopy (left) and percentage of positive cells were quantified. **B-D.** Analysis of mRNA levels by RT-qPCR of *CDKN1A*, a panel of SASP related genes (*IL1A*, *IL1B*, *CCL20* and *LIF*) and HSC activation related genes (*COL1A1*, *FN1*). All analyses were done after 6 days of the corresponding treatment. Statistical analysis was done with one-way ANOVA with Sidak's correction (n=3 independent experiments). In A, a representative experiment is shown *p<0.05; **p<0.01; ***p<0.001; ****p<0.0001.

Since doxorubicin-induced senescent hallmarks were not attenuated by deferiprone in HSC, contrary to what we observed in hepatocytes, we wanted to corroborate these results using an alternative pro-senescent factor in HSC. We used

deoxycholic acid (DCA), a bile acid produced by intestinal bacteria that is often found in the entero-hepatic circulation, and that it was previously described in the literature as inducer of senescence in HSC [144]. Results with DCA were like those obtained with doxorubicin, indicating that iron chelation with deferiprone does not attenuate senescence in HSC, regardless of the inducing agent (**Figures 31 and 32**).

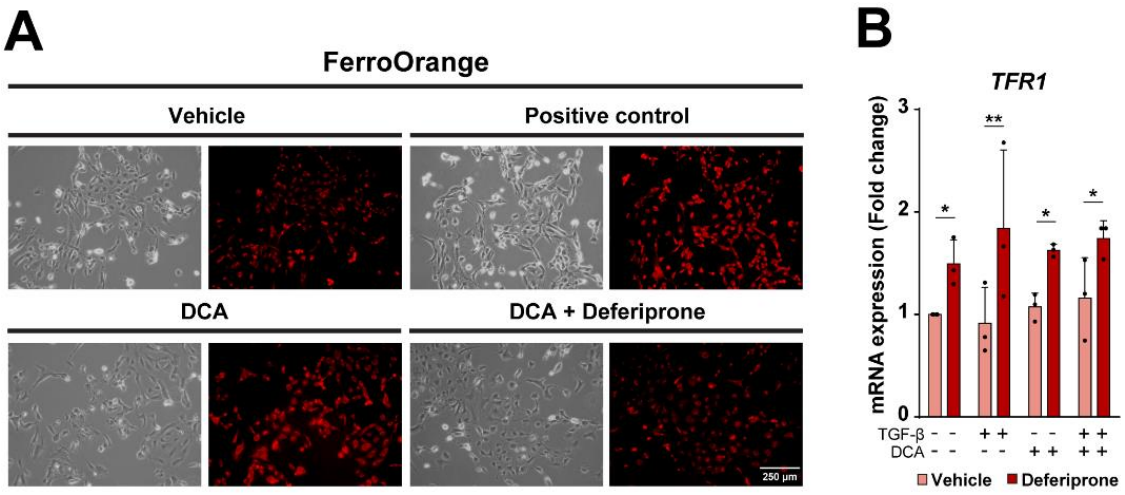

Figure 31. Effects of deferiprone on iron accumulation in a human HSC senescence model induced by DCA. The human HSC cell line LX-2 was cultured as detailed in **Figure 8B** with DCA as a senescent inducer. **A.** FerroOrange dye was used to analyse iron accumulation. Treatment for 24 h with iron (660 µM) was used as positive control. Images were taken with a fluorescence microscope and representative ones are shown. **B.** *TFR1* mRNA levels were analysed by RT-qPCR. All analyses were done after 6 days of the corresponding treatment. Statistical analysis was done with one-way ANOVA with Sidak's correction (n=3 independent experiments). In A, a representative experiment is shown *p<0.05; **p<0.01.

To exclude the possibility that a higher deferiprone dose might be necessary to see any effect in the LX-2 HSC cell line, we performed some experiments with a higher concentration of deferiprone (50 µM), obtaining the same results (data not shown).

Altogether, these results indicate that deferiprone counteracts senescence specifically in hepatocytes and has no effects on senescent HSC.

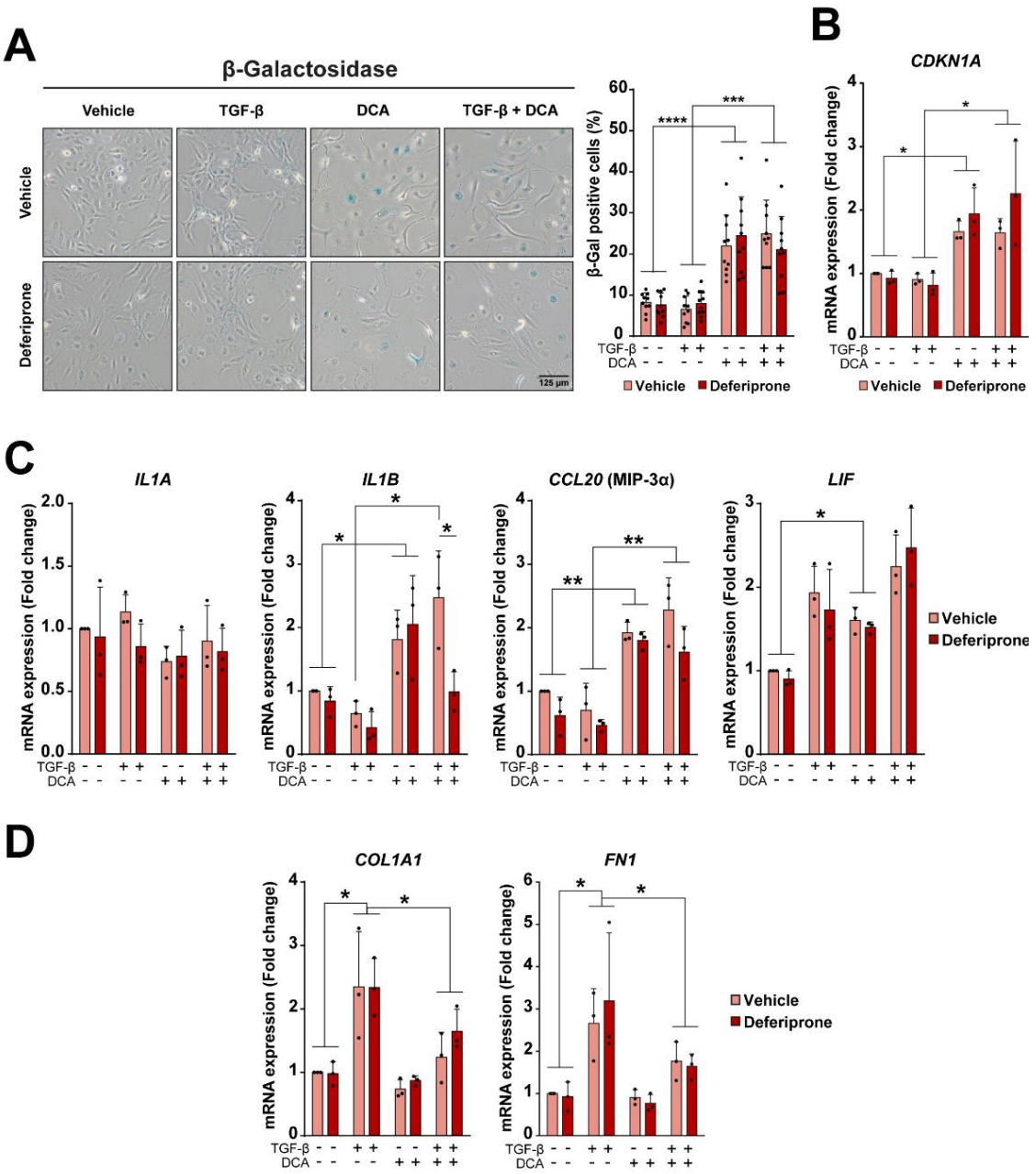

Figure 32. Effects of deferiprone on senescence and activation markers in a human HSC senescence model induced by DCA. The human HSC cell line LX-2 was cultured as detailed in **Figure 8B** with DCA as a senescent inducer. **A.** β-Galactosidase staining assay was performed to analyse senescence. Ten images were taken from random fields by phase contrast microscopy (left) and percentage of positive cells were quantified (right). **B-D.** Analysis of mRNA levels by RT-qPCR of *CDKN1A*, a panel of SASP related genes (*IL1A*, *IL1B*, *CCL20* and *LIF*) and HSC activation related genes (*COL1A1*, *FN1*). All analyses were done after 6 days of the corresponding treatment. Statistical analysis was done with one-way ANOVA with Sidak's correction (n=3 independent experiments). In A, a representative experiment is shown *p<0.05; **p<0.01; ***p<0.001; ****p<0.0001.

1.4. Translational relevance of iron accumulation and senescence in the development of liver fibrosis in patients.

After unveiling iron accumulation and senescence as relevant factors in our mouse CCl_4 model and *in vitro* hepatocytes, we next wondered if these could be relevant factors in fibrotic patients too. Hence, we analysed public data from a cohort of non-alcoholic fatty liver disease (now named MASLD) patients [128]. A preliminary overview of several iron accumulation, SASP and fibrosis-related gene signatures showed that apparently all gene signatures tested tended to increase along the stages of liver fibrosis (**Figure 33A**). When analysed thoroughly, we found a tendency to increase in the iron accumulation gene signature (**Figure 33B**) and a significant increase in the SASP-related SenMayo gene expression signature (**Figure 33C**) along fibrosis stages. Importantly, a strong correlation between iron accumulation and SASP SenMayo gene signatures was observed (**Figure 33D**).

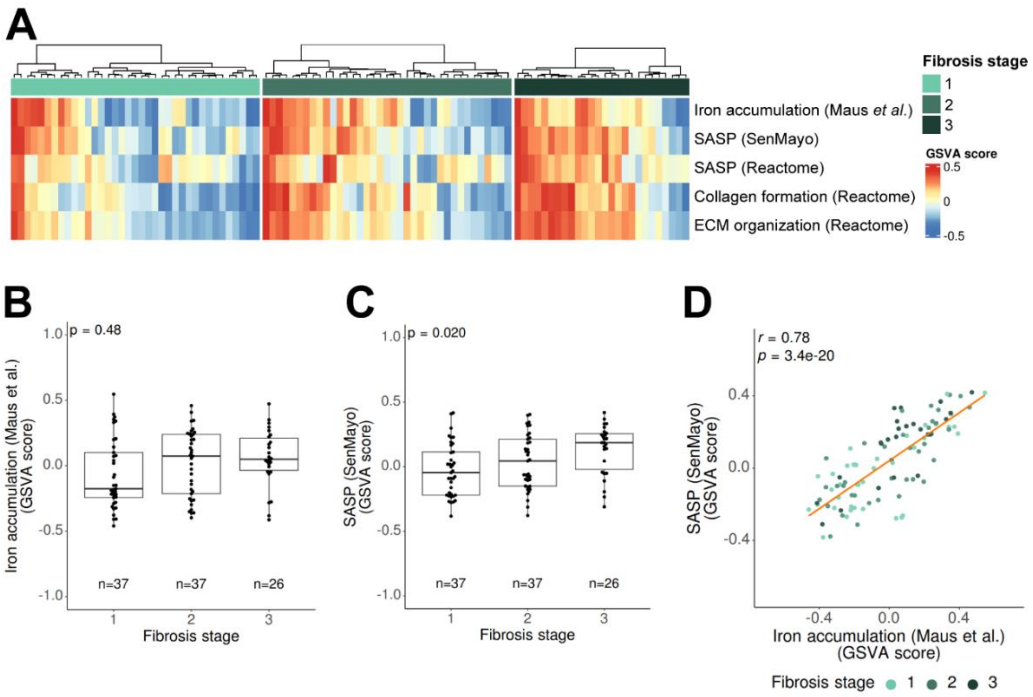

Figure 33. Analysis of iron accumulation and SASP expression across liver fibrosis stages in human MASLD patients. Transcriptomic data was obtained from the Fujiwara *et al.* cohort of liver fibrosis patients (34). **A.** Heatmap showing changes in gene expression for the following gene signatures: iron accumulation (designed by Maus et al., 18), SASP (SenMayo and Reactome), collagen formation (Reactome) and ECM organization (Reactome) classified by fibrosis stage. **B.** Boxplot of relative enrichment (GSVA score) for iron accumulation gene signature across fibrosis stages. **C.** Boxplot of SASP (SenMayo) gene signature relative enrichment (GSVA score) across fibrosis stages. **D.** Pearson correlation analysis of the relative enrichment of iron accumulation gene signature with SASP (SenMayo) gene signature. Each dot is a sample (color indicates the fibrosis stage). Kendall's τ was used to assess the association between the gene signatures and fibrosis stage. All analyses were adjusted for multiple testing with Bonferroni test correction.

Similarly to what we had done with the *in vitro* hepatocytes and mouse CCl_4 model, we analysed the ferroptosis-related gene signature along the fibrosis stages in patients and found no significant increase (**Figure 34A**), while correlations between ferroptosis and SASP gene signatures were weak and observed with only one of the SASP gene signatures (SenMayo) (**Figure 34B**).

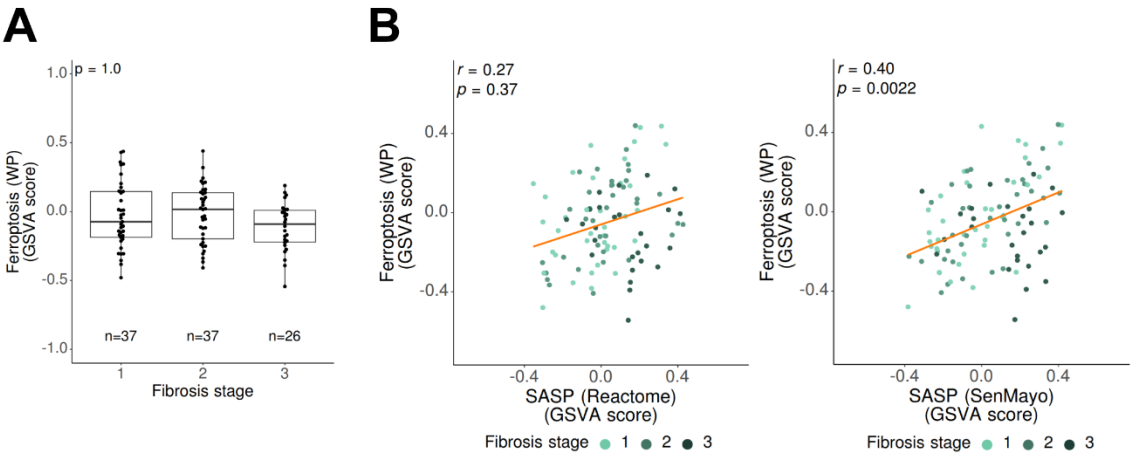

Figure 34. Transcriptomic analysis of ferroptosis in the human cohort of MASLD patients analysed in Figure 33. A. Boxplot of relative enrichment (GSVA score) for the ferroptosis (WikiPathways: WP) gene signature across fibrosis stages. **B.** Pearson correlation analyses between the relative enrichment of both SASP signatures (Reactome and SenMayo) and the ferroptosis signature. Each dot is a sample (colour indicates the fibrosis stage). Kendall's τ was used to assess the association between the gene signatures and fibrosis stage. P-values were adjusted using Bonferroni test correction.

Both iron accumulation and the SenMayo SASP gene signatures correlated with fibrotic hallmarks such as ROS-related genes, activation of the TGF-β pathway, collagen formation and ECM organization gene signatures (**Figure 35**). To further validate these findings, we performed the same analysis with the second SASP gene signature (Reactome), obtaining identical results (**Figure 36**). These analyses support the clinical relevance of iron accumulation in human liver fibrotic pathologies, establishing a strong correlation with pathological senescence and hallmarks of liver damage, inflammation and fibrosis.

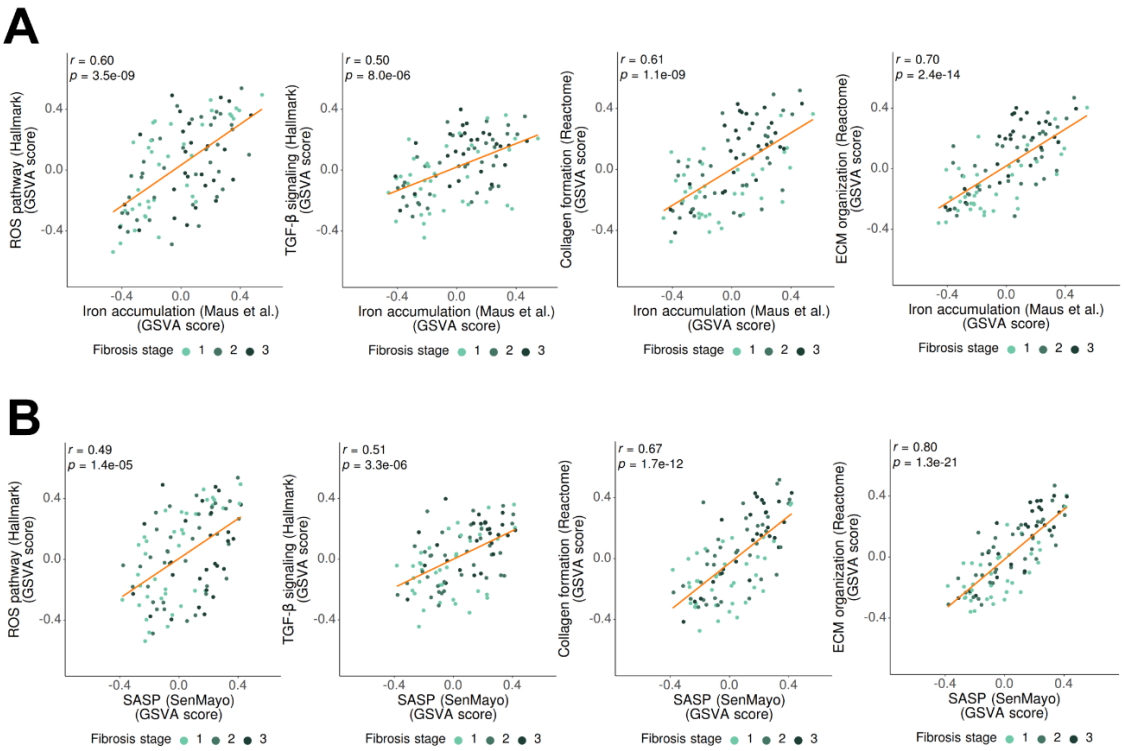

Figure 35. Analysis of the correlation between iron accumulation or SASP expression and fibrotic hallmarks across liver fibrosis stages in human MASLD patients. Transcriptomic data was obtained from the Fujiwara *et al.* cohort of liver fibrosis patients [128]. **A. and B.** Pearson correlation analyses of the relative enrichment in the gene signatures related to iron accumulation (A) and relative enrichment of SASP (SenMayo) (B) with ROS pathway (Hallmark), TGF-β signalling (Hallmark), collagen formation (Reactome) and ECM organization (Reactome) gene signatures in the Fujiwara *et al.* cohort of liver fibrosis patients [128]. Each dot is a sample (colour indicates the fibrosis stage). Kendall's τ was used to assess the association between the gene signatures and fibrosis stage. All analyses were adjusted for multiple testing with Bonferroni test correction.

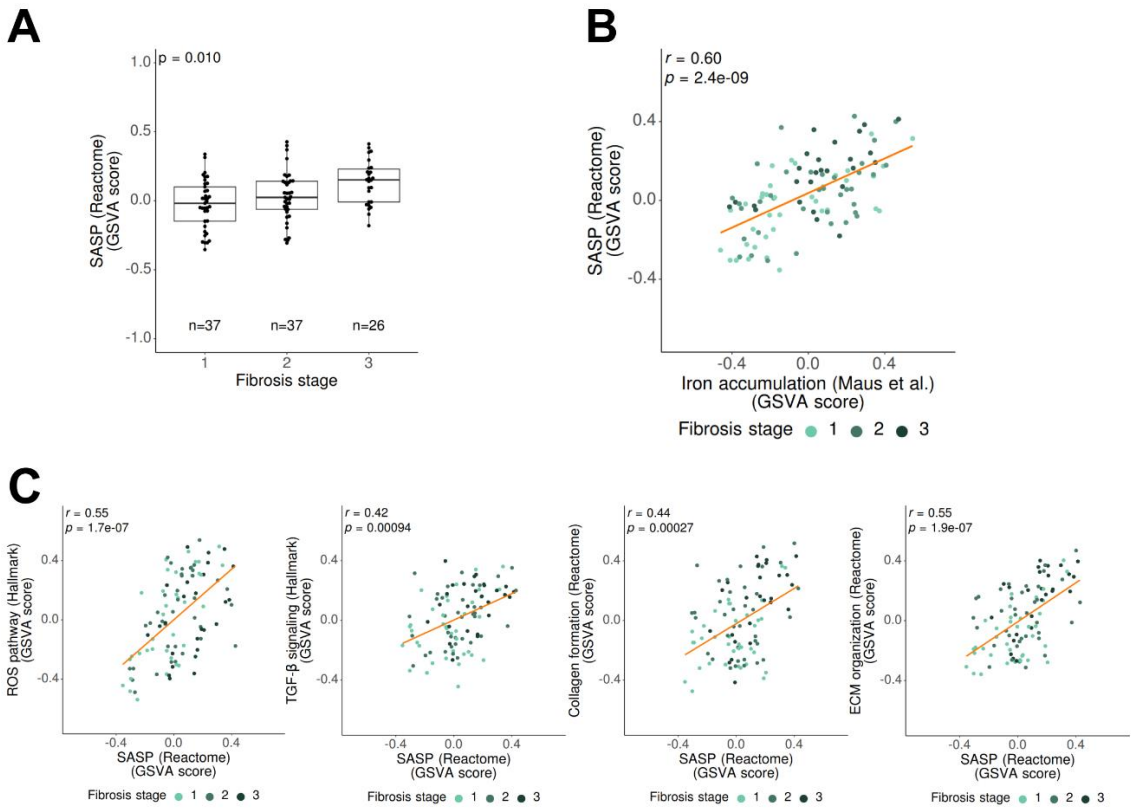

Figure 36. Analysis of iron accumulation and SASP expression along liver fibrosis stages in MASLD patients. Transcriptomic data was obtained from the Fujiwara *et al.* cohort of liver fibrosis patients [128]. **A.** Boxplot of SASP (Reactome) gene signature relative enrichment (GSVA score) across fibrosis stages. **B.** Pearson correlation analysis of the relative enrichment of iron accumulation gene signature with SASP (Reactome) gene signature. **C.** Pearson correlation analyses of the relative enrichment of SASP (Reactome) gene signature with ROS pathway (Hallmark), TGF-β signalling (Hallmark), collagen formation (Reactome) and ECM organization (Reactome) gene signatures. Each dot is a sample (colour indicates the fibrosis stage). Kendall's τ was used to assess the association between the gene signatures and fibrosis stage. All analyses were adjusted for multiple testing with Bonferroni test correction.

To have a more complete overview of the situation in other chronic liver disease aetiologies, we also explored public transcriptomic data from another cohort of patients suffering ASH and alcoholic cirrhosis [129]. Although some heterogeneity among the patients was observed (**Figure 37A**), a clear positive correlation was patent between iron accumulation and SASP (**Figure 37B**). Then, we looked for the specific correlation between iron accumulation or SASP with collagen formation and ECM organization pathways. In this case we observed a significant and stronger correlation with the SASP than with iron accumulation, although the latter was significant too in the case of cirrhotic patients (**Figure 38**).

These analyses support the clinical relevance of iron accumulation in human liver fibrotic pathologies from different aetiologies, establishing a strong correlation with pathological senescence and hallmarks of liver fibrosis.

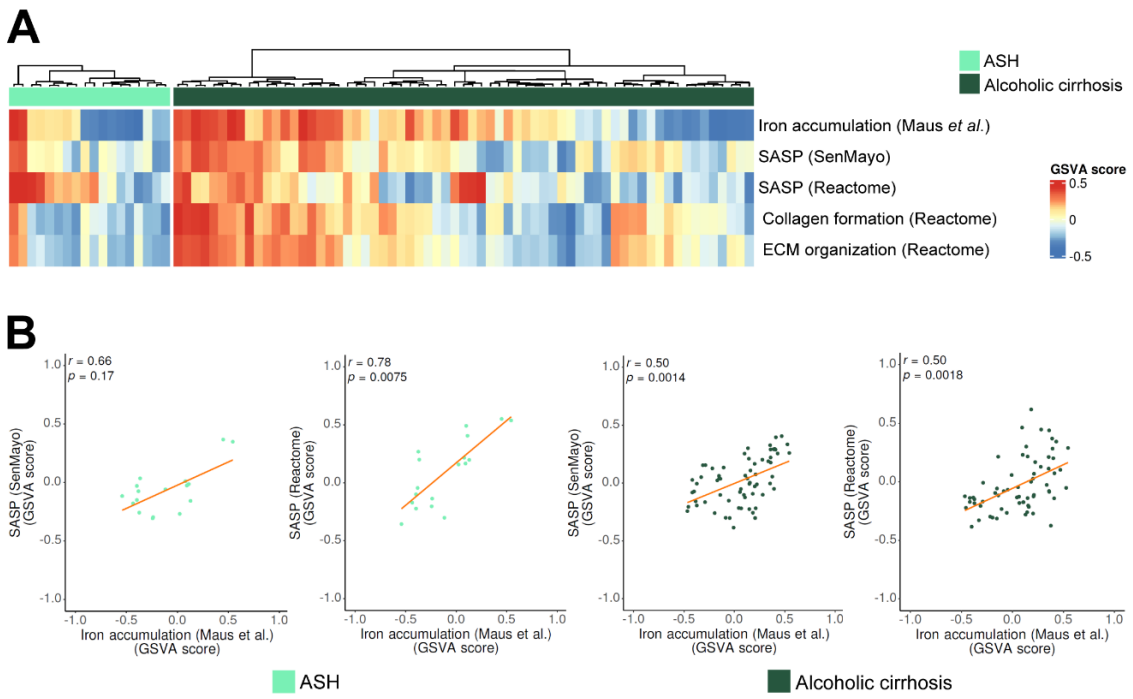

Figure 37. Analysis of iron accumulation and SASP expression in HCC-naïve ASH and alcoholic cirrhosis patients. A. Heatmap showing changes in gene expression for the following gene signatures: iron accumulation (designed by Maus *et al.*, [62]), SASP (SenMayo and Reactome), collagen formation (Reactome) and ECM organization (Reactome) in the Trepo *et al.* cohort of HCC-naïve ASH and alcoholic cirrhosis patients [129]. **B.** Pearson correlation analysis of the relative enrichment of iron accumulation gene signature with SASP (SenMayo and Reactome) gene signatures in ASH (left) and alcoholic cirrhosis (right) patients. Each dot is a sample. All analyses were adjusted for multiple testing with Bonferroni test correction.

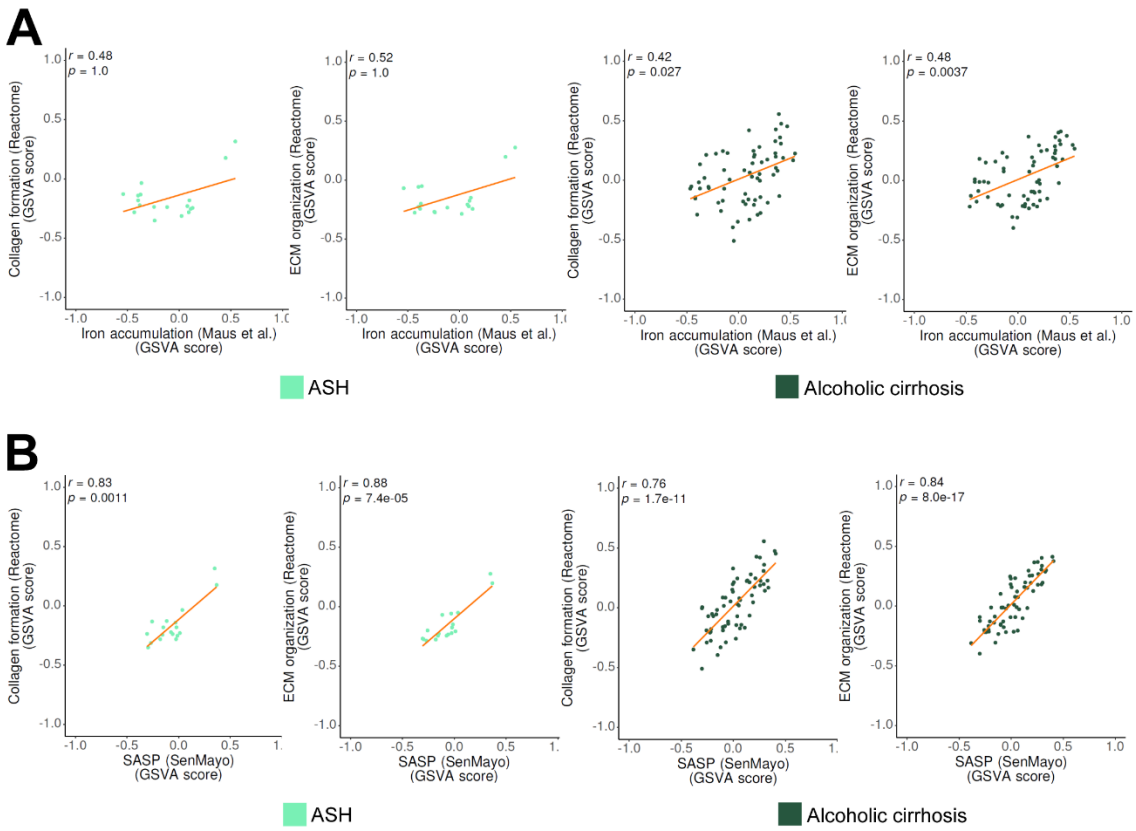

Figure 38. Analysis of the correlation between iron accumulation or SASP expression and fibrotic hallmarks across liver fibrosis stages in HCC-naïve ASH and alcoholic cirrhosis patients. A. Heatmap showing changes in gene expression for the following gene signatures: iron accumulation (designed by Maus *et al.*, [62]), SASP (SenMayo and Reactome), collagen formation (Reactome) and ECM organization (Reactome) in the Trepo *et al.* cohort of HCC-naïve ASH and alcoholic cirrhosis patients [129]. **B.** Pearson correlation analysis of the relative enrichment of iron accumulation gene signature with SASP (SenMayo and Reactome) gene signatures in ASH (left) and alcoholic cirrhosis (right) patients. **C-D.** Pearson correlation analyses of the relative enrichment in the gene signatures related to iron accumulation (C) and relative enrichment of SASP (SenMayo) (D) with collagen formation (Reactome) and ECM organization (Reactome) gene signatures in ASH (left) and alcoholic cirrhosis (right) patients. Each dot is a sample. All analyses were adjusted for multiple testing with Bonferroni test correction.

2. Analysis of the potential therapeutic role of NOX4 in hepatic stellate cell activation. Implications in cholangiocarcinoma.

2.1. Analysis of NOX4 expression in CCA tumour and stromal cells.

As mentioned in the introduction, our group demonstrated that NOX4 mediates TGF-β-induced tumour suppressor actions in hepatocytes and HCC tumour cells. However, the role of NOX4 in CCA has not been described. Preliminary analyses in two public data bases (TCGA and TIGER-LC) and a public cohort from Llovet *et al.* [145] indicated that *NOX4* is upregulated in CCA compared to adjacent non-tumoral liver tissue (NTL; **Figure 39A**). In these years, we have corroborated the same result in a new cohort of patients that we have been developing thanks to the implication of clinician members in our group (Dr. Emilio Ramos, surgeon; and Dr. Teresa Serrano, pathologist at Bellvitge University Hospital; **Figure 39A**). These findings indicated a potential role of NOX4 in CCA tumorigenesis, but surprisingly, *NOX4* expression was not detected when analysed in a battery of CCA cell lines *in vitro*, compared to the positive expression in non-tumoral liver tissue, human hepatocytes or HHC cell lines (**Figure 39B**). These results suggested that other cell types different from the epithelial tumoral cells had to be responsible for the upregulated *NOX4* expression in the tumour.

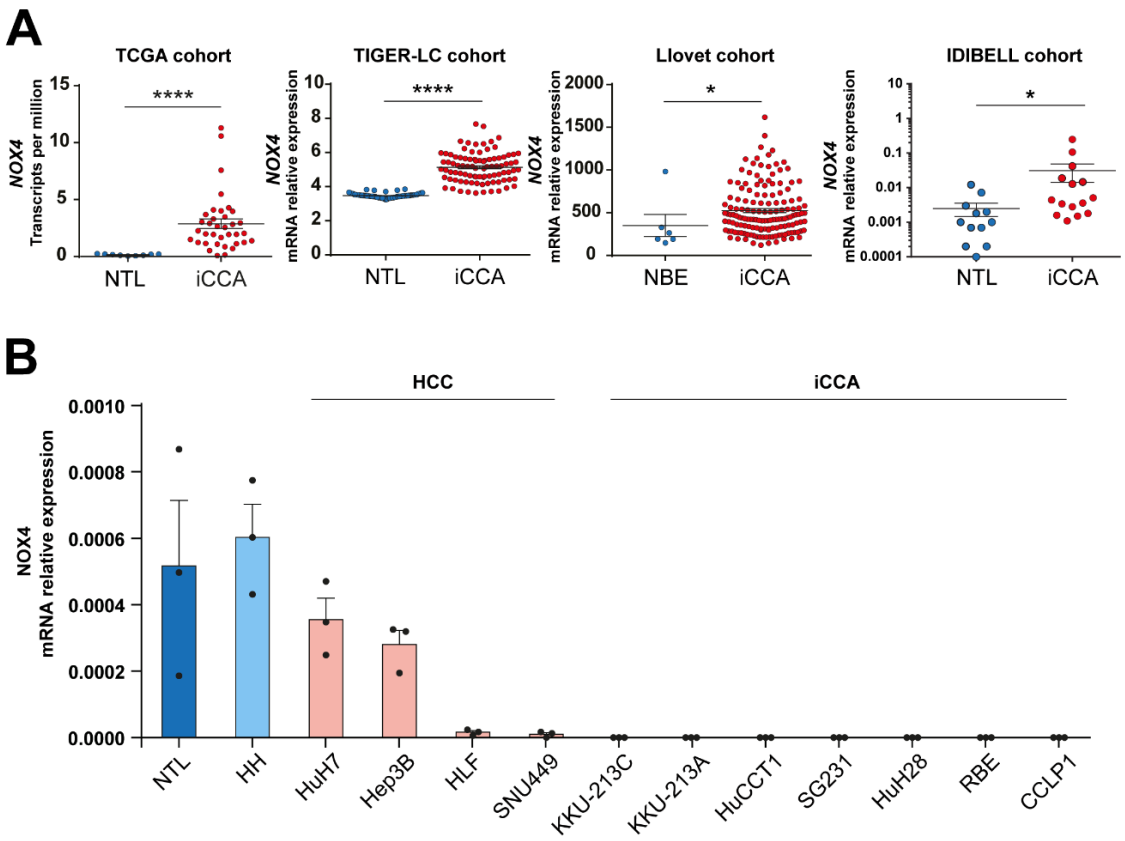

Figure 39. Analysis of *NOX4* expression in intrahepatic cholangiocarcinoma (iCCA). A. *NOX4* mRNA expression in CCA tumours compared to surrounding non-tumoral liver tissue (NTL) or normal biliary epithelial cells (NBE) from the TCGA, TIGER-LC, Llovet *et al.* [145] and IDIBELL cohorts of patients. **B.** *NOX4* mRNA expression in non-tumoral liver (NTL), human hepatocytes (HH), 4 hepatocellular carcinoma (HCC) cell lines and 7 iCCA cell lines, determined by RT-qPCR. Results are expressed as means ± SEM from 3 independent cultures. *p <0.05, **p <0.01, ***p <0.001, ****p <0.0001; as compared to NTL.

To clarify this aspect, we searched for bioinformatic support from Aashreya Ravichandra (Technical University of Munich, Munich, Germany) and explored public data from a single cell RNA sequencing (scRNA-seq) data set (GSE201425) from CCA biopsies. Interestingly, among the different cell types found in the tumour, *NOX4* was mainly expressed in CAF, followed by a lower expression in endothelial cells (**Figure 40A**). Further evaluation of scRNA-seq data allowed us to define the major CAF subpopulations (myCAF, iCAF, vCAF, lipoCAF and apCAF) and to determine that *NOX4* was mainly expressed in myCAF, which are the myofibroblastic ones, and to a lesser extent in apCAF (**Figure 40B**).

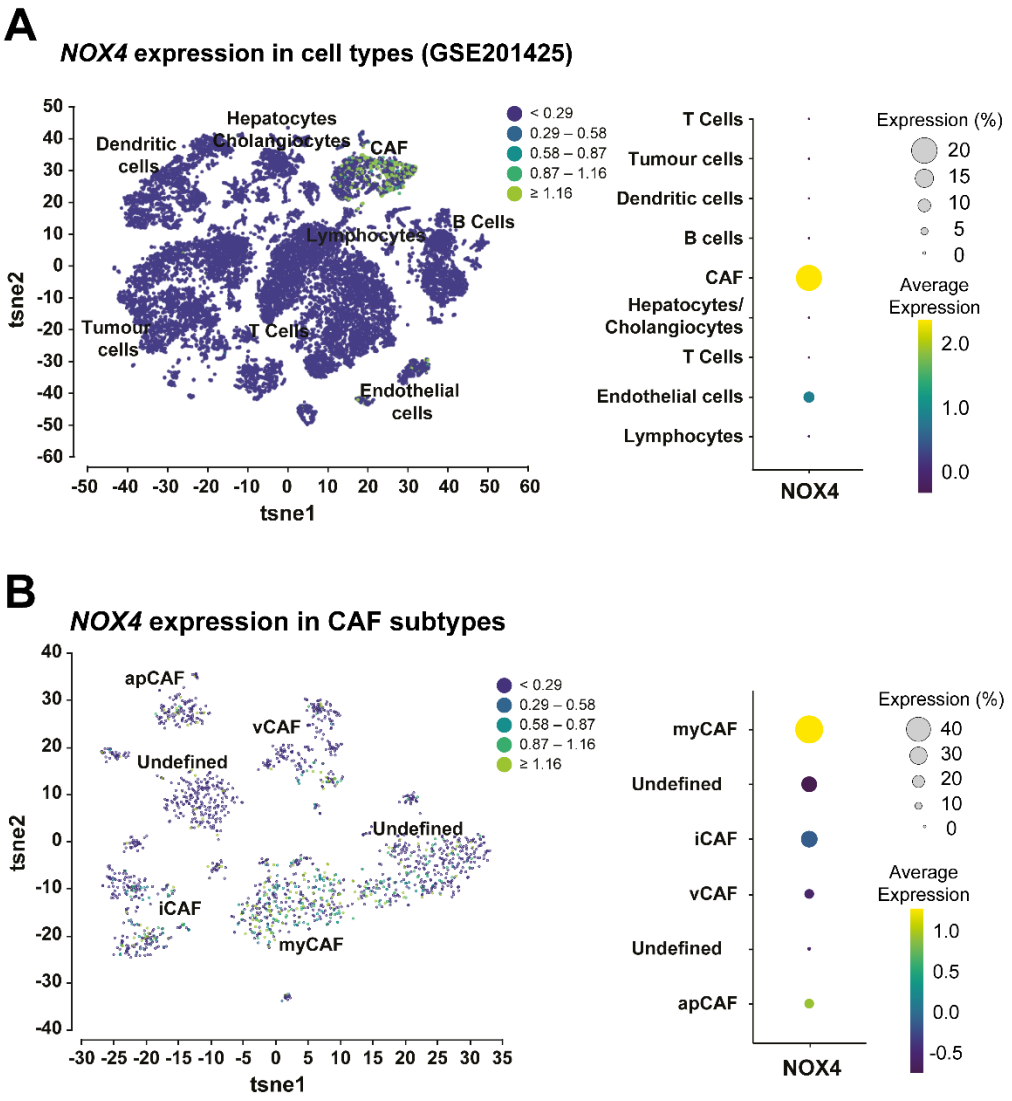

Figure 40. Analysis of NOX4 expression in the different cell types of intrahepatic cholangiocarcinoma (iCCA) and cancer associated fibroblasts (CAF) subtypes. **A.** Umap and dotplot showing *NOX4* expression in scRNA-seq data set GSE201425 from iCCA biopsies. **B.** scRNAseq analysis showing *NOX4* expression in CAF subpopulations. apCAF, antigen-presenting CAF; iCAF, inflammatory CAF; myCAF, myofibroblast CAF; vCAF, vascular CAF.

In parallel, we analysed gene expression in CCA from public data bases that showed a strong significant correlation between the expression of *NOX4* and markers of myofibroblast such as *ACTA2* (α-SMA) and *COL1A1* genes (**Figure 41A**). Moreover, *NOX4* gene expression was found upregulated in the stroma of tumours from iCCA patients compared to non-tumoral stroma in samples obtained by laser microdissection in collaboration with Dr. Cédric Coulouarn (University of Rennes, Rennes, France) (**Figure 41B**). Importantly, we also found a significant correlation between *NOX4* and myofibroblast markers in the stroma of these tumours (**Figure 41C**).

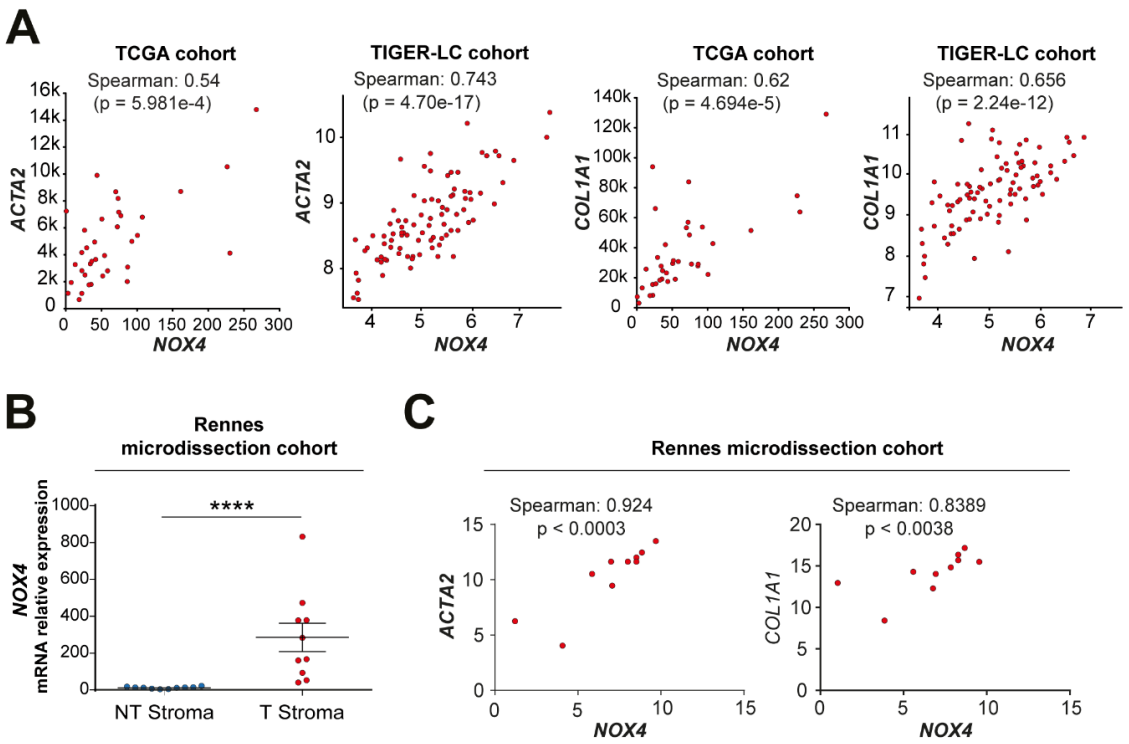

Figure 41. Correlation between NOX4 and myofibroblast-related genes expression in intrahepatic cholangiocarcinoma (iCCA) and iCCA stroma. A. Correlation between *ACTA2* and *COL1A1,* and *NOX4* expression in the TCGA and TIGER-LC iCCA cohorts. **B.** *NOX4* mRNA expression in non-tumoral (NT) or tumoral (T) stromal samples from the Rennes microdissection cohort. **G.** Correlation between *ACTA2* and *COL1A1* with *NOX4* expression in microdissected stroma from 10 iCCA samples. Correlations were determined using Spearman's correlation analysis. ***p <0.001; as compared to NT stroma.

To model *in vitro* the transdifferentiation from HSC to myofibroblast, we used three different human-derived HSC cell lines (LX-2, hTERT and HSC-GFP) and a human primary CAF cell line from iCCA. We first analysed the basal *NOX4* and *ACTA2* gene expression in the HSC cell lines (**Figure 42A-B**) and α-SMA by Western blot, being CAF the cells with the highest protein levels of this myofibroblastic marker, as expected (**Figure 42C**).

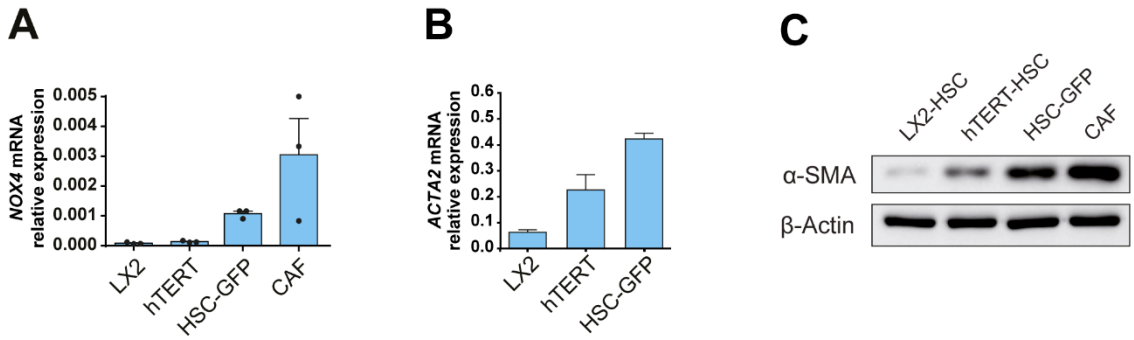

Figure 42. Expression analysis of *NOX4* and *ACTA2* in hepatic stellate cells (HSC) and cancer-associated fibroblasts (CAF) in basal conditions. A-B. *NOX4* and *ACTA2* mRNA basal expression in LX2-HSC, hTERT-HSC and HSC-GFP cells, analysed by RT-qPCR (n = 3). **C.** α-SMA basal protein levels in LX2-HSC, hTERT-HSC, HSC-GFP and CAF from an intrahepatic cholangiocarcinoma patient, analysed by Western blot.

We next studied the response to TGF-β, the major profibrotic cytokine in the liver, as inducer of the transdifferentiation to myofibroblasts in our cells. Exposure to TGF-β induced a rapid increase in the expression of *NOX4* already detectable at 3 h, compared to the vehicle, concomitant with an increased expression of *ACTA2* and *COL1A1*, which were upregulated at longer times (24-72 h) (**Figure 43**). The fact that the upregulation of *NOX4* precedes the increase in expression of *ACTA2* and *COL1A1* might suggest that indeed NOX4 could be mediating HSC activation.

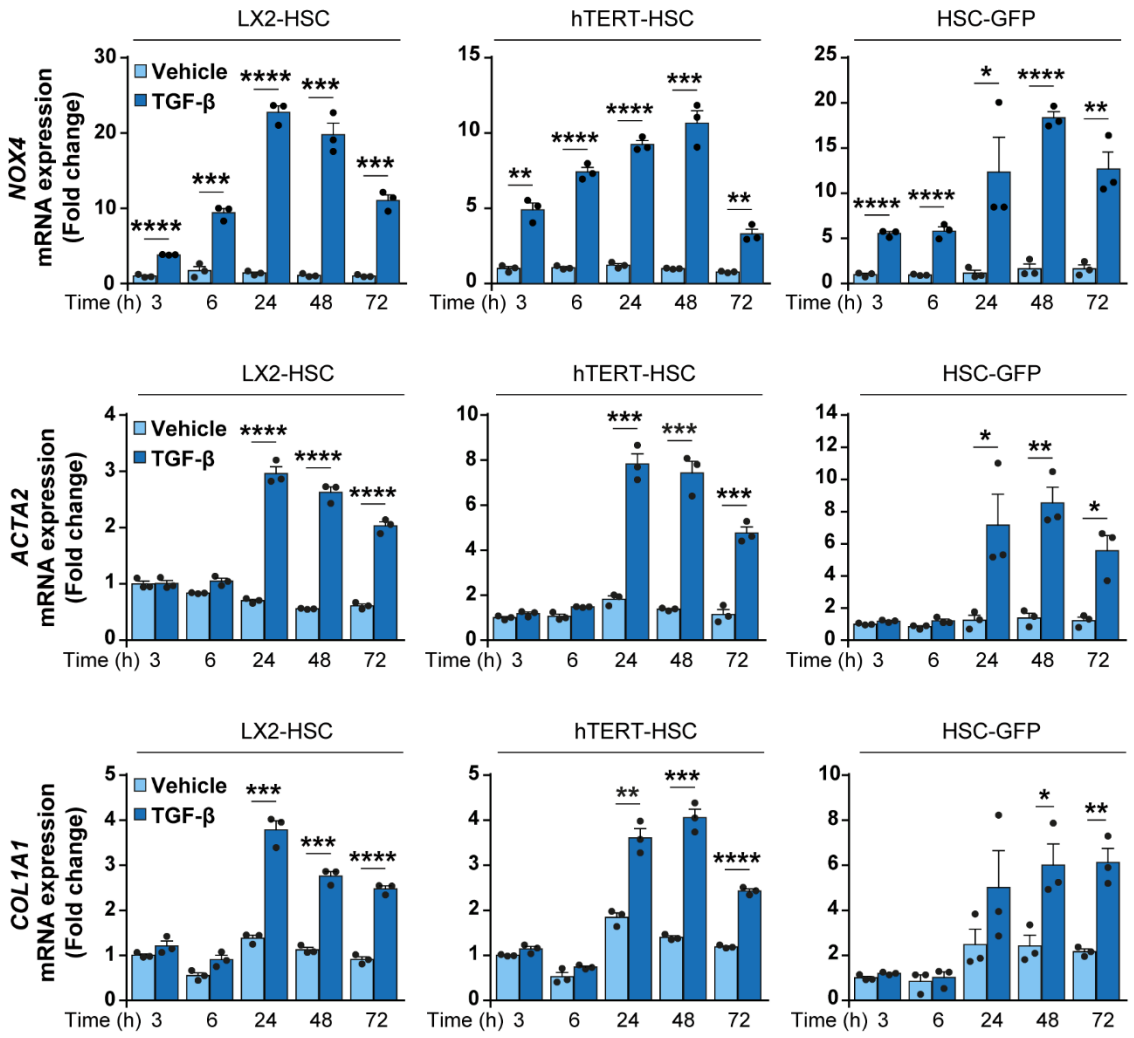

Figure 43. Analysis of the gene expression regulation by TGF-β of *NOX4*, *ACTA2* and *COL1A1* genes in hepatic stellate cells (HSC). A-C. *NOX4*, *ACTA2* and *COL1A1* mRNA expression in LX2-HSC, hTERT-HSC and HSC-GFP cells upon TGF-β (2 ng/mL) treatment at different times (n = 3). *p <0.05, **p <0.01, ***p <0.001, ****p <0.0001; as compared to the vehicle.

These results were corroborated at the protein level by Western blot (**Figure 44**), reaching the peak of NOX4, α-SMA and collagen content at 48 h after TGF-β treatment.

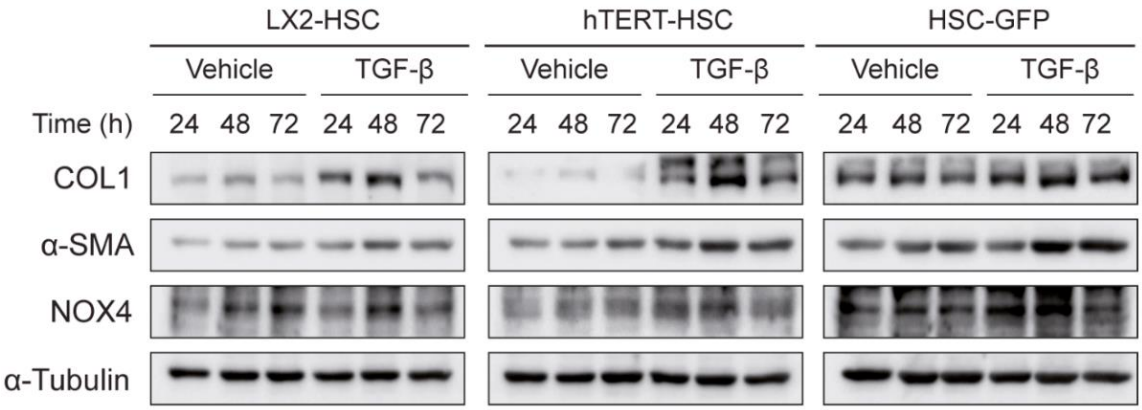

Figure 44. Analysis of the protein levels regulation by TGF-β of and Collagen 1, α-SMA and NOX4 in hepatic stellate cells (HSC). Collagen 1, α-SMA and NOX4 protein levels analysed by Western blot in LX2-HSC, hTERT-HSC and HSC-GFP cells after TGF-β treatment at different times.

To validate if this regulation by TGFβ observed in human HSC cell lines could also be occurring in patients, we used CAFs isolated from an iCCA patient from Paris, which responded to TGF-β in a similar manner at 48 h (**Figure 45**).

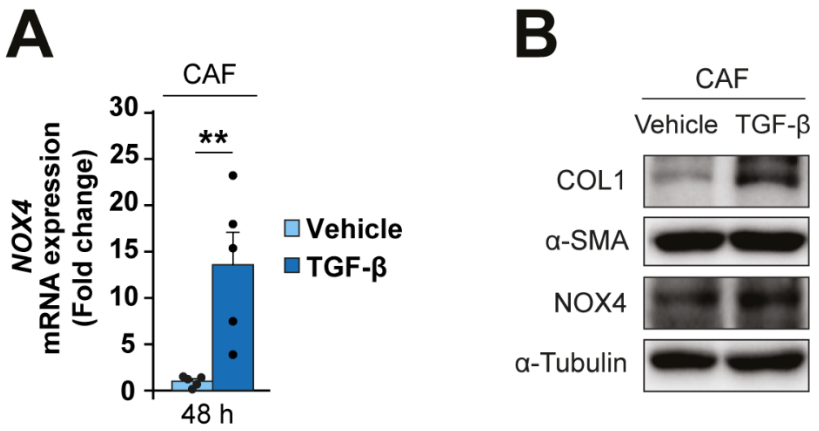

Figure 45. Analysis of the response to TGF-β in terms of Collagen 1, α-SMA and NOX4 protein levels in cancer-associated fibroblasts (CAF) from a patient. A. *NOX4* mRNA expression in CAF isolated from an intrahepatic cholangiocarcinoma (iCCA) patient upon TGF-β (2 ng/mL) treatment at 48 h, analysed by RT-qPCR (n = 5). **B.** Collagen 1, α-SMA and NOX4 protein levels analysed by Western blot in CAF from an iCCA patient after TGF-β treatment at 48 h. **p <0.01; as compared to the vehicle.

Overall, these results demonstrate that in iCCA, NOX4 is mainly expressed in the fibroblasts, while absent in the tumour cell, and its levels increase during fibroblast transdifferentiation towards CAF, suggesting that NOX4 downstream TGF-β might be playing a relevant role in this activation process, as we hypothesized based on the existing literature [103-106, 108, 111].

2.2. Generation and characterization of a syngeneic orthotopic CCA model in wild type and NOX4$^{-/-}$ mice to evaluate the role of stromal NOX4 on tumour progression.

To evaluate the potential impact of targeting NOX4 in the stroma of CCA we performed a syngeneic orthotopic model by implanting the murine SB1 CCA cells in wild type (WT) and NOX4-/- mice (further details in Materials and Methods section, **Figure 10**) and see how tumours develop in the stroma of these mice. We hypothesized that in the knockout mice (in complete absence of NOX4 functions), the transdifferentiation process from HSC to CAF would be potentially impaired, thus displaying differences in the stroma compared to WT mice and consequently affecting tumour growth.

Surprisingly, despite the absence of NOX4, tumours from WT and NOX4-/- mice were identical in size and expression of *Krt19*, a marker of CCA tumour cell. When analysing the stromal compartment, we did not find any difference in the content of α-Sma and collagen deposition as analysed by IHC and Picro-Sirius Red staining, respectively, neither at the mRNA level (**Figure 46**). These results indicated that somehow the HSC in these tumours could be activated into CAFs despite the lack of NOX4 expression.

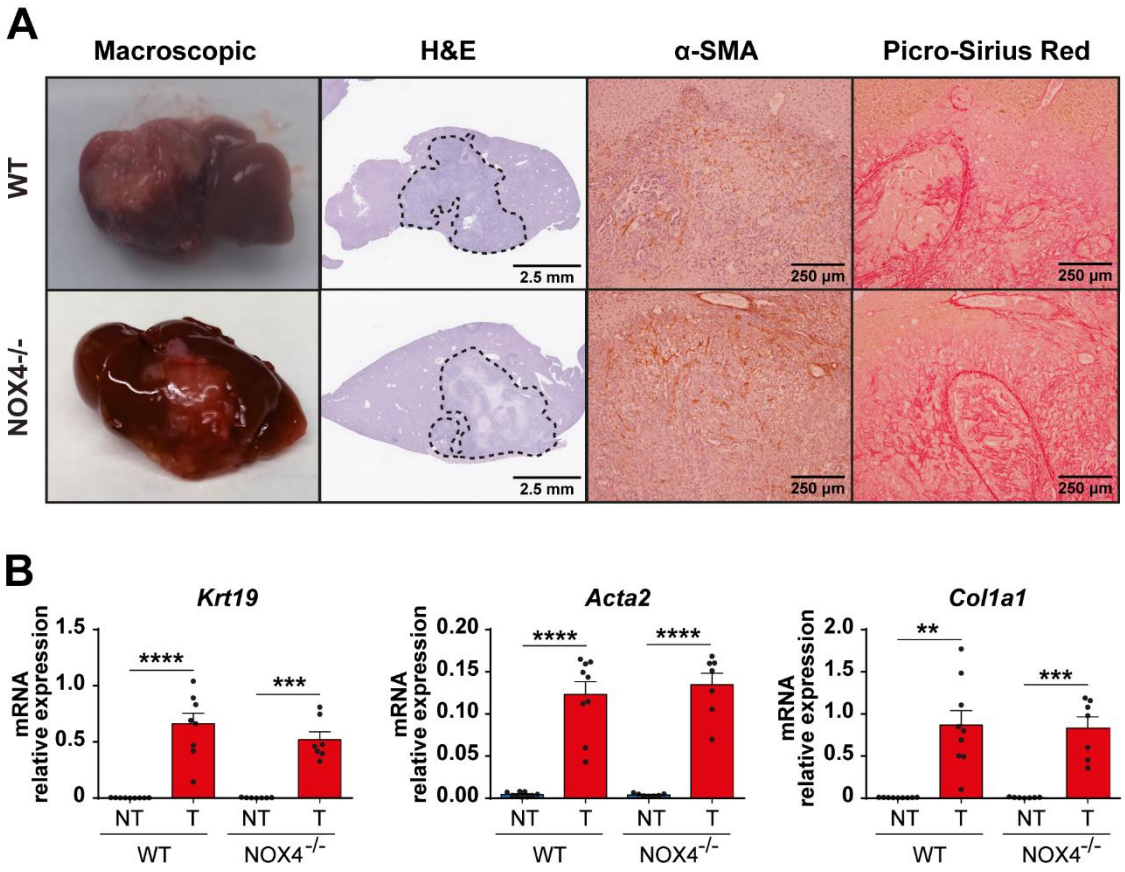

Figure 46. Generation and characterization of a syngeneic orthotopic iCCA mouse model. A. Representative macroscopic images of the tumours at term and tissue sections stained with haematoxylin-eosin, to illustrate the size of the tumours, α-SMA to visualize CAF (cancer-associated fibroblasts) and Picro-Sirius Red staining to reveal collagen deposition. **B.** RT-qPCR of the *Krt19* gene (marker of CCA), and *ACTA2* and *COL1A1* to analyse myofibroblastic/CAF hallmarks expression. Data expressed as mean ± SEM. Student's t-Test; **p<0.01; ***p<0.001; ****p<0.0001.

2.3. Generation of loss of function experimental models of NOX4 in human hepatic stellate cells by CRISPR-Cas9 and siRNA to analyse transdifferentiation into myofibroblasts *in vitro*.

To answer the new questions arised from the unexpected results in the mouse model, we decided to model the stable depletion of NOX4 *in vitro* in fibroblasts to ascertain the exact role of NOX4 in the transdifferentiation of these cells. Among the HSC cell lines available in the lab, we chose the hTERT-HSC to perform a CRISPR-Cas9 mediated silencing of NOX4 because they are immortalized and express higher levels of NOX4 than LX2-HSC. After stably silencing NOX4, as shown by mRNA and protein levels (**Figure 47A-B**) (see more details about the model generation in Materials and Methods section), the CRISPR-Control and CRISPR-NOX4 cells

showed similar responses to TGF-β in terms of *ACTA2* (α-SMA) and *COL1A1* expression (**Figure 47A**), confirmed by Western blot (**Figure 47B**).

Since NOX4 produces H_2O_2 as a result of its catalytic activity, we measured H_2O_2 levels by Amplex Red assay. As expected, TGF-β1 increased ROS levels in CRISPR-Control cells, while basal ROS levels were already augmented in CRISPR-NOX4 cells and did not change after TGF-β treatment (**Figure 47C**). This result led us to think that there could be a compensatory mechanism increasing ROS levels enough to allow TGF-β-induced fibroblast transdifferentiation.

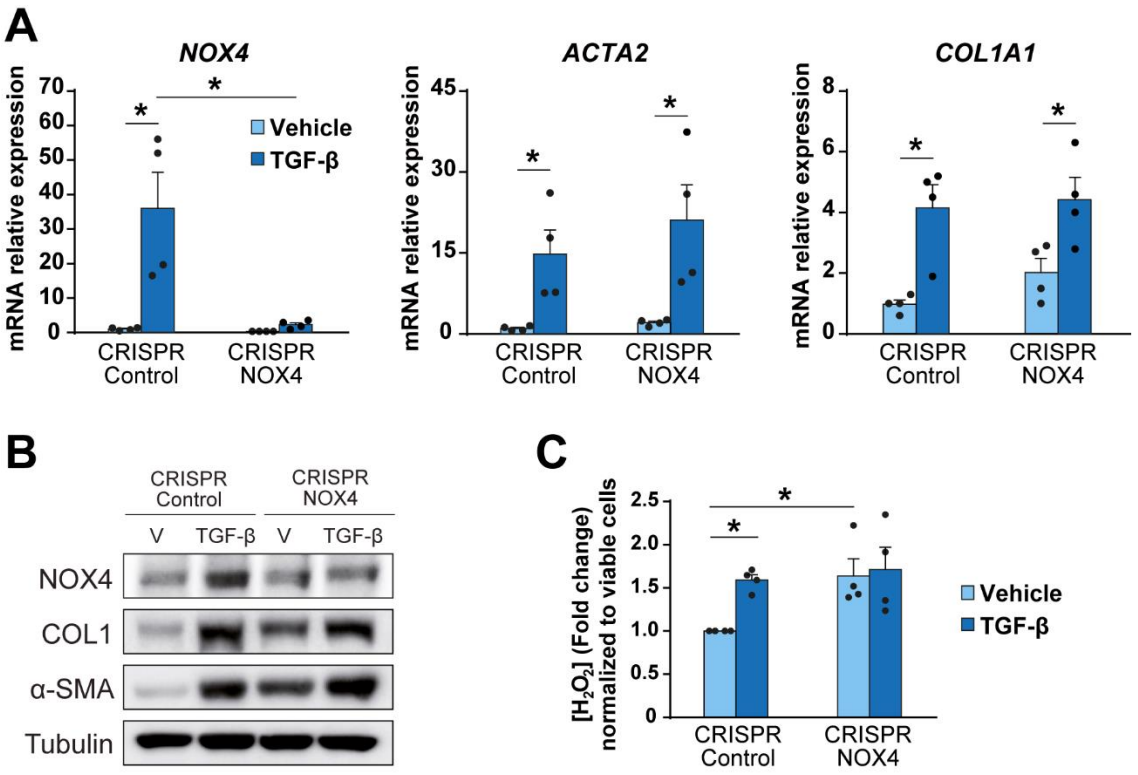

Figure 47. Characterization of myofibroblastic transdifferentiation of a NOX4-silenced model by CRISPR/Cas9 in human HSC. hTERT-CRISPR-Control and CRISPR-NOX4 cells were generated by CRISPR/Cas9 technology as detailed in Material and Methods section. **A-B.** mRNA (A) and protein (B) expression of NOX4, *ACTA2* (α-SMA) and *COL1A1* (Collagen 1, COL1) after TGF-β treatment for 48 h in the hTERT-HSC CRISPR-Control and CRISPR-NOX4 cells, analysed by RT-qPCR and Western blot. **C.** H_2O_2 production measured by Amplex red in CRISPR-Control and CRISPR-NOX4 cells after TGF-β treatment for 24 h. Values are expressed as mean ± SEM (n = 4). *p<0.05.

As described in the introduction, NADPH oxidases often present cross-regulation between isoforms, so the expression or function of one NOX can affect the others. To ascertain if another NADPH oxidase was involved in the augmented

ROS levels observed in CRISPR-NOX4 cells, we used diphenyleneiodonium chloride (DPI, an NADPH oxidase inhibitor), which abolished TGF-β-induced increase of α-SMA and collagen 1 protein levels (**Figure 48A**) and decreased ROS levels, analysed with Amplex red probe (**Figure 48B**).

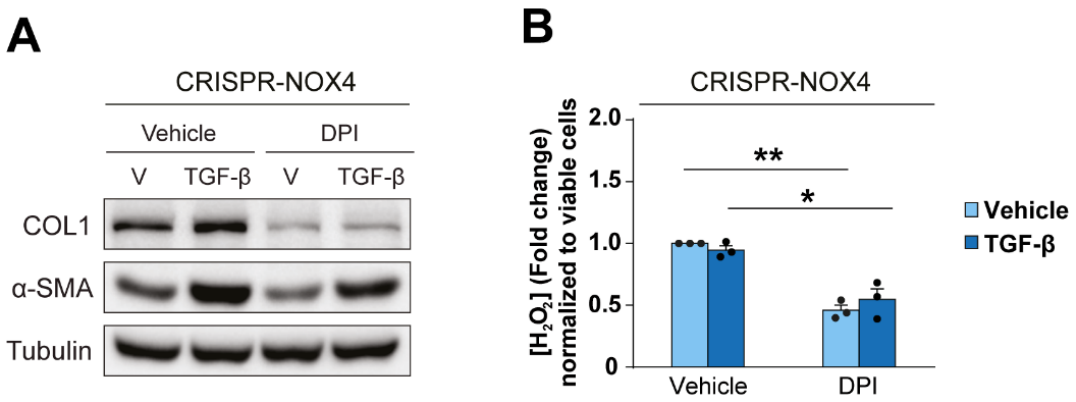

Figure 48. Effects of diphenyleneiodonium (DPI) on CRISPR-NOX4 cells transdifferentiation. hTERT CRISPR-NOX4 cells were treated with TGF-β (2 ng/mL) for 48 h in absence or presence of the NADPH oxidase inhibitor DPI (2.5 µM). **A.** Protein expression of α-SMA and COL1A1. **B.** H_2O_2 production measured by Amplex Red assay. STATISTICS. Data are presented as mean ± SEM (n = 3). *p<0.05; **p<0.01.

These results confirmed our suspicions that an NADPH oxidase was mediating HSC transdifferentiation to myofibroblast by TGF-β in absence of NOX4. Therefore, we focused on the other members of the family and their regulatory proteins. Our analyses unveiled a strong increase in the expression of p22phox (*CYBA*) and a stable and detectable expression of NOX1 (**Figure 49A-B**), while no other NOX (NOX2, NOX3 or NOX5) was detectable and the rest of regulatory components did not suffer a change in expression that could account for the increased ROS levels (**Figure 49C**). Given these results and previous literature [111], we thought on NOX1 as the most probable responsible for HSC activation in our CRISPR-NOX4 cells.

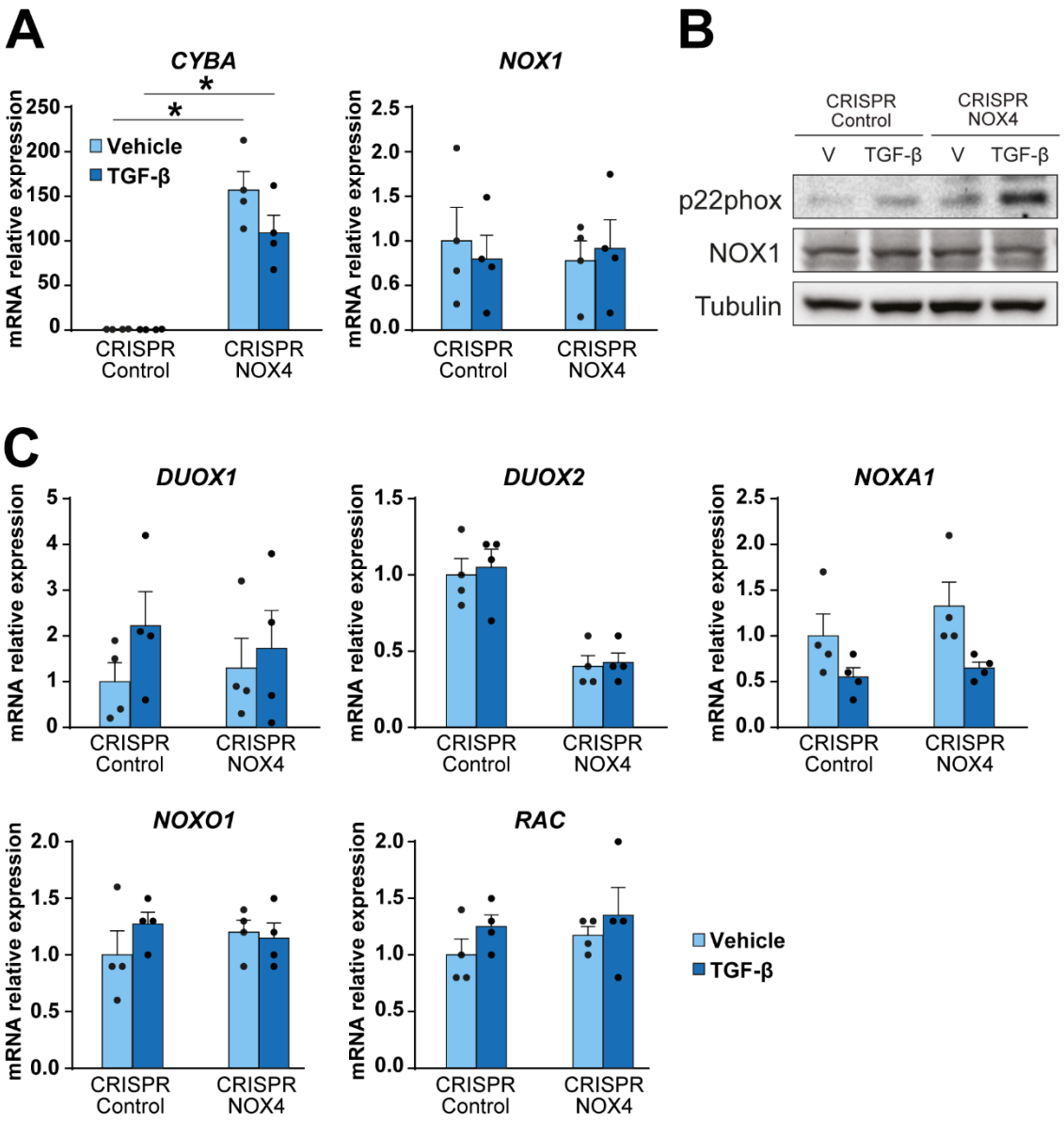

Figure 49. Analysis of expression of other NOX family members and regulatory proteins in response to TGF-β in CRISPR-Control and CRISPR-NOX4 cells. hTERT CRISPR-Control and CRISPR-NOX4 cells were treated with TGF-β (2 ng/mL) for 48 h. **A.** mRNA relative expression of *CYBA* (p22phox) and *NOX1* genes, analysed by RT-qPCR. **B.** Protein levels of p22phox and NOX1, determined by Western blot. **C.** mRNA relative expression of *DUOX1*, *DUOX2*, *NOXA1*, *NOXO1* and *RAC*, determined by RT-qPCR. mRNA expression of *NOX2*, *NOX3* and *NOX5* were measured but not detected. Values are expressed as mean ± SEM (n = 4). *p<0.05.

Since NOX4 is constitutively active and it is considered regulated at the transcriptional level, while NOX1 expression is mostly stable but its activity is regulated by other partners, we hypothesized that the increase in p22phox resulted from NOX4 knock-down was able to further increase the activity of NOX1. To validate this possibility, we downregulated NOX1 with siRNA transfection in CRISPR-NOX4

cells, using a scramble sequence as control. Silencing NOX1 in CRISPR-NOX4 cells abolished TGF-β-induced increase of α-SMA and Collagen 1 and reduced ROS levels (**Figure 50**), similarly to the effects observed with DPI.

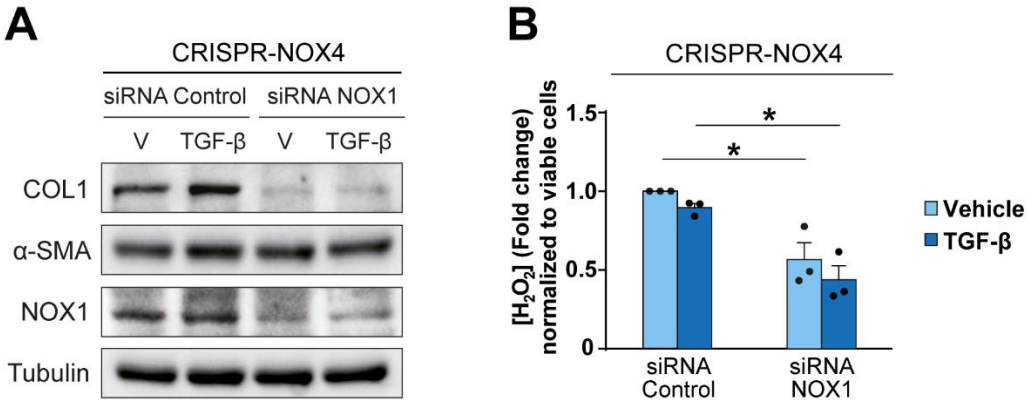

Figure 50. Analysis of transdifferentiation of CRISPR-NOX4 cells upon NOX1 silencing by siRNA. hTERT CRISPR-NOX4 cells were transfected with small interfering RNAs (siRNA) against NOX1 or a scramble sequence as control and treated with TGF-β for 48 h. **A.** Protein expression of NOX1, α-SMA and Collagen 1 (COL1A1), analysed by Western blot. **B.** H_2O_2 production measured by Amplex Red assay (n = 3). *p<0.05.

These results suggested that NOX1 could be replacing NOX4 when is permanently silenced by CRISPR/Cas9. However, we had no evidence of which are the specific roles of these NOXs in normal conditions, when both are expressed.

To finally decipher the actual participation of NOX4 and/or NOX1 in TGF-β induced fibroblast transdifferentiation, we performed further siRNA studies in wild type HSC cells expressing endogenously both NOXs. Importantly, we observed that individual silencing of NOX1 or NOX4 did not impair the induction of myofibroblast markers α-SMA and Collagen 1 by TGF-β. Indeed, only double NOX4/NOX1 downregulation was able to impair TGF-β1-induced activation in hTERT-HSC cells (**Figure 51A**), and these results were validated in another HSC cell line, LX-2. (**Figure 51B**).

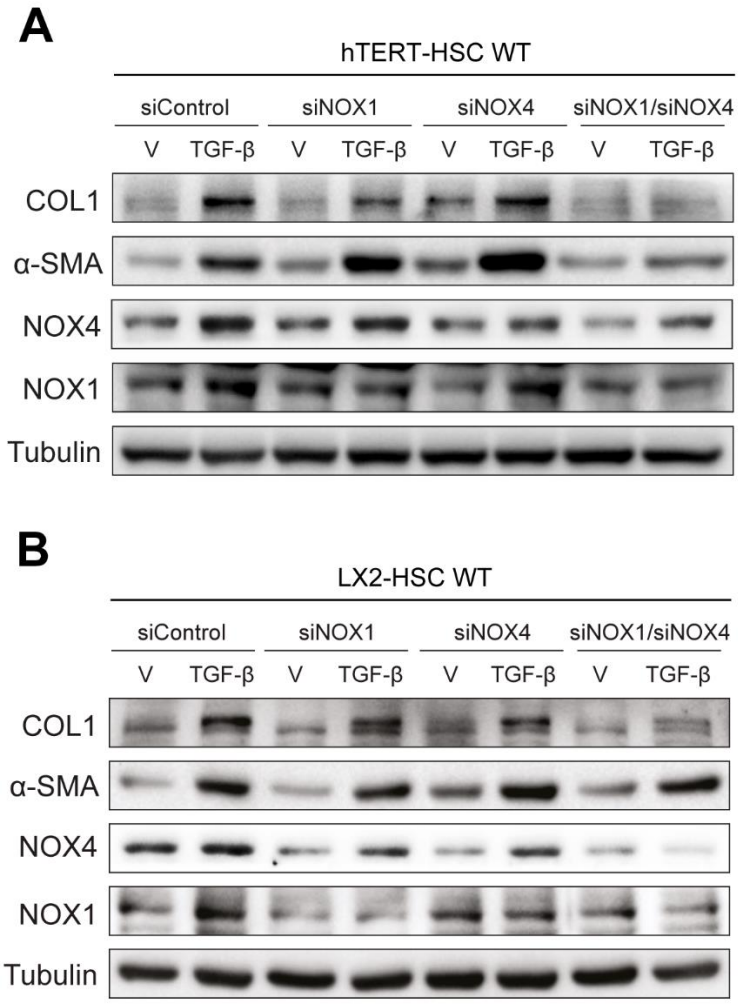

Figure 51. Analysis of transdifferentiation of hTERT and LX2 HSC wild type cells upon NOX1/NOX4 silencing by siRNA. hTERT and LX2 HSC wild-type cells were transfected with small interfering RNAs (siRNA) against NOX1, NOX4 or both, or a scramble sequence as control, and treated with TGF-β for 48 h. **A-B.** Protein expression of Collagen 1 (COL1A1), α-SMA, NOX1, α-SMA, NOX1 and NOX4 analysed by Western blot.

We then decided to explore the clinical relevance of these results and analysed a cohort of iCCA patients (GSE244807) with the aid of Sara Hijazo-Pechero (IDIBELL, L'Hospitalet de Llobregat, Spain). Bioinformatic analysis in this cohort correlated with our results *in vitro* since patients with low expression of both *NOX4* and *NOX1* showed better survival than those with high expression of one or both NOXs (**Figure 52**), indicating the important role played by the duet NOX4/NOX1 in CCA pathobiology.

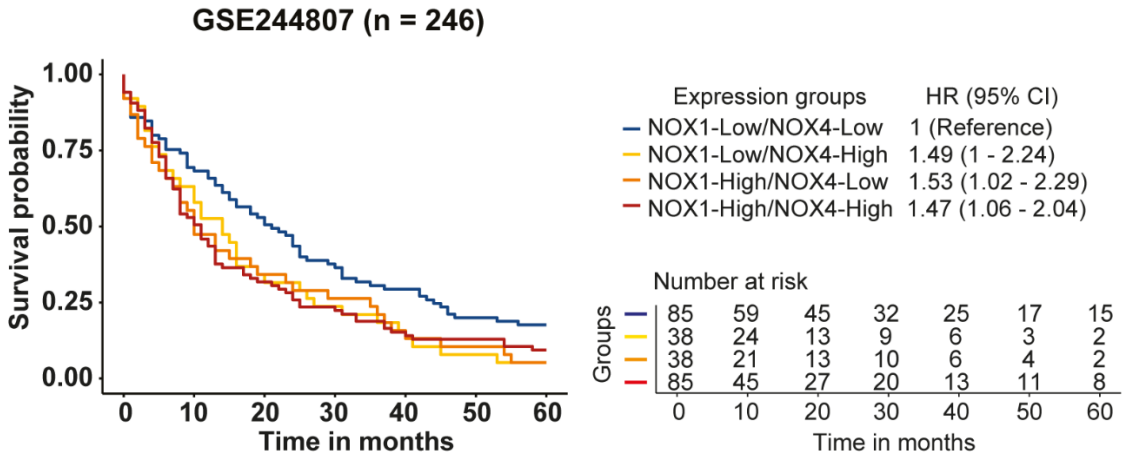

Figure 52. Survival probability of intrahepatic cholangiocarcinoma patients based on *NOX1* and *NOX4* gene expression. 5-year survival probability of patients from GSE244807 cohort stratified based on *NOX4* and *NOX1* expression (log-rank test).

2.4. Evaluation of the efficacy of NOX4 inhibitors on HSC transdifferentiation *in vitro*.

Looking for a potential translational application about the necessity of impairing the activity of both NOXs to blunt fibroblast transdifferentiation in CCA, we decided to evaluate the effects of setanaxib, a dual NOX4/NOX1 inhibitor that has been successfully tested in clinical trials of cholangiopathies (NCT03226067) [146]. For this purpose, we first started validating this inhibitor in the transdifferentiation of LX2-HSC, hTERT-HSC and HSC-GFP that show different degrees of basal activation, and we further stimulated them with TGF-β in absence or presence of setanaxib. Analyses by Western blot showed that setanaxib was able to impair TGF-β-induced increment in the protein levels of both α-SMA and Collagen 1 in the three cell lines (**Figure 53**).

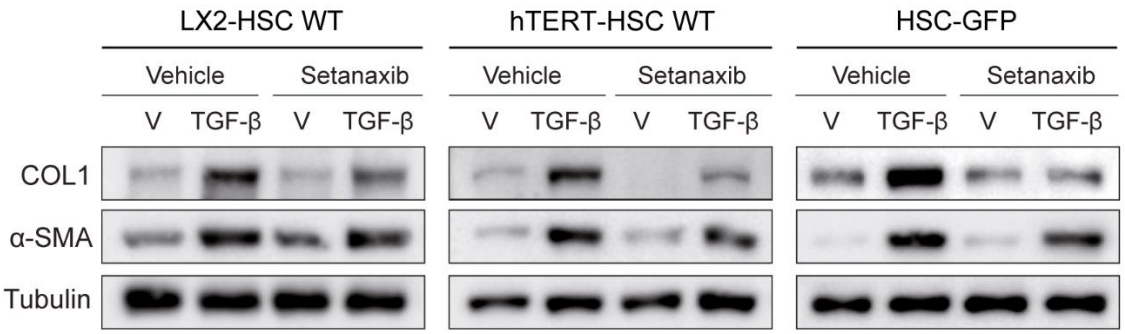

Figure 53. Effects of setanaxib on TGF-β-induced fibroblast transdifferentiation in human HSC. Representative images of Western blot analysis of Collagen 1 (COL1) and α-SMA in hepatic stellate cell (HSC) lines treated with TGF-β or the vehicle in absence or presence of setanaxib, or the vehicle, for 48 h.

Next, we decided to evaluate the transcriptomic effects of setanaxib in HSC by RNA-seq to better understand the molecular mechanisms and pathways regulated by this drug. Raw data analysis was performed by Beatriz Martín-Mur (CNAG, Barcelona). As seen in the **Figure 54**, GSEA analysis showed that setanaxib was able to inhibit many signalling pathways involved in myofibroblasts activation, as well as ECM organization.

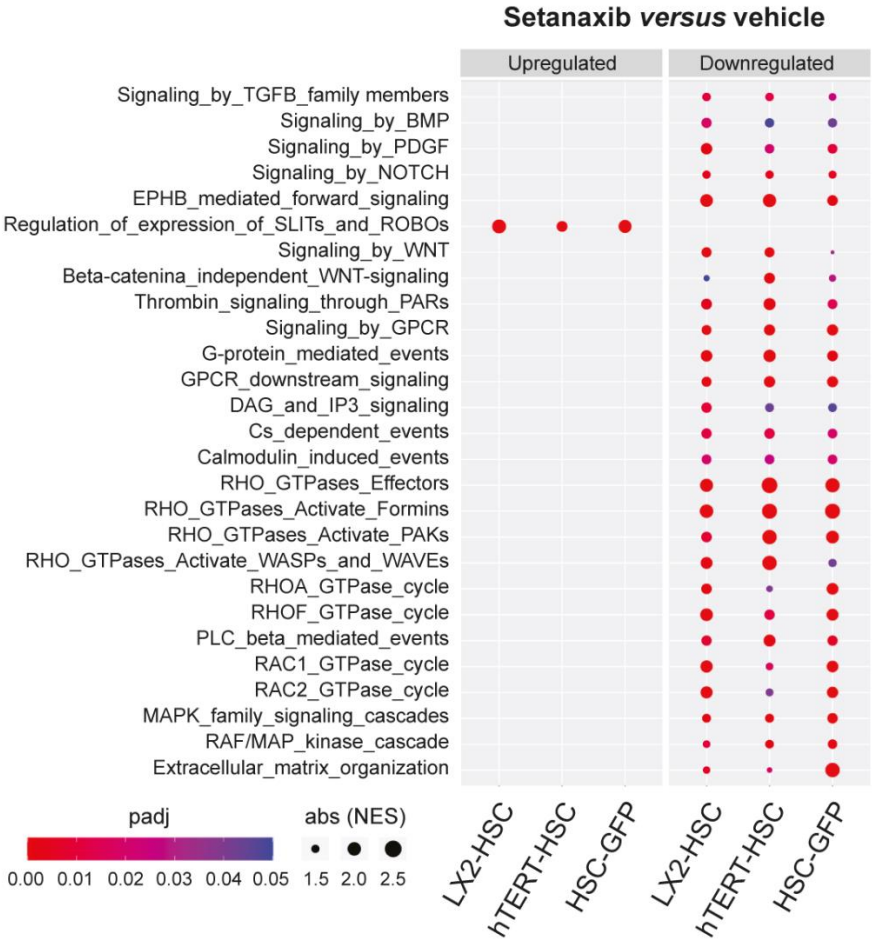

Figure 54. Effects of setanaxib on human HSC cell lines analysed by RNA-seq. Dot plot showing differences in enrichment for key events related with signalling pathways involved in myofibroblast transdifferentiation in hepatic stellate cell (HSC) lines treated with setanaxib or the vehicle.

Since setanaxib was able to inhibit myofibroblastic functions in human HSC, we decided to test its impact on iCCA growth *in vitro* using mixed spheroids formed by iCCA cells and HSC-GFP. Setanaxib had no impact on the size of spheroids formed by tumour cells alone (**Figure 55A**), but significantly reduced the growth of mixed spheroids (**Figure 55B**), suggesting that setanaxib affects primarily the fibroblastic cells and does not apparently have undesired effects on tumour cell growth.

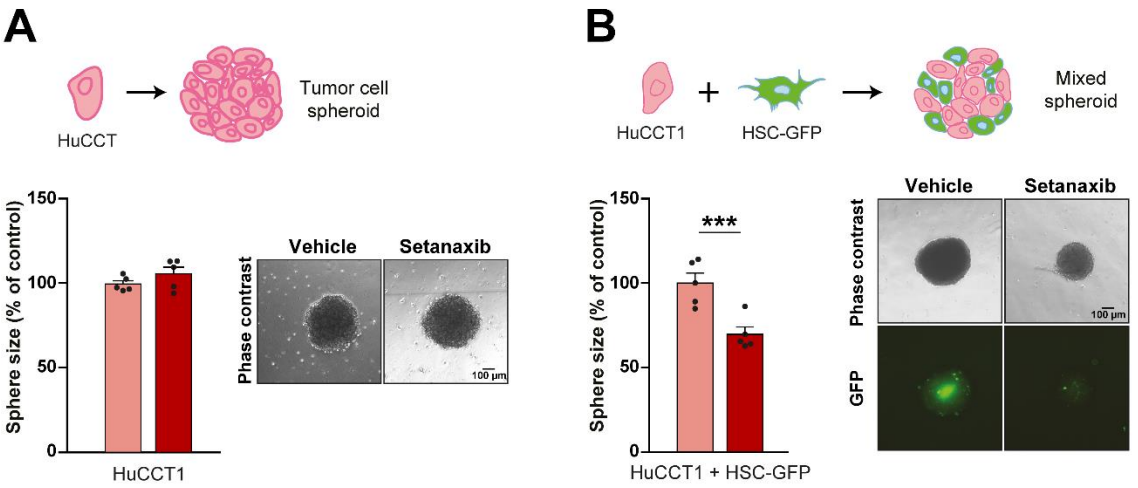

Figure 55. Effect of setanaxib on tumoral growth in 3D-spheroids. A. Size of spheres from HuCCT1 cells after 4 days of treatment with setanaxib. Representative phase contrast and images of spheres at the time of size analysis are shown. **B.** Size of mixed spheres from HuCCT1 cells in combination with hepatic stellate cells (HSC-GFP) after 4 days of treatment with setanaxib. Representative phase contrast images of spheres at the time of size analysis are shown. Values are expressed as means ± SEM (n = 5). ***, $p < 0.001$; as compared with the vehicle.

To have a closer approach to patients, we analysed the efficacy of setanaxib on CAF isolated from three iCCA patients. We used CAF from two patients obtained in collaboration with Laura Sererols-Viñas and Dr. Silvia Affò (IDIBAPS, Barcelona, Spain); and one patient obtained thanks to Dr. Laura Fouassier (CRSA, Paris, France). Indeed, setanaxib was able to reduce the protein levels of CAF markers both in absence and presence of TGF-β, especially that of Collagen 1, in CAF from three different patients (one from Paris and one from Barcelona) (**Figure 56**). In summary, these data suggest that setanaxib may be a good strategy to target tumour growth by targeting CAF functions in CCA.

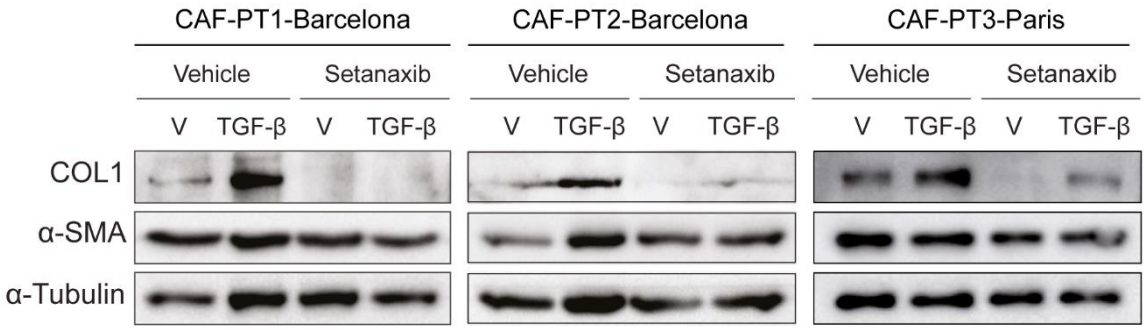

Figure 56. Effect of setanaxib on cancer associated fibroblast activation. Representative images of Western blot analysis of COL1 and α-SMA in CAF treated with TGF-β (2 ng/mL) or the vehicle in absence or presence of setanaxib (40 µM) for 48 hours.

2.5. Evaluation of the efficacy of NOX4 inhibitors on tumor progression in a murine AKT-YAP hydrodynamic tail vein injection CCA model.

Based on our *in vitro* studies, we hypothesized that the use of NOX4/NOX1 inhibitors, such as setanaxib, would reduce tumour growth by specifically targeting transdifferentiation in both newly recruited HSC and CAF. Thus, as a final step, we decided to evaluate the effects of setanaxib in the AKT-YAP-induced CCA model generated by hydrodynamic tail-vein injection of the vectors, that shows a prominent and desmoplastic stroma with collagen deposition, as observed in a pilot experiment to set up the model (**Figure 57**). Briefly, we induced tumorigenesis (see more details in the Materials and Methods section, **Figure 11**) and four weeks later, once the tumours were established, we treated the animals for two additional weeks before sacrifice. Analysis of the livers showed reduced number and maximal size of tumours in the setanaxib group (**Figure 58**).

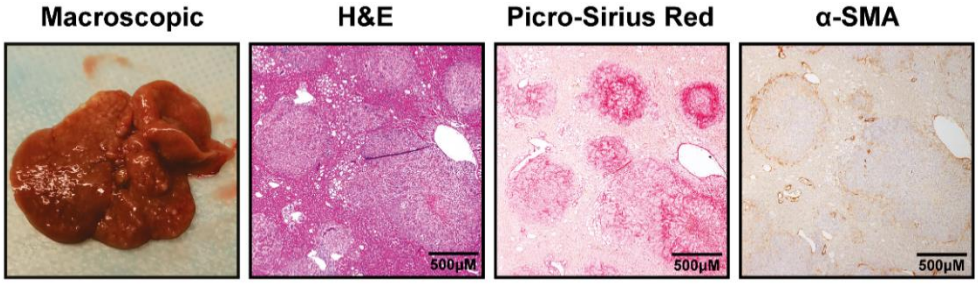

Figure 57. Caracterization of an intrahepatic cholangiocarcinoma mouse model by hydrodynamic tail vein injection with AKT/YAP vectors. Tumours were generated as described in Materials and methods section, but no treatment was administered. Four weeks later, once tumours were established, liver tissues were collected and stained for haematoxylin-eosin (H&E) and Picro-Sirius Red, and immunostained for α-SMA.

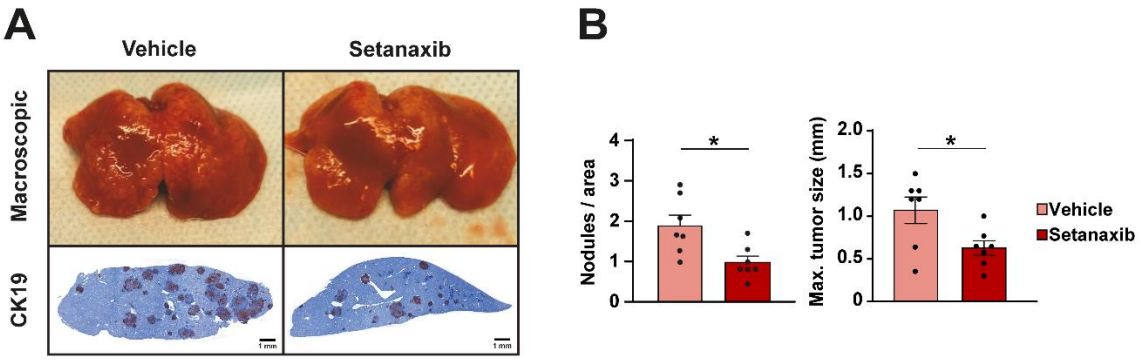

Figure 58. Effects of dual NOX4/NOX1 inhibition with setanaxib on tumour burden *in vivo* in the AKT/YAP mouse intrahepatic cholangiocarcinoma (iCCA) model. CCA tumours were induced using the HTVI AKT-YAP model and treated with setanaxib (60 mg/kg) or the vehicle. A. Representative macroscopic images of livers and Cytokeratin-19 (CK19) IHC (to mark CCA cells) from animals treated with setanaxib or the vehicle. **B.** Quantification of nodules/area and maximal tumour size for each mouse. Values are expressed as mean ± SEM from 7 animals. *, $p < 0.05$; as compared with vehicle group.

Histopathological analyses for this experiment were performed by a pathologist, Dr. Alexander Scheiter (Institute of Pathology, Regensburg, Germany), and two investigators: Dr. Ester Gonzalez-Sanchez and Dr. Javier Vaquero (CIC-IBMCC, CSIC-Universidad de Salamanca, Salamanca). Livers from vehicle-treated mice contained mostly undifferentiated CCA with mainly trabecular growth within a desmoplastic stroma. Tumours showed expansive rather than infiltrative growth. On the contrary, setanaxib-treated livers showed smaller tumour nodules with pycnotic nuclei and the appearance of lower grade lesions. In this regard, quantification of IHC showed a reduced percentage of Ki67 positive cells (proliferative) and increased cleaved caspase 3 (cCasp3) staining (apoptotic) in setanaxib group (**Figure 59A**). Further analyses of the TME showed similar disposition of CAF within the tumours in both groups, although the staining was less intense in the setanaxib group. Accordingly, setanaxib-treated mice showed reduced Picro-Sirius Red staining compared to vehicle group, indicative of less collagen deposition by CAF (**Figure 59B**).

Altogether, these results corroborated our previous *in vitro* observations. Moreover, it is known that ECM deposition by CAF, including different collagens, increases tumour stiffness and forms a barrier that impedes T cell access into the interior of the tumours, impacting negatively in the efficacy of current immunotherapies [147]. In this sense, analysis of CD4 T cells showed that these cells are localized in the surroundings of tumour nodules in this animal model.

Interestingly, CD4 T cells remained excluded in the peritumoral zone in the vehicle, while setanaxib treatment increased the intratumoral presence of CD4 T cells. Furthermore, treatment with setanaxib was also able to reduce the high expression of the immune checkpoint (ICP) PD-L1 in the tumour margins (**Figure 59C**).

Other immune subpopulations were analysed by immunohistochemistry, including tumour-associated macrophages (TAMs), natural killer cells (NK), tumour-associated neutrophils (TANs), B cells and the ICP V-domain Ig suppressor of T cell activation (VISTA), a potent negative regulator of T cell function [148]. However, no differences were observed in these markers in the mice receiving setanaxib, compared to vehicle (**Figure 60**).

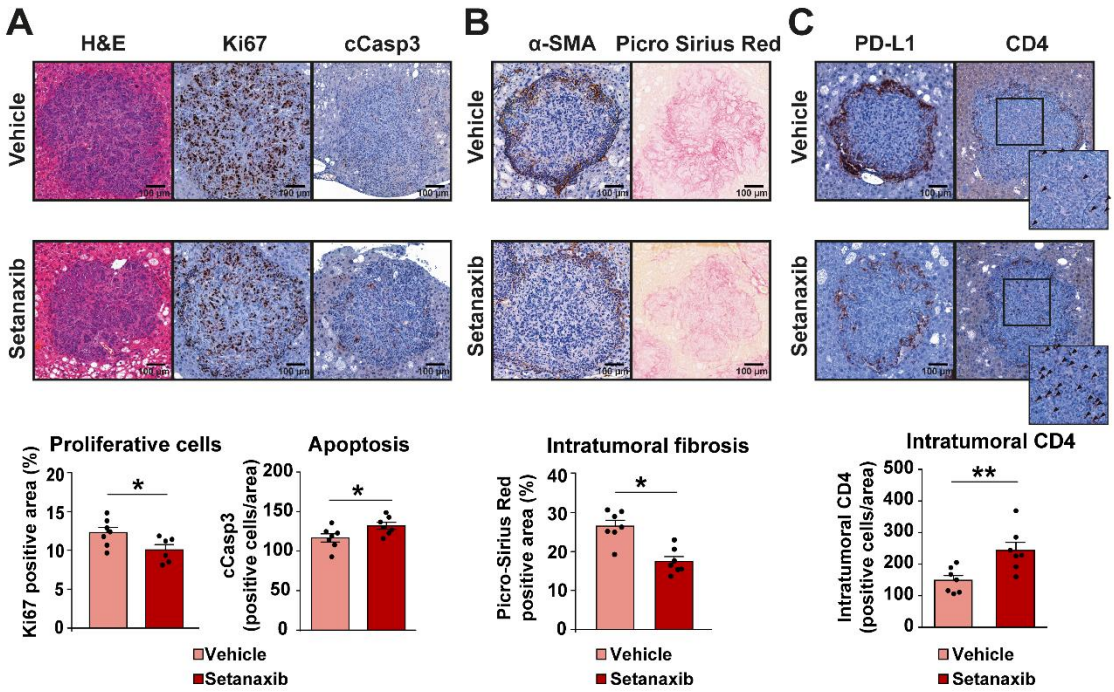

Figure 59. Effects of dual NOX4/NOX1 inhibition with setanaxib on tumour cell growth, CAF hallmarks and immune infiltration *in vivo* in the AKT/YAP mouse intrahepatic cholangiocarcinoma (iCCA) model. CCA tumours were induced using the HTVI AKT-YAP model and treated with setanaxib (60 mg/kg) or the vehicle. **A.** Representative images of haematoxylin-eosin (H&E) and IHCs for Ki67 and cleaved-Caspase 3 (cCap3) (top) and quantification (bottom). **B.** IHC for α-SMA and Picro-Sirius Red staining (top) and quantification (bottom). **C.** IHCs for PD-L1 and CD4 in liver sections from mice treated with vehicle and setanaxib (top) and quantification of CD4 cells (bottom). Arrows indicate CD4 positive cells. Values are expressed as mean ± SEM from 7 animals. *, $p < 0.05$; **, $p < 0.01$; as compared with vehicle group.

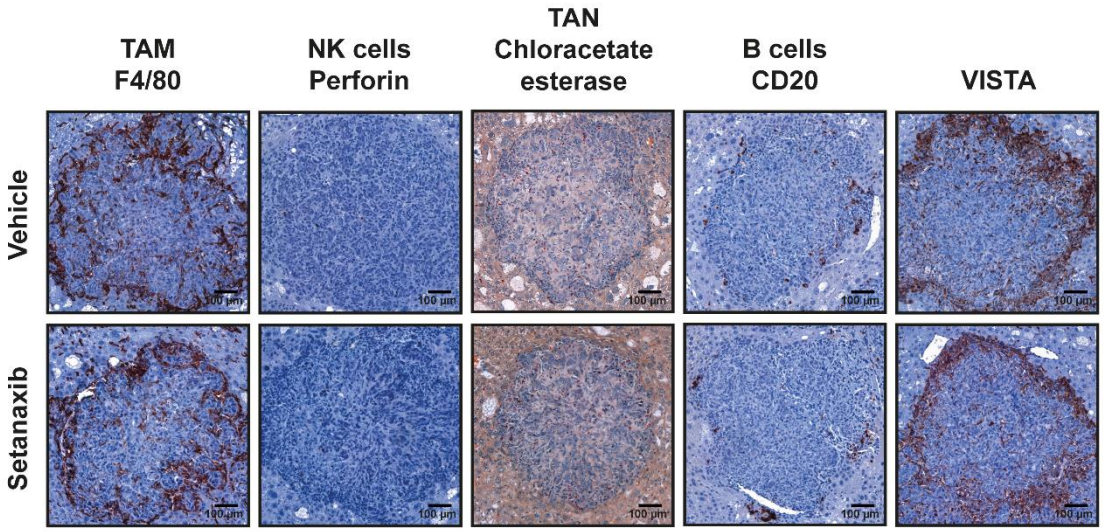

Figure 60. Impact of setanaxib treatment on the immune tumour microenvironment in the AKT-YAP intrahepatic cholangiocarcinoma (iCCA) model. Tumours were induced using the HTVI AKT-YAP model and treated with setanaxib (60 mg/kg) or the vehicle. Representative images of IHC for F4/80, Perforin, Chloroacetate esterase, Cd20 and Vista, specific markers of different populations in the immune tumour compartment. TAM, Tumour associated macrophages; NK, Natural Killer; TAN, Tumour associated Neutrophils; V-domain Ig suppressor of T cell activation, VISTA.

Considering the beneficial effects of setanaxib in a preclinical model of CCA, we wanted to simulate the potential use of setanaxib in CCA patients. In collaboration with Beatriz Martín-Mur (CNAG, Barcelona, Spain) we generated a gene signature corresponding to the genes commonly regulated by setanaxib in the three human HSC cell lines from our RNA-seq data. Interestingly, patients enriched in the setanaxib signature present a longer survival (**Figure 61A**), reduced CD274/PD-L1 expression levels (**Figure 61B**) and an increase in activated CD4 infiltration (**Figure 61C**), as analysed by Sara Hijazo-Pechero (IDIBELL, L'Hospitalet de Llobregat). These data agree with our results in the murine model and provide evidence suggesting that setanaxib might be a good therapeutic candidate in iCCA.

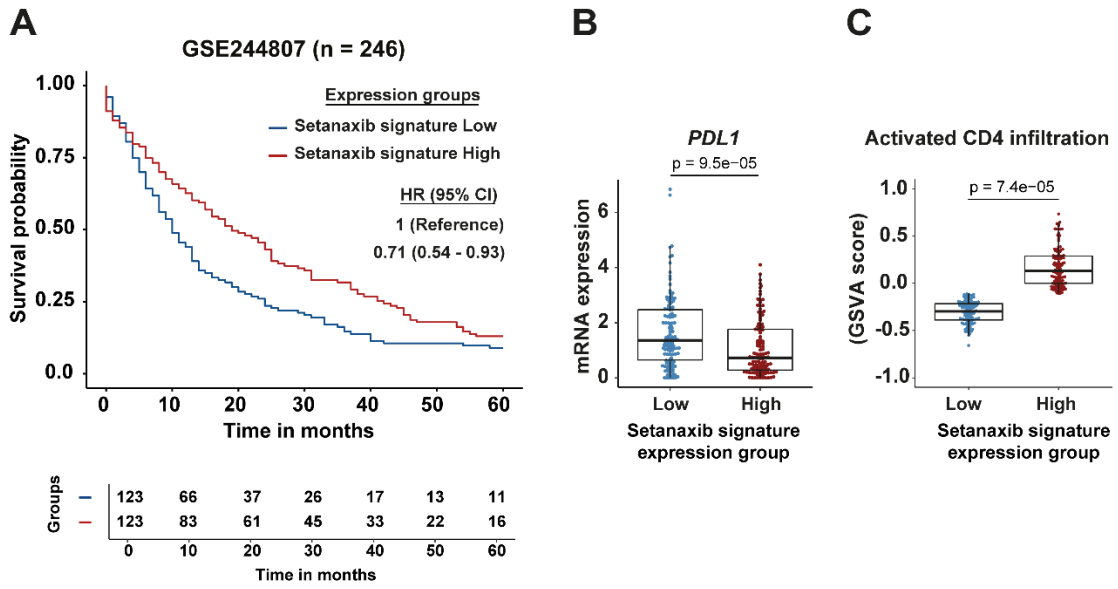

Figure 61. Analysis of survival probability and immune activation in intrahepatic cholangiocarcinoma patients based on the enrichment in a gene signature of genes regulated by setanaxib. We generated a gene signature corresponding to the genes commonly regulated by setanaxib in the three human HSC cell lines from our RNA-seq data. **A.** 5-year survival probability of patients from GSE244807 cohort stratified based on enrichment of the setanaxib gene signature (log-rank test). **B.** CD274/PDL1 expression in patients from GSE244807 cohort stratified as in A. **C.** Activated CD4 infiltration in patients from GSE244807 cohort stratified as in A.

VI. DISCUSSION

1. Iron chelation as a new therapeutic approach to prevent senescence and liver fibrosis progression

Despite extensive knowledge on liver fibrosis mechanisms, antifibrotic therapies in human pathologies have shown modest success [149, 150]. Better refined and more predictive *in vitro* and animal models may hasten drug development [151]. An increasing number of studies on hepatocellular senescence have revealed its importance in liver physiology and pathology [41, 152]. However, the mechanisms that induce the hepatic senescence are yet to be fully explored. Here, we show that senescence occurs in an experimental model of liver fibrosis after chronic treatment with CCl_4, concomitant with iron accumulation and hallmarks of liver fibrosis. These results reveal that not only the pathologies related to MASLD or ALD accumulate iron [64, 66], but it may be also accumulated in cases of chronic damage of the hepatocytes, not related to steatohepatitis.

The treatment with an iron chelator, deferiprone, attenuates iron accumulation and fibrosis, revealing the essential role played by iron in this process. We could speculate that deferiprone might be preventing oxidative damage caused by an accumulated labile iron pool, as was proposed for deferoxamine, an iron chelator, which could have antifibrotic effects in the liver through its antioxidant properties [153, 154]. In this study, we propose that deferiprone prevents liver fibrosis progression by decreasing senescence. Senescent cells are highly secretory, and they execute a diverse set of functions mediated by the SASP [36]. Our results indicate that deferiprone treatment induces notable changes in the composition of SASP in the liver, favoring an anti-inflammatory environment.

The major contributors of senescence properties in the liver are hepatocytes [152], which express almost all the iron-related genes, in accordance with their central role in iron metabolism [155]. Here, we present evidence that hepatocytes from CCl_4-treated mice, or treated *in vitro* with CCl_4, show a gene transcriptomic signature compatible with iron accumulation and SASP, correlating with induction of ROS-related genes, activation of the TGF-β pathway and a decrease in oxidative metabolism, as characteristics of hepatocyte growth arrest, inflammation and senescence [156]. The results in *in vitro* experiments with human hepatocytes have demonstrated that iron accumulates in response to an agent that induces senescence, such as doxorubicin, being deferiprone able to attenuate some senescent-related hallmarks, such as SA-β-GAL staining and the SASP-related gene

expression, overall, clearly indicating that hepatocytes would be a target for iron chelators, which would prevent senescence. Deferiprone also attenuated doxorubicin-mediated cell death but did not completely prevent the arrest in cell cycle, as observed by the levels of CDKN1A (p21), which continued being high, and the cell viability, which continued being decreased, in the combined treatment with doxorubicin and deferiprone. This type of phenotype is typical of treatments that impair the SASP in senescent cells but are not able to completely prevent the arrest in cell cycle. However, this SASP-less phenotype is sufficient to attenuate the microinflammatory involvement that contributes to liver fibrosis and cancer [157, 158].

The use of senolytic agents in liver fibrosis could be beneficial by removing senescent hepatocytes, but action on senescent HSC could be counterproductive due to their less profibrotic phenotype [159]. In this sense, different strategies are ongoing to target senescence specifically in hepatocytes [160]. Here we demonstrate that iron chelators would prevent the deleterious effects of iron accumulation and the progression of senescence specifically in hepatocytes, preventing inflammation and fibrosis. No effect of deferiprone is observed in HSC undergoing senescence by doxorubicin or DCA and it does not affect their expression of ECM-related genes. These results suggest a cell-type-specific response to iron chelation, where hepatocytes appear to be more sensitive to changes in iron levels than HSCs, in line with their role in regulating iron homeostasis. Therefore, it seems that iron chelation efficacy as a therapeutic strategy relies on the effects on decreasing senescence and SASP in hepatocytes, which indirectly affect the fibroblast profibrogenic phenotype *in vivo*, attenuating liver fibrosis.

Altogether, experimental data indicate that iron, which accumulates after chronic liver injury, mediates senescence and liver fibrosis. We also show transcriptomic data in patients with different etiologies (MASH, ASH and alcoholic cirrhosis) demonstrating the relevance of iron accumulation in the progression of liver fibrosis, correlating with a SASP-related gene signature and pivotal hallmarks of hepatocyte damage. Collectively, our study establishes iron accumulation as a clinically exploitable driver of pathological senescence in hepatocytes, which could attenuate liver fibrosis, as was previously proposed in kidney and lung [62].

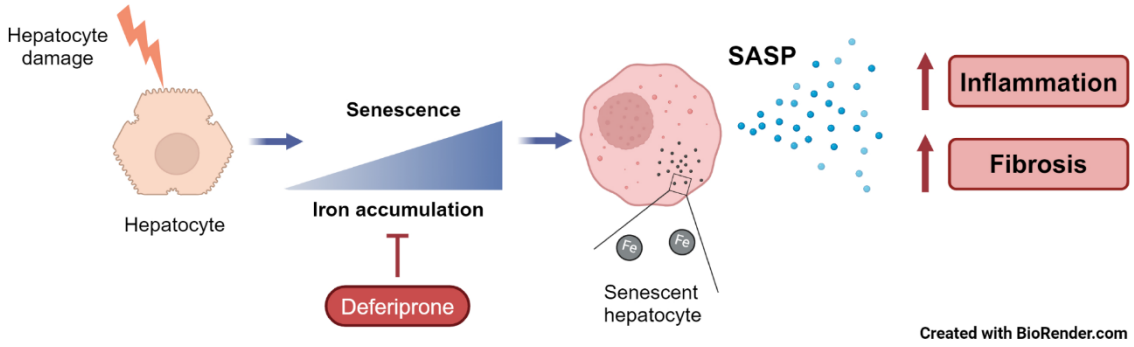

Figure 62. Graphical abstract summarizing the results. Deferiprone prevents iron accumulation and senescence hallmarks, particularly in hepatocytes, which present reduced levels of SASP factors, attenuating inflammation and liver fibrosis. Created with BioRender.com.

2. NOX4/NOX1 dual inhibition in cholangiocarcinoma as an efficient approach to target TGF-beta protumorigenic actions in CAF

TGF-β signalling plays a central role in carcinogenesis by modulating key events both in the tumour cell and the TME. It has been widely reported that in HCC TGF-β can suppress or promote tumour progression depending on the stage of the disease. In general, TGF-β suppresses tumour growth at early stages, while acts as a tumour promoting agent at late stages by inducing invasion and metastasis [30]. In the liver TME, TGF-β is considered to play detrimental roles since it activates CAF, stimulates angiogenesis and exerts immunosuppressive effects [35].

The recent approval of immunotherapy for the treatment of iCCA patients was the first important change in the standard of care for the majority of iCCA patients in decades. However, the high percentage of unresponsive patients to these therapies led strategies towards the combination of immunotherapy with inhibitors of other major signalling pathways exerting immunosuppressor actions. In this context, TGF-β appeared to be an ideal candidate, but the latest clinical trial using TGF-β inhibitors was discontinued, as the trial did not meet its primary end point of improving overall survival [34]. Indeed, we have observed in previous results from the group that TGF-β presents strong tumour suppressing effects on the iCCA tumour cell and signalling inhibition using TGF-β receptor inhibitors promotes CCA tumour growth (unpublished, manuscript under review). On the contrary, inhibiting TGF-β functions in the TME could have therapeutic effects. For instance, inhibiting TGF-β effects on CAF activation could be an interesting strategy in CCA since CAF have been shown to promote tumour growth and therapeutic resistance in this type of cancer [161]. To

bypass the undesired effects of TGF-β inhibitors on the tumour cells we decided to search for downstream mediators of specifically TGF-β protumorigenic actions, and we focused our attention on NOX4, whose expression was found highly increased in iCCA compared to normal tissue.

NOX4 role in the tumour cell has been controversial, being defined as protumorigenic in some tumours [162], and suppressor in others, including HCC [98]. However, nothing was known about NOX4 in iCCA when we started this project. Interestingly, our data reveals that NOX4 expression is absent in the tumour cell and restricted to CAF from the TME in iCCA, which would allow to inhibit it as a therapeutic approach in the fibroblasts without apparent undesired side effects on tumour cells. Nevertheless, while the role of NOX4 in favouring TGF-β fibroblast transdifferentiation has been reported over the years in different pathologies, including several cancers [163-166], a very recent study indicated that NOX4 is dispensable for skin myofibroblast differentiation and wound healing, revealing that there is still controversy in this field [167]. In that report, authors did not find differences between WT and NOX4-/- mice in terms of wound healing. Concretely, primary fibroblasts isolated from mice or from patients with NOX4 mutations were able to get activated after exposure to TGF-β [167]. These previous findings are in agreement with our results showing lack of differences in the stroma from the iCCA syngeneic model and human CRISPR-NOX4 HSC cells that were able to be activated in response to TGF-β.

However, that report did not provide a mechanism by which fibroblasts are able to respond to TGF-β in absence of NOX4, while we demonstrate here that NOX4 and NOX1 act in concert to allow TGF-β-induced transdifferentiation, and that dual inhibition is necessary to impair this process. Concretely, setanaxib was able to specifically target CAF functions and reduce iCCA growth both *in vitro* and *in vivo*. The question that remains open is why some studies found that depletion of NOX4 expression alone in NOX4-/- mice was able to impair fibroblast activation and liver fibrosis development [111]. In this regard, our group has published that NOX4 deletion favours liver regeneration [100]. In accordance with this, it is plausible that NOX4 absence in hepatocytes from knockout animals positively affects the regenerative capacity of the liver upon damage induction and, therefore, the development of liver fibrosis is attenuated. In other studies in different tumour types, such as prostate [168], oesophageal [163] or breast cancers [169], perhaps the levels

and/or function of NOX1 or the components of its regulatory complex (i.e. p22phox) are different and insufficient to trigger a compensatory mechanism after NOX4 depletion. Further investigation of these mechanisms is necessary to resolve this question.

Importantly, setanaxib recently reached the clinical stage. In a clinical trial performed in patients with primary biliary cholangitis (PBC) (NCT03226067), setanaxib showed evidence for potential anti-cholestatic and anti-fibrotic effects [146], which led to further examination of setanaxib activity in a new clinical trial in PBC patients with elevated liver stiffness (NCT05014672). Furthermore, setanaxib is also being tested together with immunotherapy in patients with recurrent or metastatic squamous cell carcinoma of head and neck (NCT05323656). Interestingly, preliminary transcriptomic data from this trial showed that the two top pathways altered by setanaxib were the “Idiopathic Pulmonary Fibrosis Signaling Pathway” and “Hepatic Fibrosis/Hepatic Stellate Cell Activation Pathway”, supporting the potential of setanaxib as an anti-fibrotic agent also in cancer. Indeed, we described here how setanaxib was able to reduce iCCA tumour growth, but also intratumoral fibrosis, correlating with the fact that NOX4 is mainly concentrated in myCAF, producers of ECM. Intriguingly, there is a proportion of NOX4 expression in apCAF, which have recently been involved in immunosuppression in pancreatic cancer [170]. In this sense, we also observed a reduction of PD-L1 expression concomitant with lower α-SMA staining at the border of iCCA tumours from the setanaxib group, compared to vehicle group. A recent report described that PD-L1 is expressed in HSC, and it is inducible by TGF-β [171]. Furthermore, PD-L1 expression was able to control HSC activation by regulating TGF-β signalling, which impacted the ability of HSC to communicate with iCCA tumour cells by paracrine signaling, reducing tumour growth [171]. This suggests that setanaxib reduction of PD-L1 expression may impact tumour growth independently of its role in the immune system regulation. Nevertheless, we also observed an increase in CD4 T cell infiltration in the setanaxib group, which is probably facilitated by the reduction of intratumoral fibrosis, as it has been previously shown [147]. Importantly, another recent study correlated intratumoral CD4 T cell infiltration with better survival of iCCA patients [172]. In this sense, our simulation of iCCA stratification based on the setanaxib signature obtained in HSC *in vitro* rendered similar results of PD-L1 reduction and increased CD4 infiltration accompanied with an improved survival of iCCA patients. Nevertheless, further studies are needed to better characterize the

importance of this infiltration and the potential impact of the different subpopulations of CD4 T cells, which have been shown to have different roles and impact in patient survival [173]. Altogether, these data suggest a potential bright future for dual NOX4/NOX1 inhibitors as therapeutic molecules.

VII. CONCLUSIONS

1. Iron accumulates in the liver after chronic liver injury by CCl4, mediating senescence and fibrosis in mice.

2. Deferiprone attenuates iron accumulation, fibrosis and senescence in a model of CCl4-induced liver fibrosis in mice and induces a switch towards a secretory profile of anti-inflammatory cytokines.

3. Iron chelation by deferiprone prevents the senescence progression and SASP in hepatocytes, but not in HSC.

4. Iron accumulation is a relevant factor in liver fibrosis patients, correlating with SASP-related gene signatures and hallmarks of fibrosis.

5. NOX4 expression is upregulated in CCA, specifically in CAF, correlating with myofibroblast hallmarks.

6. Stable genetic loss of NOX4 expression does not impair HSC transdifferentiation into myofibroblasts or CAFs.

7. Dual inhibition or silencing of NOX4/NOX1 is required to attenuate the transdifferentiation into myofibroblasts induced by TGF-β in vitro.

8. The dual NOX1/NOX4 inhibitor setanaxib reduces tumour burden, CAF functions and regulates immune landscape in a mouse model of CCA, suggesting a potential therapeutic effect.

VIII. REFERENCES

1. Bataller, R. and D.A. Brenner, *Liver fibrosis*. J Clin Invest, 2005. **115**(2): p. 209-18.

2. Pellicoro, A., et al., *Liver fibrosis and repair: immune regulation of wound healing in a solid organ*. Nat Rev Immunol, 2014. **14**(3): p. 181-94.

3. Zamani, M., et al., *Global prevalence of advanced liver fibrosis and cirrhosis in the general population: a systematic review and meta-analysis*. Clin Gastroenterol Hepatol, 2024.

4. Petta, S., et al., *The first MASH drug therapy on the horizon: Current perspectives of resmetirom*. Liver Int, 2024. **44**(7): p. 1526-1536.

5. Marcellin, P., et al., *Regression of cirrhosis during treatment with tenofovir disoproxil fumarate for chronic hepatitis B: a 5-year open-label follow-up study*. Lancet, 2013. **381**(9865): p. 468-75.

6. D'Ambrosio, R., et al., *A morphometric and immunohistochemical study to assess the benefit of a sustained virological response in hepatitis C virus patients with cirrhosis*. Hepatology, 2012. **56**(2): p. 532-43.

7. Vilar-Gomez, E., et al., *Weight Loss Through Lifestyle Modification Significantly Reduces Features of Nonalcoholic Steatohepatitis*. Gastroenterology, 2015. **149**(2): p. 367-78 e5; quiz e14-5.

8. Lassailly, G., et al., *Bariatric Surgery Reduces Features of Nonalcoholic Steatohepatitis in Morbidly Obese Patients*. Gastroenterology, 2015. **149**(2): p. 379-88; quiz e15-6.

9. Kamm, D.R. and K.S. McCommis, *Hepatic stellate cells in physiology and pathology*. J Physiol, 2022. **600**(8): p. 1825-1837.

10. Mederacke, I., et al., *Fate tracing reveals hepatic stellate cells as dominant contributors to liver fibrosis independent of its aetiology*. Nat Commun, 2013. **4**: p. 2823.

11. Drabsch, Y. and P. ten Dijke, *TGF-beta signalling and its role in cancer progression and metastasis*. Cancer Metastasis Rev, 2012. **31**(3-4): p. 553-68.

12. Xu, F., et al., *TGF-beta/SMAD Pathway and Its Regulation in Hepatic Fibrosis*. J Histochem Cytochem, 2016. **64**(3): p. 157-67.

13. Kisseleva, T., et al., *Myofibroblasts revert to an inactive phenotype during regression of liver fibrosis*. Proc Natl Acad Sci U S A, 2012. **109**(24): p. 9448-53.

14. Troeger, J.S., et al., *Deactivation of hepatic stellate cells during liver fibrosis resolution in mice*. Gastroenterology, 2012. **143**(4): p. 1073-83 e22.

15. Blechacz, B., et al., *Clinical diagnosis and staging of cholangiocarcinoma*. Nat Rev Gastroenterol Hepatol, 2011. **8**(9): p. 512-22.

16. Kendall, T., et al., *Anatomical, histomorphological and molecular classification of cholangiocarcinoma*. Liver Int, 2019. **39 Suppl 1**: p. 7-18.

17. Banales, J.M., et al., *Cholangiocarcinoma 2020: the next horizon in mechanisms and management*. Nat Rev Gastroenterol Hepatol, 2020. **17**(9): p. 557-588.

18. Vithayathil, M. and S.A. Khan, *Current epidemiology of cholangiocarcinoma in Western countries*. J Hepatol, 2022. **77**(6): p. 1690-1698.

19. Oh, D.Y., et al., *Plain language summary of the TOPAZ-1 study: durvalumab and chemotherapy for advanced biliary tract cancer*. Future Oncol, 2023. **19**(34): p. 2277-2289.

20. Rimini, M., et al., *Durvalumab plus gemcitabine and cisplatin in advanced biliary tract cancer: An early exploratory analysis of real-world data*. Liver Int, 2023. **43**(8): p. 1803-1812.

21. Kelley, R.K., et al., *Pembrolizumab in combination with gemcitabine and cisplatin compared with gemcitabine and cisplatin alone for patients with advanced biliary tract cancer (KEYNOTE-966): a randomised, double-blind, placebo-controlled, phase 3 trial*. Lancet, 2023. **401**(10391): p. 1853-1865.

22. Banales, J.M., et al., *Expert consensus document: Cholangiocarcinoma: current knowledge and future perspectives consensus statement from the European Network for the Study of Cholangiocarcinoma (ENS-CCA)*. Nat Rev Gastroenterol Hepatol, 2016. **13**(5): p. 261-80.

23. Ilyas, S.I., et al., *Cholangiocarcinoma - evolving concepts and therapeutic strategies*. Nat Rev Clin Oncol, 2018. **15**(2): p. 95-111.

24. Cadamuro, M., et al., *The deleterious interplay between tumor epithelia and stroma in cholangiocarcinoma*. Biochim Biophys Acta Mol Basis Dis, 2018. **1864**(4 Pt B): p. 1435-1443.

25. Mertens, J.C., et al., *Therapeutic effects of deleting cancer-associated fibroblasts in cholangiocarcinoma*. Cancer Res, 2013. **73**(2): p. 897-907.

26. Greten, T.F., et al., *Immunology and immunotherapy of cholangiocarcinoma*. Nat Rev Gastroenterol Hepatol, 2023. **20**(6): p. 349-365.

27. Ilyas, S.I., et al., *Cholangiocarcinoma - novel biological insights and therapeutic strategies*. Nat Rev Clin Oncol, 2023. **20**(7): p. 470-486.

28. Cantallops Vila, P., et al., *Heterogeneity, crosstalk, and targeting of cancer-associated fibroblasts in cholangiocarcinoma*. Hepatology, 2024. **79**(4): p. 941-958.

29. Affo, S., et al., *Promotion of cholangiocarcinoma growth by diverse cancer-associated fibroblast subpopulations*. Cancer Cell, 2021. **39**(6): p. 883.

30. Massague, J. and D. Sheppard, *TGF-beta signaling in health and disease*. Cell, 2023. **186**(19): p. 4007-4037.

31. Papoutsoglou, P., C. Louis, and C. Coulouarn, *Transforming Growth Factor-Beta (TGFbeta) Signaling Pathway in Cholangiocarcinoma*. Cells, 2019. **8**(9).

32. Vaquero, J., et al., *Epithelial-mesenchymal transition in cholangiocarcinoma: From clinical evidence to regulatory networks*. J Hepatol, 2017. **66**(2): p. 424-441.

33. Lin, Y., et al., *JNK inhibitor SP600125 enhances TGF-beta-induced apoptosis of RBE human cholangiocarcinoma cells in a Smad-dependent manner*. Mol Med Rep, 2013. **8**(6): p. 1623-9.

34. Skouteris, N., et al., *Immune checkpoint inhibitors and combinations with other agents in cholangiocarcinoma*. Immunotherapy, 2023. **15**(7): p. 487-502.

35. Gonzalez-Sanchez, E., et al., *The TGF-beta Pathway: A Pharmacological Target in Hepatocellular Carcinoma?* Cancers (Basel), 2021. **13**(13).

36. Birch, J. and J. Gil, *Senescence and the SASP: many therapeutic avenues*. Genes Dev, 2020. **34**(23-24): p. 1565-1576.

37. Gorgoulis, V., et al., *Cellular Senescence: Defining a Path Forward*. Cell, 2019. **179**(4): p. 813-827.

38. Kuilman, T., et al., *Oncogene-induced senescence relayed by an interleukin-dependent inflammatory network*. Cell, 2008. **133**(6): p. 1019-31.

39. Lujambio, A., et al., *Non-cell-autonomous tumor suppression by p53*. Cell, 2013. **153**(2): p. 449-60.

40. Munoz-Espin, D. and M. Serrano, *Cellular senescence: from physiology to pathology*. Nat Rev Mol Cell Biol, 2014. **15**(7): p. 482-96.

41. Ferreira-Gonzalez, S., et al., *Cellular Senescence in Liver Disease and Regeneration*. Semin Liver Dis, 2021. **41**(1): p. 50-66.

42. Aravinthan, A., et al., *Hepatocyte expression of the senescence marker p21 is linked to fibrosis and an adverse liver-related outcome in alcohol-related liver disease*. PLoS One, 2013. **8**(9): p. e72904.

43. Marshall, A., et al., *Relation between hepatocyte G1 arrest, impaired hepatic regeneration, and fibrosis in chronic hepatitis C virus infection*. Gastroenterology, 2005. **128**(1): p. 33-42.

44. Tachtatzis, P.M., et al., *Chronic Hepatitis B Virus Infection: The Relation between Hepatitis B Antigen Expression, Telomere Length, Senescence, Inflammation and Fibrosis*. PLoS One, 2015. **10**(5): p. e0127511.

45. Aravinthan, A., et al., *Hepatocyte senescence predicts progression in non-alcohol-related fatty liver disease*. J Hepatol, 2013. **58**(3): p. 549-56.

46. Wijayasiri, P., et al., *Role of Hepatocyte Senescence in the Activation of Hepatic Stellate Cells and Liver Fibrosis Progression*. Cells, 2022. **11**(14): p. 2221.

47. Yu, H., et al., *Lipid accumulation-induced hepatocyte senescence regulates the activation of hepatic stellate cells through the Nrf2-antioxidant response element pathway*. Exp Cell Res, 2021. **405**(2): p. 112689.

48. Bird, T.G., et al., *TGFbeta inhibition restores a regenerative response in acute liver injury by suppressing paracrine senescence*. Sci Transl Med, 2018. **10**(454): p. eaan1230.

49. Ritschka, B., et al., *The senotherapeutic drug ABT-737 disrupts aberrant p21 expression to restore liver regeneration in adult mice*. Genes Dev, 2020. **34**(7-8): p. 489-494.

50. Irvine, K.M., et al., *Senescent human hepatocytes express a unique secretory phenotype and promote macrophage migration*. World J Gastroenterol, 2014. **20**(47): p. 17851-62.

51. Ogrodnik, M., et al., *Cellular senescence drives age-dependent hepatic steatosis*. Nat Commun, 2017. **8**: p. 15691.

52. Kisseleva, T. and D. Brenner, *Molecular and cellular mechanisms of liver fibrosis and its regression*. Nat Rev Gastroenterol Hepatol, 2021. **18**(3): p. 151-166.

53. Krizhanovsky, V., et al., *Senescence of activated stellate cells limits liver fibrosis*. Cell, 2008. **134**(4): p. 657-67.

54. Kong, X., et al., *Interleukin-22 induces hepatic stellate cell senescence and restricts liver fibrosis in mice*. Hepatology, 2012. **56**(3): p. 1150-9.

55. Kawabata, H., *Transferrin and transferrin receptors update*. Free Radic Biol Med, 2019. **133**: p. 46-54.

56. Sharp, P. and S.K. Srai, *Molecular mechanisms involved in intestinal iron absorption*. World J Gastroenterol, 2007. **13**(35): p. 4716-24.

57. Brasse-Lagnel, C., et al., *Intestinal DMT1 cotransporter is down-regulated by hepcidin via proteasome internalization and degradation*. Gastroenterology, 2011. **140**(4): p. 1261-1271 e1.

58. Galaris, D., A. Barbouti, and K. Pantopoulos, *Iron homeostasis and oxidative stress: An intimate relationship*. Biochim Biophys Acta Mol Cell Res, 2019. **1866**(12): p. 118535.

59. Evans, R.W., et al., *Nature of non-transferrin-bound iron: studies on iron citrate complexes and thalassemic sera*. J Biol Inorg Chem, 2008. **13**(1): p. 57-74.

60. Hider, R.C. and X.L. Kong, *Glutathione: a key component of the cytoplasmic labile iron pool*. Biometals, 2011. **24**(6): p. 1179-87.

61. Hider, R.C., *Nature of nontransferrin-bound iron*. Eur J Clin Invest, 2002. **32 Suppl 1**: p. 50-4.

62. Maus, M., et al., *Iron accumulation drives fibrosis, senescence and the senescence-associated secretory phenotype*. Nat Metab, 2023. **5**(12): p. 2111-2130.

63. Wood, M.J., et al., *Ductular reaction in hereditary hemochromatosis: the link between hepatocyte senescence and fibrosis progression*. Hepatology, 2014. **59**(3): p. 848-57.

64. Ali, N., K. Ferrao, and K.J. Mehta, *Liver Iron Loading in Alcohol-Associated Liver Disease*. Am J Pathol, 2023. **193**(10): p. 1427-1439.

65. Czaja, A.J., *Review article: iron disturbances in chronic liver diseases other than haemochromatosis - pathogenic, prognostic, and therapeutic implications*. Aliment Pharmacol Ther, 2019. **49**(6): p. 681-701.

66. Dongiovanni, P., et al., *Iron in fatty liver and in the metabolic syndrome: a promising therapeutic target*. J Hepatol, 2011. **55**(4): p. 920-32.

67. Bedard, K., B. Lardy, and K.H. Krause, *NOX family NADPH oxidases: not just in mammals*. Biochimie, 2007. **89**(9): p. 1107-12.

68. Hajjar, C., et al., *The NOX Family of Proteins Is Also Present in Bacteria*. mBio, 2017. **8**(6).

69. Bedard, K. and K.H. Krause, *The NOX family of ROS-generating NADPH oxidases: physiology and pathophysiology*. Physiol Rev, 2007. **87**(1): p. 245-313.

70. Kato, K. and L. Hecker, *NADPH oxidases: Pathophysiology and therapeutic potential in age-associated pulmonary fibrosis*. Redox Biol, 2020. **33**: p. 101541.

71. Schroder, K., *NADPH oxidases: Current aspects and tools*. Redox Biol, 2020. **34**: p. 101512.

72. Schroder, K., N. Weissmann, and R.P. Brandes, *Organizers and activators: Cytosolic Nox proteins impacting on vascular function*. Free Radic Biol Med, 2017. **109**: p. 22-32.

73. Cheng, G., D. Ritsick, and J.D. Lambeth, *Nox3 regulation by NOXO1, p47phox, and p67phox*. J Biol Chem, 2004. **279**(33): p. 34250-5.

74. Debbabi, M., et al., *NOXO1 phosphorylation on serine 154 is critical for optimal NADPH oxidase 1 assembly and activation*. FASEB J, 2013. **27**(4): p. 1733-48.

75. Yamamoto, A., et al., *Phosphorylation of Noxo1 at threonine 341 regulates its interaction with Noxa1 and the superoxide-producing activity of Nox1*. FEBS J, 2013. **280**(20): p. 5145-59.

76. Wientjes, F.B., et al., *p40phox, a third cytosolic component of the activation complex of the NADPH oxidase to contain src homology 3 domains*. Biochem J, 1993. **296 (Pt 3)**(Pt 3): p. 557-61.

77. De Deken, X., et al., *Roles of DUOX-mediated hydrogen peroxide in metabolism, host defense, and signaling*. Antioxid Redox Signal, 2014. **20**(17): p. 2776-93.

78. Prior, K.K., et al., *CRISPR/Cas9-mediated knockout of p22phox leads to loss of Nox1 and Nox4, but not Nox5 activity*. Redox Biol, 2016. **9**: p. 287-295.

79. Serrander, L., et al., *NOX4 activity is determined by mRNA levels and reveals a unique pattern of ROS generation*. Biochem J, 2007. **406**(1): p. 105-14.

80. Park, H.S., et al., *Cutting edge: direct interaction of TLR4 with NAD(P)H oxidase 4 isozyme is essential for lipopolysaccharide-induced production of reactive oxygen species and activation of NF-kappa B*. J Immunol, 2004. **173**(6): p. 3589-93.

81. Gorin, Y., et al., *Nox4 mediates angiotensin II-induced activation of Akt/protein kinase B in mesangial cells*. Am J Physiol Renal Physiol, 2003. **285**(2): p. F219-29.

82. Inoguchi, T., et al., *Protein kinase C-dependent increase in reactive oxygen species (ROS) production in vascular tissues of diabetes: role of vascular NAD(P)H oxidase*. J Am Soc Nephrol, 2003. **14**(8 Suppl 3): p. S227-32.

83. Matsushima, S., et al., *Tyrosine kinase FYN negatively regulates NOX4 in cardiac remodeling*. J Clin Invest, 2016. **126**(9): p. 3403-16.

84. Gil Lorenzo, A.F., et al., *Heat Shock Protein 70 and CHIP Promote Nox4 Ubiquitination and Degradation within the Losartan Antioxidative Effect in Proximal Tubule Cells*. Cell Physiol Biochem, 2015. **36**(6): p. 2183-97.

85. Takac, I., et al., *The E-loop is involved in hydrogen peroxide formation by the NADPH oxidase Nox4*. J Biol Chem, 2011. **286**(15): p. 13304-13.

86. Vermot, A., et al., *NADPH Oxidases (NOX): An Overview from Discovery, Molecular Mechanisms to Physiology and Pathology*. Antioxidants (Basel), 2021. **10**(6).

87. Zana, M., et al., *Interaction between p22(phox) and Nox4 in the endoplasmic reticulum suggests a unique mechanism of NADPH oxidase complex formation*. Free Radic Biol Med, 2018. **116**: p. 41-49.

88. Block, K., Y. Gorin, and H.E. Abboud, *Subcellular localization of Nox4 and regulation in diabetes*. Proc Natl Acad Sci U S A, 2009. **106**(34): p. 14385-90.

89. Hilenski, L.L., et al., *Distinct subcellular localizations of Nox1 and Nox4 in vascular smooth muscle cells*. Arterioscler Thromb Vasc Biol, 2004. **24**(4): p. 677-83.

90. Goyal, P., et al., *Identification of novel Nox4 splice variants with impact on ROS levels in A549 cells*. Biochem Biophys Res Commun, 2005. **329**(1): p. 32-9.

91. Waghela, B.N., et al., *Molecular insights of NADPH oxidases and its pathological consequences*. Cell Biochem Funct, 2021. **39**(2): p. 218-234.

92. Moreno-Caceres, J., et al., *Caveolin-1-dependent activation of the metalloprotease TACE/ADAM17 by TGF-beta in hepatocytes requires activation of Src and the NADPH oxidase NOX1*. FEBS J, 2016. **283**(7): p. 1300-10.

93. Ikeda, S., et al., *IQGAP1 regulates reactive oxygen species-dependent endothelial cell migration through interacting with Nox2*. Arterioscler Thromb Vasc Biol, 2005. **25**(11): p. 2295-300.

94. Liang, S., et al., *NADPH Oxidase 1 in Liver Macrophages Promotes Inflammation and Tumor Development in Mice*. Gastroenterology, 2019. **156**(4): p. 1156-1172 e6.

95. Teufelhofer, O., et al., *Superoxide generation from Kupffer cells contributes to hepatocarcinogenesis: studies on NADPH oxidase knockout mice*. Carcinogenesis, 2005. **26**(2): p. 319-29.

96. Bertram, K., et al., *NOX1 supports the metabolic remodeling of HepG2 cells*. PLoS One, 2015. **10**(3): p. e0122002.

97. Penuelas-Haro, I., et al., *The NADPH oxidase NOX4 regulates redox and metabolic homeostasis preventing HCC progression*. Hepatology, 2023. **78**(2): p. 416-433.

98. Crosas-Molist, E., et al., *The NADPH oxidase NOX4 inhibits hepatocyte proliferation and liver cancer progression*. Free Radic Biol Med, 2014. **69**: p. 338-47.

99. Carmona-Cuenca, I., et al., *Upregulation of the NADPH oxidase NOX4 by TGF-beta in hepatocytes is required for its pro-apoptotic activity*. J Hepatol, 2008. **49**(6): p. 965-76.

100. Herranz-Iturbide, M., et al., *NADPH oxidase 4 (Nox4) deletion accelerates liver regeneration in mice*. Redox Biol, 2021. **40**: p. 101841.

101. Caja, L., et al., *Overactivation of the MEK/ERK pathway in liver tumor cells confers resistance to TGF-beta-induced cell death through impairing up-regulation of the NADPH oxidase NOX4*. Cancer Res, 2009. **69**(19): p. 7595-602.

102. Espinosa-Sotelo, R., et al., *Dissecting the role of the NADPH oxidase NOX4 in TGF-beta signaling in hepatocellular carcinoma*. Redox Biol, 2023. **65**: p. 102818.

103. Hecker, L., et al., *NADPH oxidase-4 mediates myofibroblast activation and fibrogenic responses to lung injury*. Nat Med, 2009. **15**(9): p. 1077-81.

104. Bondi, C.D., et al., *NAD(P)H oxidase mediates TGF-beta1-induced activation of kidney myofibroblasts*. J Am Soc Nephrol, 2010. **21**(1): p. 93-102.

105. Cucoranu, I., et al., *NAD(P)H oxidase 4 mediates transforming growth factor-beta1-induced differentiation of cardiac fibroblasts into myofibroblasts*. Circ Res, 2005. **97**(9): p. 900-7.

106. Sampson, N., et al., *ROS signaling by NOX4 drives fibroblast-to-myofibroblast differentiation in the diseased prostatic stroma*. Mol Endocrinol, 2011. **25**(3): p. 503-15.

107. Jiang, J.X., et al., *Liver fibrosis and hepatocyte apoptosis are attenuated by GKT137831, a novel NOX4/NOX1 inhibitor in vivo*. Free Radic Biol Med, 2012. **53**(2): p. 289-96.

108. Sancho, P., et al., *NADPH oxidase NOX4 mediates stellate cell activation and hepatocyte cell death during liver fibrosis development*. PLoS One, 2012. **7**(9): p. e45285.

109. Bettaieb, A., et al., *Hepatocyte Nicotinamide Adenine Dinucleotide Phosphate Reduced Oxidase 4 Regulates Stress Signaling, Fibrosis, and Insulin Sensitivity During Development of Steatohepatitis in Mice*. Gastroenterology, 2015. **149**(2): p. 468-80 e10.

110. Cui, W., et al., *NOX1/nicotinamide adenine dinucleotide phosphate, reduced form (NADPH) oxidase promotes proliferation of stellate cells and aggravates liver fibrosis induced by bile duct ligation*. Hepatology, 2011. **54**(3): p. 949-58.

111. Lan, T., T. Kisseleva, and D.A. Brenner, *Deficiency of NOX1 or NOX4 Prevents Liver Inflammation and Fibrosis in Mice through Inhibition of Hepatic Stellate Cell Activation*. PLoS One, 2015. **10**(7): p. e0129743.

112. Jiang, J.X., et al., *Reduced nicotinamide adenine dinucleotide phosphate oxidase 2 plays a key role in stellate cell activation and liver fibrogenesis in vivo*. Gastroenterology, 2010. **139**(4): p. 1375-84.

113. Herranz-Iturbide, M., et al., *The TGF-beta/NADPH Oxidases Axis in the Regulation of Liver Cell Biology in Health and Disease*. Cells, 2021. **10**(9).

114. Tang, W., et al., *Responses of nontransformed human hepatocytes to conditional expression of full-length hepatitis C virus open reading frame*. Am J Pathol, 2007. **171**(6): p. 1831-46.

115. Tsuchida, T. and S.L. Friedman, *Mechanisms of hepatic stellate cell activation*. Nat Rev Gastroenterol Hepatol, 2017. **14**(7): p. 397-411.

116. Carnesecchi, S., et al., *A key role for NOX4 in epithelial cell death during development of lung fibrosis*. Antioxid Redox Signal, 2011. **15**(3): p. 607-19.

117. Rizvi, S., et al., *YAP-associated chromosomal instability and cholangiocarcinoma in mice*. Oncotarget, 2018. **9**(5): p. 5892-5905.

118. Chen, X. and D.F. Calvisi, *Hydrodynamic transfection for generation of novel mouse models for liver cancer research*. Am J Pathol, 2014. **184**(4): p. 912-923.

119. Kamimura, K., et al., *Image-Guided Hydrodynamic Gene Delivery: Current Status and Future Directions*. Pharmaceutics, 2015. **7**(3): p. 213-23.

120. Kao, C.Y., V.M. Factor, and S.S. Thorgeirsson, *Reduced growth capacity of hepatocytes from c-myc and c-myc/TGF-alpha transgenic mice in primary culture*. Biochem Biophys Res Commun, 1996. **222**(1): p. 64-70.

121. Dobin, A., et al., *STAR: ultrafast universal RNA-seq aligner*. Bioinformatics, 2013. **29**(1): p. 15-21.

122. Li, B. and C.N. Dewey, *RSEM: accurate transcript quantification from RNA-Seq data with or without a reference genome*. BMC Bioinformatics, 2011. **12**: p. 323.

123. Korotkevich, G., et al., *Fast gene set enrichment analysis*. bioRxiv, 2021: p. 060012.

124. Yang, W., et al., *Single-Cell Transcriptomic Analysis Reveals a Hepatic Stellate Cell-Activation Roadmap and Myofibroblast Origin During Liver Fibrosis in Mice*. Hepatology, 2021. **74**(5): p. 2774-2790.

125. Godoy, P., et al., *Gene network activity in cultivated primary hepatocytes is highly similar to diseased mammalian liver tissue*. Arch Toxicol, 2016. **90**(10): p. 2513-29.

126. Irizarry, R.A., et al., *Exploration, normalization, and summaries of high density oligonucleotide array probe level data*. Biostatistics, 2003. **4**(2): p. 249-64.

127. Hammad, S., et al., *Tolerance of repeated toxic injuries of murine livers is associated with steatosis and inflammation*. Cell Death Dis, 2023. **14**(7): p. 414.

128. Fujiwara, N., et al., *Molecular signatures of long-term hepatocellular carcinoma risk in nonalcoholic fatty liver disease*. Sci Transl Med, 2022. **14**(650): p. eabo4474.

129. Trepo, E., et al., *Combination of Gene Expression Signature and Model for End-Stage Liver Disease Score Predicts Survival of Patients With Severe Alcoholic Hepatitis*. Gastroenterology, 2018. **154**(4): p. 965-975.

130. Liberzon, A., et al., *The Molecular Signatures Database (MSigDB) hallmark gene set collection*. Cell Syst, 2015. **1**(6): p. 417-425.

131. Hanzelmann, S., R. Castelo, and J. Guinney, *GSVA: gene set variation analysis for microarray and RNA-seq data*. BMC Bioinformatics, 2013. **14**: p. 7.

132. R Core Team. *R: A language and environment for statistical computing*. 2021; Available from: https://www.R-project.org/.

133. Tang, Z., et al., *GEPIA: a web server for cancer and normal gene expression profiling and interactive analyses*. Nucleic Acids Res, 2017. **45**(W1): p. W98-W102.

134. Cerami, E., et al., *The cBio cancer genomics portal: an open platform for exploring multidimensional cancer genomics data*. Cancer Discov, 2012. **2**(5): p. 401-4.

135. Gao, J., et al., *Integrative analysis of complex cancer genomics and clinical profiles using the cBioPortal*. Sci Signal, 2013. **6**(269): p. pl1.

136. Beaufrère, A., et al., *Self-supervised learning to predict intrahepatic cholangiocarcinoma transcriptomic classes on routine histology*. bioRxiv, 2024: p. 2024.01.15.575652.

137. Charoentong, P., et al., *Pan-cancer Immunogenomic Analyses Reveal Genotype-Immunophenotype Relationships and Predictors of Response to Checkpoint Blockade*. Cell Rep, 2017. **18**(1): p. 248-262.

138. Saul, D., et al., *A new gene set identifies senescent cells and predicts senescence-associated pathways across tissues*. Nat Commun, 2022. **13**(1): p. 4827.

139. Kurt, A.S., et al., *IL-2 availability regulates the tissue specific phenotype of murine intra-hepatic Tregs*. Front Immunol, 2022. **13**: p. 1040031.

140. Pommier, Y., et al., *DNA topoisomerases and their poisoning by anticancer and antibacterial drugs*. Chem Biol, 2010. **17**(5): p. 421-33.

141. Sliwinska, M.A., et al., *Induction of senescence with doxorubicin leads to increased genomic instability of HCT116 cells*. Mech Ageing Dev, 2009. **130**(1-2): p. 24-32.

142. Jiang, X., B.R. Stockwell, and M. Conrad, *Ferroptosis: mechanisms, biology and role in disease*. Nat Rev Mol Cell Biol, 2021. **22**(4): p. 266-282.

143. Li, J., et al., *Ferroptosis: past, present and future*. Cell Death Dis, 2020. **11**(2): p. 88.

144. Nguyen, P.T., et al., *Senescent hepatic stellate cells caused by deoxycholic acid modulates malignant behavior of hepatocellular carcinoma*. J Cancer Res Clin Oncol, 2020. **146**(12): p. 3255-3268.

145. Sia, D., et al., *Integrative molecular analysis of intrahepatic cholangiocarcinoma reveals 2 classes that have different outcomes*. Gastroenterology, 2013. **144**(4): p. 829-40.

146. Invernizzi, P., et al., *Setanaxib, a first-in-class selective NADPH oxidase 1/4 inhibitor for primary biliary cholangitis: A randomized, placebo-controlled, phase 2 trial*. Liver Int, 2023. **43**(7): p. 1507-1522.

147. Nicolas-Boluda, A., et al., *Tumor stiffening reversion through collagen crosslinking inhibition improves T cell migration and anti-PD-1 treatment*. Elife, 2021. **10**.

148. Lines, J.L., et al., *VISTA is an immune checkpoint molecule for human T cells*. Cancer Res, 2014. **74**(7): p. 1924-32.

149. Lemoinne, S. and S.L. Friedman, *New and emerging anti-fibrotic therapeutics entering or already in clinical trials in chronic liver diseases*. Curr Opin Pharmacol, 2019. **49**: p. 60-70.

150. Mohammed, O.S., et al., *Current investigations for liver fibrosis treatment: between repurposing the FDA-approved drugs and the other emerging approaches*. J Pharm Pharm Sci, 2023. **26**: p. 11808.

151. Friedman, S.L. and M. Pinzani, *Hepatic fibrosis 2022: Unmet needs and a blueprint for the future*. Hepatology, 2022. **75**(2): p. 473-488.

152. Sanfeliu-Redondo, D., A. Gibert-Ramos, and J. Gracia-Sancho, *Cell senescence in liver diseases: pathological mechanism and theranostic opportunity*. Nat Rev Gastroenterol Hepatol, 2024. **21**(7): p. 477-492.

153. Darwish, S.F., et al., *Antifibrotic mechanism of deferoxamine in concanavalin A induced-liver fibrosis: Impact on interferon therapy*. Biochem Pharmacol, 2015. **98**(1): p. 231-42.

154. Mohammed, A., et al., *Deferoxamine alleviates liver fibrosis induced by CCl4 in rats*. Clin Exp Pharmacol Physiol, 2016. **43**(8): p. 760-8.

155. Zhang, A.S., et al., *Localization of iron metabolism-related mRNAs in rat liver indicate that HFE is expressed predominantly in hepatocytes*. Blood, 2004. **103**(4): p. 1509-14.

156. Brenner, C., et al., *Decoding cell death signals in liver inflammation*. J Hepatol, 2013. **59**(3): p. 583-94.

157. Herranz, N., et al., *mTOR regulates MAPKAPK2 translation to control the senescence-associated secretory phenotype*. Nat Cell Biol, 2015. **17**(9): p. 1205-17.

158. Laberge, R.M., et al., *MTOR regulates the pro-tumorigenic senescence-associated secretory phenotype by promoting IL1A translation*. Nat Cell Biol, 2015. **17**(8): p. 1049-61.

159. Zhang, M., et al., *Hepatic stellate cell senescence in liver fibrosis: Characteristics, mechanisms and perspectives*. Mech Ageing Dev, 2021. **199**: p. 111572.

160. Maeso-Diaz, R., et al., *Targeting senescent hepatocytes using the thrombomodulin-PAR1 inhibitor vorapaxar ameliorates NAFLD progression*. Hepatology, 2023. **78**(4): p. 1209-1222.

161. Ravichandra, A., S. Bhattacharjee, and S. Affo, *Cancer-associated fibroblasts in intrahepatic cholangiocarcinoma progression and therapeutic resistance*. Adv Cancer Res, 2022. **156**: p. 201-226.

162. Shanmugasundaram, K., et al., *NOX4 functions as a mitochondrial energetic sensor coupling cancer metabolic reprogramming to drug resistance*. Nat Commun, 2017. **8**(1): p. 997.

163. Hanley, C.J., et al., *Targeting the Myofibroblastic Cancer-Associated Fibroblast Phenotype Through Inhibition of NOX4*. J Natl Cancer Inst, 2018. **110**(1): p. 109-20.

164. Ford, K., et al., *NOX4 Inhibition Potentiates Immunotherapy by Overcoming Cancer-Associated Fibroblast-Mediated CD8 T-cell Exclusion from Tumors*. Cancer Res, 2020. **80**(9): p. 1846-1860.

165. Crestani, B., V. Besnard, and J. Boczkowski, *Signalling pathways from NADPH oxidase-4 to idiopathic pulmonary fibrosis*. Int J Biochem Cell Biol, 2011. **43**(8): p. 1086-9.

166. Barnes, J.L. and Y. Gorin, *Myofibroblast differentiation during fibrosis: role of NAD(P)H oxidases*. Kidney Int, 2011. **79**(9): p. 944-56.

167. Siedlar, A.M., et al., *NADPH oxidase 4 is dispensable for skin myofibroblast differentiation and wound healing*. Redox Biol, 2023. **60**: p. 102609.

168. Sampson, N., et al., *Inhibition of Nox4-dependent ROS signaling attenuates prostate fibroblast activation and abrogates stromal-mediated protumorigenic interactions*. Int J Cancer, 2018. **143**(2): p. 383-395.

169. Mir, S., et al., *Upregulation of Nox4 induces a pro-survival Nrf2 response in cancer-associated fibroblasts that promotes tumorigenesis and metastasis, in part via Birc5 induction*. Breast Cancer Res, 2022. **24**(1): p. 48.

170. Huang, H., et al., *Mesothelial cell-derived antigen-presenting cancer-associated fibroblasts induce expansion of regulatory T cells in pancreatic cancer*. Cancer Cell, 2022. **40**(6): p. 656-673 e7.

171. Sun, L., et al., *PD-L1 promotes myofibroblastic activation of hepatic stellate cells by distinct mechanisms selective for TGF-beta receptor I versus II*. Cell Rep, 2022. **38**(6): p. 110349.

172. Carapeto, F., et al., *The immunogenomic landscape of resected intrahepatic cholangiocarcinoma*. Hepatology, 2022. **75**(2): p. 297-308.

173. Xia, T., et al., *Immune cell atlas of cholangiocarcinomas reveals distinct tumor microenvironments and associated prognoses*. J Hematol Oncol, 2022. **15**(1): p. 37.